



Università degli studi ROMA TRE

Dottorato di ricerca in Scienze dell'Ingegneria Civile
XX Ciclo

Tesi di Dottorato

Implementation and experimental verification of
models for nonlinear analysis of masonry infilled
r.c. frames

Dottorando: Alessandro Vittorio Bergami

Docente guida: Prof. Camillo Nuti

Coordinatore del dottorato: Prof. Leopoldo Franco

Roma, Novembre 2007

Collana delle tesi di Dottorato di Ricerca
In Scienze dell'Ingegneria Civile
Università degli Studi Roma Tre
Tesi n° 17

Sommario

L'influenza della tamponatura sulla risposta strutturale di telai tamponati sottoposti ad azione sismica è stata largamente indagata attraverso numerose campagne sperimentali e lo studio di molteplici modelli analitici.

In questo lavoro, con riferimento a strutture e materiali largamente diffusi in Italia, sono discussi i risultati di prove sperimentali condotte, presso il *Laboratorio di sperimentazione su materiali e strutture* dell'Università degli Studi Roma Tre, su laterizi, malta, muri singoli ed accoppiati e su portali in cemento armato nudi e tamponati. Parallelamente all'attività sperimentale sono stati implementati modelli numerici a fibre, rappresentativi delle strutture studiate, avvalendosi di modelli a singola e tripla biella per i pannelli di tamponatura. L'accuratezza dei risultati numerici è stata valutata attraverso il confronto con i risultati sperimentali ottenuti dalle prove cicliche condotte sui portali in c.a.

L'analisi numerica è stata estesa a telai più complessi aventi differenti distribuzioni di tamponatura.

Abstract

The effects of infill panels on the response of r.c. frames subjected to seismic action are widely recognised and numerous experimental investigations as well as several analytical models have been developed on this subject. In this work, referring to specific materials and structures commonly used in Italy, experimental tests performed at the *Laboratory of experiments on materials and structures* of the University Roma Tre on bricks, single and double masonry infills, walls and finally on bare and infilled r.c. portals, are described and discussed. Together with the experimental activity, the implementation of non linear fiber models representative of the considered structures by means of single and triple strut nonlinear cyclic models for masonry panels is described. The accuracy of the models has been assessed through comparison with experimental results obtained from cyclic tests of frames. The numerical model has been extended to multy-storey r.c. frames with different infill configurations.

Contents

FIGURES INDEX.....	5
TABLES INDEX.....	14
1. INTRODUCTION.....	17
1.1 AIMS OF THE STUDY	18
1.2 THESIS LAYOUT.....	19
2. EXPERIMENTAL CHARACTERIZATION OF INFILLS.....	20
2.1 INTRODUCTION.....	20
2.2 MATERIALS SELECTION AND SAMPLES PREPARATION	20
2.3 EXPERIMENTAL TESTS ON MORTAR	24
2.3.1 <i>Experimental tests on type 1 mortar</i>	24
2.3.2 <i>Experimental tests on type 2 mortar</i>	28
2.4 EXPERIMENTAL TESTS ON BRICKS	31
2.4.1 <i>Compression tests on hollow bricks</i>	31
2.4.2 <i>Compression tests on half-full bricks</i>	34
2.5 EXPERIMENTAL TESTS ON WALLS.....	38
2.6 EXPERIMENTAL TEST RESULTS ON HOLLOW BRICK AND TYPE 1 MORTAR WALLS ..	51
2.7 EXPERIMENTAL TEST RESULTS ON HALF-FULL BRICKS AND TYPE 1 MORTAR WALLS	60
2.8 EXPERIMENTAL TESTS RESULTS ON WALLS OF HALF-FULL BRICKS AND TYPE 2 MORTAR	69
2.9 INFLUENCE OF MORTAR ON EXPERIMENTAL RESULTS.....	78
2.10 CORRELATION BETWEEN MATERIALS AND WALLS' STRENGTH.....	79
2.11 EXPERIMENTAL TESTS RESULTS OF DOUBLE PANEL WALLS	88
3. EXPERIMENTAL TESTS ON PORTAL'S MATERIALS.....	94
3.1 INTRODUCTION.....	94
3.2 EXPERIMENTAL TESTS ON REINFORCING BARS	94
3.3 EXPERIMENTAL TESTS ON CONCRETE.....	98
3.4.1 <i>Non-destructive tests</i>	100
3.4.2 <i>Destructive tests</i>	102
4. EXPERIMENTAL MODELS.....	103
4.1 INTRODUCTION.....	103
4.2 DESCRIPTION OF THE SAMPLES.....	103
4.3 DESCRIPTION OF OPENSEES	109
4.4 DESCRIPTION OF THE NUMERICAL MODEL	110
4.5 DESCRIPTION OF THE 1:1 SCALED FRAME	116

5.	GLOBAL MODELS OF INFILLED R.C. FRAMES	118
5.1	INTRODUCTION.....	118
5.2	STRUCTURAL RESPONSE OF INFILLED FRAMES	118
5.3	SINGLE STRUT MODEL	120
5.4	INFILL CONSTITUTIVE MATERIAL MODEL	122
5.4.1	<i>Determination of the single strut dimension</i>	<i>124</i>
5.5	TRIPLE STRUT MODEL.....	126
5.5.1	<i>Determination of the triple strut geometry</i>	<i>127</i>
6.	ANALYSES RESULTS FOR THE PORTAL MODEL	131
6.1	INTRODUCTION.....	131
6.2	NUMERICAL MODEL OF THE PORTAL WITH SINGLE STRUT	131
6.3	ANALYSES RESULTS FOR THE PORTAL WITH THE TRIPLE STRUT MODEL	141
7.	EXPERIMENTAL TESTS ON PORTALS	148
7.1	INTRODUCTION.....	148
7.2	EXPERIMENTAL EQUIPMENT	148
7.3	EXPERIMENTAL TESTS ON THE BARE PORTAL F_{N1}	158
7.4	EXPERIMENTAL TESTS ON THE INFILLED PORTAL F_{T1} AND F_{T2}	167
7.4.1	<i>Experimental test on the portal F_{T1}</i>	<i>167</i>
7.4.2	<i>Experimental test on the portal F_{T2}</i>	<i>172</i>
7.4.3	<i>Behaviour mode observed</i>	<i>176</i>
7.5	EXPERIMENTAL DETERMINATION OF THE EQUIVALENT STRUT	177
7.6	COMPARISON OF THE EXPERIMENTAL AND NUMERICAL RESULTS.....	183
8.	ANALYSES RESULTS FOR THE 1:1 SCALED FRAMES.....	187
8.1	INTRODUCTION.....	187
8.2	NUMERICAL MODELS AND ANALYSES RESULTS	187
9.	CONCLUSIONS.....	203
9.1	FUTURE DEVELOPMENTS	205
	BIBLIOGRAPHY	206

Figures index

Figure 2.1: hollow bricks 8x16x33cm ³	27
Figure 2. 2: half-full bricks 12x12x25 cm ³	21
Figure 2.3: types of infill walls: a) walls with double panel with air space b) plain wall	21
Figure 2.4: MTS press.....	29
Figure 2.5: Metrocom press.....	23
Figure 2.6: characteristics of the system for compression tests on bricks.....	23
Figure 2.7: bending test on mortar [mm]	24
Figure 2.8: bending tests on mortar samples.....	25
Figure 2.9: type 1 mortar bending tests, load-deformation	26
Figure 2.10: Compression tests on mortar cylinders.....	27
Figure 2.11: type 1 mortar stress–strain curve	28
Figure 2.12: type 2 mortar bending tests, load-deformation	30
Figure 2.13: type 2 mortar stress–strain curve	30
Figure 2.14: hollow bricks compression tests, compression orthogonal to holes (left); compression parallel to holes (right).....	31
Figure 2.15: failure of a hollow bricks sample compression orthogonal to holes (left); compression parallel to holes (right).....	31
Figure 2.16: hollow bricks stress-strain curve, compression tests orthogonal to holes...	32
Figure 2.17: hollow bricks load-deformation curve, compression tests orthogonal to holes.....	32
Figure 2.18: hollow bricks stress-strain curve, compression tests parallel to holes.....	33
Figure 2.19: hollow bricks load-deformation curve, compression tests parallel to holes	33
Figure 2.20: half-full bricks compression tests, compression parallel to holes (left); compression orthogonal to holes (right)	35
Figure 2.21: failure of a sample of half-full bricks, compression parallel to holes (right) and orthogonal holes (left)	35
Figure 2.22: half-full bricks stress-strain curve, compression tests parallel to holes	36
Figure 2.23: half-full bricks load-displacement curve, compression tests parallel to holes.....	36
Figure 2.24: half-full bricks stress-strain curve, compression tests orthogonal to holes.	37

Figure 2.25: half-full bricks load-displacement curve, compression tests parallel to holes.....	37
Figure 2.26: walls specimens, walls of half-full bricks (left), walls of hollow bricks (right)	39
Figure 2.27: double panel walls, specimens ready to be tested (left), side view of double panel wall (right).....	39
Figure 2.28: steel profile used to transfer the compression load on walls.....	40
Figure 2.29: steel saddle used to settle diagonally the walls.....	40
Figure 2.30: vertical compression test, layout of test systems	41
Figure 2.31: diagonal compression test, layout of test system	41
Figure 2.32: equipment set up for vertical compression tests: the steel profiles fitted on the Metrocom 3000 kN press (left), a wall ready to be crashed inside the press (right) .	42
Figure 2.33: diagonal compression tests set up, steel supports for diagonal compression tests (left), wall ready to be crashed inside the press (right)	42
Figure 2.34: suspension system of the upper steel profile	42
Figure 2.35: transducer adopted to measuring deformations (left), the external transducer installed (right)	43
Figure 2.36: hollow brick panels layout of sensors on the wall compressed parallel to holes [mm]	44
Figure 2.37: hollow brick panels layout of sensors on the wall compressed orthogonally to holes [mm].....	44
Figure 2.38: hollow brick panels layout of sensors on the wall compressed diagonally [mm]	44
Figure 2.39: half-full brick panels layout of sensors on the wall compressed parallel to holes [mm]	45
Figure 2.40: half-full brick panels layout of sensors on the wall compressed orthogonally to holes [mm].....	45
Figure 2.41: half-full brick panels layout of sensors on the wall compressed diagonally [mm]	45
Figure 2.42: double panel walls layout of sensors on the wall compressed parallel to holes [mm]	46
Figure 2.43: double panel walls layout of sensors on the wall compressed orthogonally to holes [mm]	46
Figure 2.44: double panel walls layout of sensors on the wall compressed diagonally [mm]	46
Figure 2.45: equipment for compression test parallel to holes on hollow brick walls (front and back view of the panel)	47

Figure 2.46: equipment for compression test orthogonal to holes on hollow brick walls (front and back view of the panel)	47
Figure 2.47: equipment for diagonal on hollow brick walls (front and back view of the panel)	47
Figure 2.48: equipment for compression test parallel to holes on half-full brick walls (front and back view of the panel)	48
Figure 2.49: equipment for compression test orthogonal to holes on half-full brick walls (front and back view of the panel)	48
Figure 2.50: equipment for diagonal compression test half-full brick walls (front and back view of the panel)	48
Figure 2.51: equipment for vertical compression on double panel walls (front and back view of the panel).....	49
Figure 2.52: equipment for horizontal compression on double panel walls (front and back view of the panel)	49
Figure 2.53 equipment for diagonal compression on double panel walls (front and back view of the panel).....	49
Figure 2.54: compression test parallel to holes, initial phase and collapse	52
Figure 2.55: compression test orthogonal to hole, initial phase and collapse	52
Figure 2.56: diagonal compression test, front and side collapse view	52
Figure 2.57: compression tests parallel to holes, load-displacement curves of walls of hollow brick and type 1 mortar	53
Figure 2.58: compression tests parallel to holes, stress-strain curves of walls of hollow brick and type 1 mortar	53
Figure 2.59: compression tests orthogonal to holes, load-displacement curves of walls of hollow brick and type 1 mortar.....	54
Figure 2.60: compression tests orthogonal to holes, stress-strain curves of walls of hollow brick and type 1 mortar	54
Figure 2.61: diagonal compression tests, load-displacement curves of walls of hollow brick and type 1 mortar	55
Figure 2.62: diagonal compression tests, stress-strain curves of walls of hollow brick and type 1 mortar.....	55
Figure 2.63: comparison between average elastic modulus determined from internal or external transducers [MPa]	58
Figure 2.64: comparison between maximum strains determined from internal or external transducers [-]	58
Figure 2.65: compression test parallel to holes, initial phase and collapse	61

Figure 2.66: compression test orthogonal to holes, initial phase and collapse.....	61
Figure 2.67: diagonal compression test, initial phase and collapse.....	61
Figure 2.68: compression tests parallel to holes, load-displacement curves of walls of half-full bricks and type 1 mortar	62
Figure 2.69:: compression tests parallel to holes, stress-strain curves of walls of half-full bricks and type 1 mortar	62
Figure 2.70: compression tests orthogonal to holes, load-displacement curves of walls of half-full bricks and type 1 mortar	63
Figure 2.72: diagonal compression tests, load-displacement curves of walls of half-full bricks and type 1 mortar	64
Figure 2.74: comparison between average elastic modulus determined from internal or external transducers [MPa]	66
Figure 2.75: comparison between maximum strains determined from internal or external transducers [-]	67
Figure 2.76: compression tests parallel to holes, load-displacement curves of walls of half-full bricks and type 2 mortar	69
Figure 2.78: compression tests othogonal to holes, load-displacement curves of walls of half-full bricks and type 2 mortar	70
Figure 2.79: compression tests orthogonal to holes, stress-strain curves of walls of half-full bricks and type 2.....	71
Figure 2.80: diagonal compression tests, load-displacement curves of walls of half-full bricks and type 2	71
Figure 2.80: diagonal compression tests, stress-strain curves of walls of half-full bricks and type 2 mortar	72
Figure 2.82: stress–strain curves (internal transducer) from compression tests parallel to holes.....	74
Figure 2.83: stress–strain curves (internal transducer) from compression tests orthogonal to holes.....	74
Figure 2.83 stress–strain curves (internal transducer) from diagonal compression tests	75
Figure 2.84: comparison between maximum loads of walls with different mortar	78
Figure 2.85: comparison between theoretical and experimental strength walls of hollow bricks and type 1 mortar	82
Figure 2.86: comparison between theoretical and experimental strength of walls of half-full bricks and type 1 mortar	82
Figure 2.87: comparison between theoretical and experimental strength of walls of half-full bricks and type 2 mortar	83

Figure 2.88: comparison between experimental strength of walls as a percentage of bricks strength.....	84
Figure 2.89: comparison between experimental strength of walls as a percentage of type 1 mortar strength	85
Figure 2.90: comparison between experimental strength of half-full bricks walls as a percentage of bricks strength	85
Figure 2.91: comparison between experimental strength of walls as a percentage of mortar's strength	86
Figure 2.92: comparison between experimental and theoretical orthogonal to holes strength, of walls built using half-full bricks with type 1 and type 2 mortar	86
Figure 2.93: comparison between experimental and theoretical parallel to holes strength of walls built using half-full bricks with type 1 and type 2 mortar	87
Figure 2.94: compression test parallel to holes, initial phase and collapse	89
Figure 2.95: compression test orthogonal to the holes: initial phase and collapse.....	89
Figure 2.96: diagonal compression test, front and side view of collapse.....	89
Figure 2.97: load–displacement curves from parallel to holes compression tests of double panel walls.....	90
Figure 2.98: stress–strain curves from parallel to holes compression tests of double panel walls	90
Figure 2.99: load–displacement curves from orthogonal to holes compression tests of double panel walls.....	91
Figure 2.101: load–displacement curves from diagonal compression tests of double panel walls.....	92
Figure 2.102: stress –strain curves from diagonal compression tests of double panel walls	92
Figure 3.1: sclerometric test (left) and ultrasonic test (right) on a column of the portal.	99
Figure 4.1: carpentry and rebar of the r.c. portal.....	105
Figure 4.2: rebar of the r.c. portal	106
Figure 4.3: plans of the building that the frame examined belongs to (scale ratio 1:1, length in [cm], the frame is highlighted)	108
Figure 4.4: the frame analyzed (scale ratio 1:1), the position of the portal (realized in reduced scale ratio) is highlighted [cm]	108
Figure 4.5: characteristics of the portal frame.....	109
Figure 4.6: fibre-based model	110
Figure 4.7: Kent & Park concrete model	111

Figure 4.8: analytical response for cycling load of concrete.....	113
Figure 4.9: OpenSees CONCRETE02 response for cycling load (unconfined concrete)	113
Figure 4.10: OpenSees CONCRETE02 response to cycling load (column confined concrete).....	114
Figure 4.11: OpenSees CONCRETE02 response to cycling load (beam confined concrete).....	114
Figure 4.12: OpenSees model of the portal.....	115
Figure 4.13: curvature–moment relationship of portal’s sections	115
Figure 4.13: resistant sections of beams 50x20 cm (top) and columns 40x20 cm (bottom) of the frame (scale ratio 1:1) [cm].....	116
Figure 4.14: curvature–moment relationship of frame’s beams.....	117
Figure 4.15: curvature–moment relationship of frame’s columns	117
Figure 5.1: shelf consisting of frame and infill	119
Figure 5.2: stiffness of the bare frame and the diagonal strut in parallel	120
Figure 5.3: strut model proposed by (Camberscuc 1996)	122
Figure 5.4: triple strut models with different distributions of contact stress between the infill and frame.....	128
Figure 5.5: loads and stress components of the model.....	128
Figure 6.1: geometry of the infilled portal (width: r.c. elements=200 mm; wall=120 mm) [mm]	132
Figure 6.2: position of the equivalent strut	132
Figure 6.3: the Hysteretic Material	134
Figure 6.4: axial load–axial deformation of the single strut initially defined	134
Figure 6.5: axial load-deformation of the calibrated single strut model	135
Figure 6.6: comparison between the model initially defined (initial) and the experimental one (calibrated).....	135
Figure 6.8: bare and infilled portal: base shear – top displacement	137
Figure 6.9: localization of plastic hinges on the capacity curve of the bare (top) and infilled portal with single strut model (bottom)	138
Figure 6.10: bare (left) and infilled (right) portal: localisation of plastic hinges	139
Figure 6.13: geometry of the triple strut	142
Figure 6.14: implemented triple strut model [mm]	142
Figure 6.15: constitutive model of the triple strut	144

Figure 6.16: base shear–top displacement of the portal with triple strut.....	144
Figure 6.17: comparison between capacity curve of the infilled portal models.....	145
Figure 6.18: localization of plastic hinges on the capacity curve of the infilled portal with triple strut model.....	145
Figure 6.19: infilled portal with triple strut model, localisation of plastic hinges.....	146
Figure 6.20: shear acting on column 1	147
Figure 6.21: shear acting on column 2	147
Figure 7.1: layout of the test system developed	149
Figure 7.2: the test system set-up on the portal F_{n1}	149
Figure 7.3: details of the jack M_h installed on the contrast wall (top) and on the portal (bottom)	150
Figure 7.4: structure designed to apply the gravity load on columns.....	151
Figure 7.5: basement fixing system	151
Figure 7.6: instrumentation of the bare portal.....	153
Figure 7.7: instrumentation of the infilled portal, side 1 and side 2.....	154
Figure 7.8: set-up of the experimental test on the bare portal.....	155
Figure 7.9: the bare portal ready to be tested	155
Figure 7.10: portal instrumentation's details.....	156
Figure 7.11: instrumentation of the infilled portal, side 1	156
Figure 7.12: instrumentation of the infilled portal, side 2.....	157
Figure 7.13: loading cell inserted under the hydraulic jack	157
Figure 7.14: portal F_{n1} , damage to the base of the columns (top displacement of 30 mm)	159
Figure 7.15: portal F_{n1} , damage to the top of the columns (collapse)	160
Figure 7.16: portal F_{n1} , cracks map.....	160
Figure 7.17: portal F_{n1} , excursion of the jack M_h – load applied by the jack M_h	161
Figure 7.18: portal F_{n1} , top displacement–horizontal load	162
Figure 7.19: portal F_{n1} , envelope of the test performed	162
Figure 7.20: column lower section, curvature-moment	164
Figure 7.21: column lower section, curvature-horizontal load.....	165
Figure 7.22: column upper section, curvature-horizontal load.....	166

Figure 7.23: column sections, curvature-horizontal load	167
Figure 7.24: portal F_{t1} , superficial cracks along columns height	169
Figure 7.25: portal F_{t1} , infill damages during the experimental test (close to maximum load)	169
Figure 7.25: portal F_{t1} , infill damages during the experimental test (in correspondence with the maximum load)	170
Figure 7.27: portal F_{t1} , infill damages during the experimental test (after having achieved maximum load).....	170
Figure 7.28: portal frame F_{t1} , detail of the structure following collapse	171
Figure 7.29: portal F_{t1} , top displacement–horizontal load.....	171
Figure 7.30: portal frame F_{t1} , infill damages during the experimental test (after having achieved maximum load).....	173
Figure 7.31: portal F_{t2} , top displacement–horizontal load.....	173
Figure 7.31: column lower section, curvature-horizontal load.....	174
Figure 7.32: column upper section, curvature-horizontal load.....	174
Figure 7.33: column upper and lower sections, curvature-horizontal load	175
Figure 7.34: diagonal deformation, deformation-horizontal load	175
(transducer 41)	175
Figure 7.34: -drift between the panel and the beam-load.....	176
(transducer 33)	176
Figure 7.34: characteristics of the equivalent strut determined as the difference between the capacity curves of the portal F_{t1} and F_{t2}	178
Figure 7.35: experimental results Vs calibrated model (implemented in the numerical model) of the diagonal strut, axial load –deformation	180
Figure 7.36: experimental stress strain relationship of the strut.....	180
Figure 7.37: theoretical Vs calibrated models of the diagonal strut, axial load- deformation.....	181
Figure 7.38: experimental and numerical capacity curves of the bare portal.....	183
Figure 7.39: experimental and numerical cyclic analysis of the bare portal	184
Figure 7.40: experimental and numerical cyclic analysis of the infilled portal.....	184
Figure 7.41: experimental and numerical capacity curves of the infilled portal	185
Figure 8.1: geometry of the r.c. frame, scale ratio 1:1 [cm].....	188
Figure 8.2: details of one single infilled portal of the frame, scale ratio 1:1 [mm].....	189

Figure 8.3: frame Fb (left) and Fi,1 (right)	190
Figure 8.4: frame Fi,2 (left) and Fi,3 (right)	190
Figure 8.5: distribution of the horizontal loads adopted (proportional to the first modal form)	191
Figure 8.6: capacity curves of the frames analysed.....	191
Figure 8.7: horizontal displacements of each level (up) interstorey drift of the bare frame (down).....	194
Figure 8.8: horizontal displacements of each level (up) interstorey drift of the frame type 1(down).....	195
Figure 8.9: horizontal displacements of each level (up) interstorey drift of the frame type 2 (down).....	196
Figure 8.10: horizontal displacements of each level (up) interstorey drift of the frame type 3 (down).....	197
Figure 8.11: capacity curve and plastic hinges of the bare frame	198
Figure 8.12: capacity curve and plastic hinges of the frame type 2	198
Figure 8.13: plastic hinges on the bare (left) and type 1(right) frame.....	199
Figure 8.15: triple strut model (frame scale ratio 1:1)	201
Figure 8.16: geometry of the triple strut model (frame scale ratio 1:1)	201
Figure 8.17: comparison between the capacity curves determined with the triple strut and the single strut models for the frame type 1	202

Tables index

Table 2.1: type 1 mortar traction strength	26
Table 2.2: type 1 mortar compression tests results	28
Table 2.3: type 2 mortar compression tests results	29
Table 2.4: type 2 mortar traction strength	31
Table 2.5: compression tests on hollow bricks: summary of results ($f_{c,p}$ =compression strength parallel to holes; $f_{c,o}$ =compression strength orthogonal to holes)	34
Table 2.6: compression tests on half-full bricks: summary of results ($f_{c,p}$ =compression strength parallel to holes; $f_{c,o}$ =compression strength orthogonal to holes)	38
Table 2.7: results of compression tests parallel to holes on hollow bricks walls	56
Table 2.8: results of compression tests orthogonal to holes on hollow brick walls	57
Table 2.9: results of diagonal compression tests on hollow brick walls	57
Table 2.10: elastic modulus determined from internal transducers	57
Table 2.11: characterization of infill wall of hollow bricks type 1 mortar	59
Table 2.13: results of compression tests parallel to holes on half-full brick walls	65
Table 2.14: results of compression tests orthogonal to holes on half-full brick walls	65
Table 2.15: results of diagonal compression tests on half-full brick walls	65
Table 2.16: elastic modulus determined from internal transducers	66
Table 2.17: characterisation of infill wall of half-full and type 1 mortar	68
Table 2.18: results from compression parallel to holes on walls of half-full bricks and type 2 mortar	72
Table 2.19: results from compression orthogonal to holes on walls of half-full bricks and type 2 mortar	73
Table 2.20: results from diagonal compression on walls of half-full bricks and type 2 mortar	73
Table 2.21: elastic modulus from internal transducers	75
Table 2.22: strains from internal transducers	76
Table 2.23: summary of data for diagonal compression	76
Table 2.24: summary of data from external and internal transducers	76
Table 2.25: characterisation of infill wall of half-full bricks and type 2 mortar	77
Table 2.26: characteristics of type 1 and type 2 mortar	78
Table 2.27: formulation adopted to determine walls' strength	80

Table 2.28: average strength of walls of hollow bricks and type 1 mortar (the characteristic values are expressed in brackets).....	80
Table 2.29: average strength of walls of half-full bricks and type 1 mortar (the characteristic values are expressed in brackets).....	81
Table 2.30: average strength of walls of walls of half-full bricks made from type 1 mortar (the characteristic values are expressed in brackets)	81
Table 2.31: results of compression tests on double panel walls.....	93
Table 3.1: weight, length and equivalent diameter of samples	95
Table 3.2: mechanical parameters from traction tests (part A)	96
Table 3.3: mechanical parameters from traction tests (part B)	97
Table 3.4: mechanical parameter from traction tests (part C).....	98
Table 3.5: sclerometric test on portal 1	100
Table 3.6: sclerometric test on portal 2	101
Table 3.7: ultrasonic test on portal 1	101
Table 3.8: ultrasonic test on portal 2	102
Table 3.9: concrete compressive strength from Sonreb method	102
Table 3.10: destructive tests results	102
Table 4.1: scale ratio factors	104
Table 4.1: analysis of loads of the frame (1:1 scale ratio)	107
Table 4.3: nodal loads ad masses of the frame (1:1 scale ratio).....	107
Table 5.1: summary of mechanical infill's parameter adopted	125
Table 5.2: symbols adopted	126
Table 6.1: parameters of the single strut model	132
Table 6.2: bare and infilled portal: maximum horizontal load and elastic stiffness.....	137
Table 6.3: geometric parameters of the triple strut model	141
Table 6.4: bare and infilled portal: maximum horizontal load and elastic stiffness.....	146
Table 7.1: summary of data from test on the infilled portal Ft2.....	178
Table 7.2: experitmental dimension of the strut.....	179
Table 7.3: load-deformation curve of the theoretical strut model	179
Table 7.4: load-deformation curve of the experimental strut model	179
Table 7.5: stress-strain curve of the calibrated strut model.....	181

Table 7.6: summary of parameters of the calibrated infill model	181
Table 8.1: geometry and mechanical parameters of the infill panel.....	188
(1:1 scale ratio)	188
Table 8.2: stress-strain curve of the infill, experimentally determined	189
Table 8.3: parameters of the constitutive model of the strut determined for the frame (1:1 scale ratio)	189
Table 8.4: modal analysis results, parameter of the horizontal load distribution	192
Table 8.5: summary of results of the pushover analyses.....	192
Table 8.6: geometry of the triple strut model.....	200

1. Introduction

Framed structures were traditionally designed without taking into account the presence of infills realized with the objective of closing, or dividing the various building's spaces. This commonly accepted design process, also due to the weak calculation instruments available, led to a simplified structural analyses.

In reality, especially under horizontal loads the infills influence may result in important changes in terms of static as well as dynamic structural response. As is well known, infill provides to concrete structure a higher stiffness and a different stiffness distribution both in plan and in elevation.

Furthermore, as well demonstrated in by experimental studies and experiences from past seismic events, the infill influence can also be felt locally on structural elements; an important example is the collapse of slender columns under shear loading effects as a consequence of frame-infill interaction. Furthermore, the positive effects that infill has on structural behaviour are also very important as they can make the structure stiffer and more resistant to horizontal loads.

Experts are currently divided between two opposite points of view for the development of new constructions. According to the first point of view, the negative effect of infill is much more important due to the high uncertainties that exist as a consequence of the poor level of homogeneity of infill's materials; therefore infills should be completely disconnected from the frame so as not to alter the behaviour expected from the design process. The second position underlines that for reasons related to economy and execution simplicity it is best to benefit from all of the structural and non structural elements; therefore infills should collaborate and, in the meantime, the potentially negative effects would be minimized through a careful study of structural details.

Existing technical codes are focused on the first point of view even though they provide modelling procedures that include nonstructural elements.

By analysing the state of the art of this topic, it is surprising to realize how a matter that has been investigated for more than 40 years has not lead to satisfactory models. This could be attributed to the very high number of parameters that rule the question: the first being the strong variability of materials qualities and workmanship influence.

Following an in-depth analysis of scientific literature and design codes it stands to reason that a unique method allowing for determination of infill models, with the aim of being able to study structural response of buildings in their real configuration without neglecting non structural component, does not exist.

The aim of the scientific activity described in this thesis is to adopt some kinds of infill widely diffused in Italy as experimental samples. At the same time as the experimental activities carried out, reference has been made to scientific literature in order to assess the efficiency of formulas for the analytical determination of mechanical characteristics of the infill and elementary models capable of simulating global behaviour of masonry infilled frames.

With the aim of pursuing a complete course, the experimental activities carried out on elementary materials and therefore on structural models are presented and discussed. Referring to results acquired and supported by the software for structural analysis *OpenSees*, experimentally validated numerical models have been generated.

1.1 Aims of the study

Study's aims are to achieve definition of a simplified model suitable for a simple and efficient non linear static analysis of infilled framed buildings, as well as to assess the level of safety with regards to collapse. Another requirement of the model is, obviously, the level of reliability of forecasts: for this purpose the numerical parameters have been calibrated on the basis of experimental results achieved from walls samples. Afterwards one specific type of infill has been selected to continue the experimental activity on in scale r.c. portals, designed to support vertical loads only, used as samples (bare or infilled) for horizontal loading cyclic tests.

The study begins with detailed experimental activities on two types of mortar and two types of bricks with which wall samples have been built to be subject to experimental compression tests along the three main loading directions.

Passing from elementary materials to wall samples, it has been possible to discuss some formulas proposal from codes and scientific literature for the definition of walls' strength. At the same time, referring to portal's structure (realized from structural materials whose characteristics have been experimentally determined) the first representative numerical

models of bare or infilled frame structures have been created adopting two well known models: the single strut and triple strut model.

As a conclusion of the experimental activities, horizontal loading cyclic tests have been carried out on 3 portals: one bare and two infilled.

On the basis of the experimental results achieved, the numerical models have been discussed and then calibrated until the desired level of reliability has been reached.

At this point the numerical model obtained, that had a proven reliability, has been extended to much more complex plane frames. Therefore these models constitute a conclusion for the discussed activities but also a possible starting point for future studies.

1.2 Thesis layout

In this thesis, at first, experimental activities carried out on materials, walls and portals structural materials are discussed in chapter 2 and chapter 3.

Subsequently, chapters 4 and 5, the selected models (1:2 scale portal and 1:1 scale frames) as well as the adopted numerical models are presented.

The results achieved by the first numerical analyses on the bare portal and on the infilled portal (both the single strut and the triple strut model have been adopted) have been discussed and compared in chapter 6.

In Chapter 7 the experimental tests performed on the bare portal and on the infilled portals have been described; the most interesting results and some selected images have been presented and discussed.

Results achieved from the experimental activity have been used to calibrate the numerical models; then, numerical and experimental result have been compared.

Finally, the calibrated models have been extended to much complex plane frames; some numerical results are presented in Chapter 8. In Chapter 9 a summary of the work has been presented together with some final reflections upon results achieved and future developments.

2. Experimental characterization of infills

2.1 Introduction

As is known, the use of representative models of interaction between infill and r.c. frames require a preliminary knowledge of the mechanical characteristics of the wall and do not always result in a sufficient representation of reality. Following these considerations emerges the necessity to assess, through a comparison offered by direct experimentation, the level of feasibility of currently diffused models. In order to do so, an experimental course has been performed with reference to widely diffused materials, concerning characterization of each single component right through models in scale of walls and frames.

The starting point was therefore a careful selection of the basic materials to be used; with two typologies of bricks (hollow and half-full bricks) and two of mortar (in the following type 1 and type 2 mortar) single panel and double panel walls have been built, commonly used for internal partitions or to infill external facades of civil buildings in Italy. Mechanical characteristics of bricks and mortar chosen have been identified with experimental tests. A total of 48 walls have been built, divided up as follows: 12 built using hollow bricks, 24 using half-full bricks and both types of mortar and 12 double panel walls combining the previous types of brickwork both with type 1 mortar. Once built and following 28 days after maturity of the mortar, it was possible to perform vertical, horizontal and diagonal compression tests on the sample walls.

2.2 Materials selection and samples preparation

A selection between materials commonly used in Italy for the infill of existing r.c. frames.

In particular, the elements that characterise an infill wall are both mortar and bricks used to build it. Mortar is regulated by technical requirements and it is characterised according to its composition and resistance. Indications are also provided by codes for bricks that, in the case of elements without structural functions, have dubious validity as proved in this thesis.

The characterization of a material, be it mortar or bricks, may be performed only through specific experimental tests, that have been

performed on mortar as well as bricks. The mortars selected (further details will be provided in the following paragraphs) can be distinguished as follows: one to be realized on site with a specific mix (type 1) and the other pre-mixed (type 2); the type 2 represents the preferred choice in common construction sites. The bricks used have been chosen as they are widely diffused in Italy, the two types adopted are illustrated in Figure 2.1 and in Figure 2.2.2.

Half-full bricks have vertical holes and their dimensions are $12 \times 12 \times 25 \text{ cm}^3$, hollow bricks (definitions provided by *Italian Code D.M. LL.PP. 20.11.1987*), with horizontal holes have a perforation percentage exceeding 45% and their dimensions are $12 \times 12 \times 25 \text{ cm}^3$. Figure 2.3 illustrates, as an example, a double panel wall and a single panel wall; the wall specimens built will be described in detail in the following paragraphs.



Figure 2.1: hollow bricks $8 \times 16 \times 33 \text{ cm}^3$
 $12 \times 12 \times 25 \text{ cm}^3$



Figure 2. 2: half-full bricks

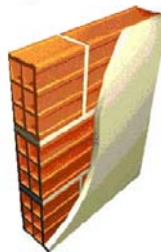


Figure 2.3: types of infill walls: a) walls with double panel with air space
b) plain wall

On the bricks previously described, in order to establish their mechanical characteristics, compression tests have been performed along the main loading directions: vertical and horizontal.

The sample bricks have been prepared through levelling and flattening of surfaces using a layer of high resistance mortar in order to guarantee a correct distribution of stresses on the element, otherwise full of irregularities, without affecting the experimental result.

Twenty-four blocks have been subject to compression test parallel and orthogonally to holes: twelve hollow and twelve half-full.

The compressive strength of the blocks f_b has been determined according to *UNI-EN 772-1* specifications as the ratio between breaking load and the gross area of the section orthogonal to loading direction:

$$f_b = \frac{F_{max}}{b \cdot l} \quad Eq. 2.1$$

with b and l dimensions of the surface orthogonal to loading direction.

The universal press *MTS 810* (maximum load 500 kN), shown in figure.2.4, has been used operating with a displacement speed of 0.05 mm/s and, only for the half-full bricks that have in the direction parallel to the holes a compressive strength exceeding the loading capacity of the press previously described, the *Metrocom* press (maximum load 3000 kN) operating with a loading rate of 0.8 kN/s. Loads and displacements have been automatically acquired.

For a more accurate data acquisition four displacement transducers have been provided between the loading plates (Figure 2.6).



Figure 2.4: MTS press



Figure 2.5: Metrocom press



Figure 2.6: characteristics of the system for compression tests on bricks

2.3 Experimental tests on mortar

2.3.1 Experimental tests on type 1 mortar

In order to characterise the mechanical properties of type 1 mortar two groups of samples have been created:

3 prisms $40 \times 40 \times 160 \text{ mm}^3$

9 cylinders diameter 100 mm , height 200 mm

The loading surfaces of cylinders have been carefully flattened and the samples have been instrumented with four 50 mm strain gauges (two horizontal and two vertical) as illustrated in Figure 2.10.

The composition of type 1 mortar is the following:

- 1 part of *Portland* cement (*CEM II/B-M(L-S-V)*32.5)

- $\frac{1}{4}$ of 32.5 cement

- $\frac{1}{4}$ of 12.5 cement

- 4 parts of sand (granulometry between $1\text{--}4 \text{ mm}$)

The following tests have been performed in accordance with *UNI EN 1015-11 requirements*:

- bending tests on three points (distance between the supports 106 mm) (Figure 2.7, Figure 2.8) on 3 prismatic samples;
- compression tests on 9 cylindrical samples $100 \times 200 \text{ mm}$.

The tests have been performed with the universal machine *MTS 810* operating at a constant displacement speed of 0.05 mm/s .

Bending tests on type 1 mortar prisms

The bending test has been performed according to the layout illustrated below:

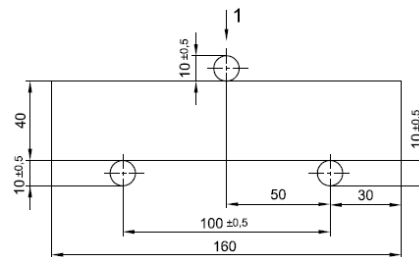


Figure 2.7: bending test on mortar [mm]

Traction strength f , has been obtained with the following formula:

$$f = 1,5 \cdot \frac{F \cdot l}{b \cdot d^2} \quad \text{Eq. 2.2}$$

with:

F	maximum load applied	
l	distance between supports	$(100 \pm 0,5 \text{ mm})$
b	width of the prisms section	(40 mm)
d	height of the prisms section	(40 mm)

The results achieved by the bending tests performed (Figure 2.8) are represented in Figure 2.9 and in Table 2.I.

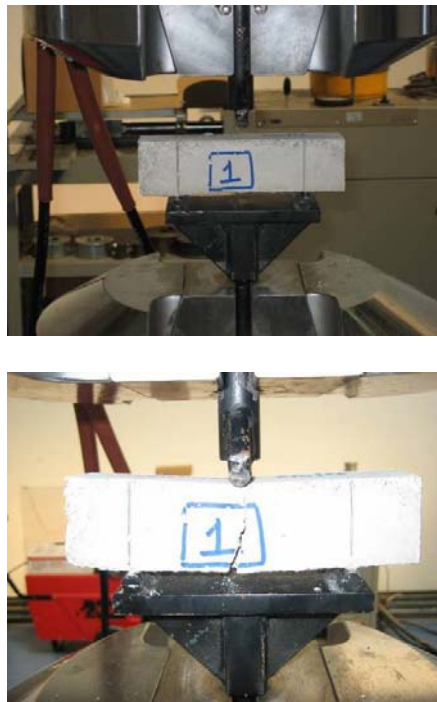


Figure 2.8: bending tests on mortar samples

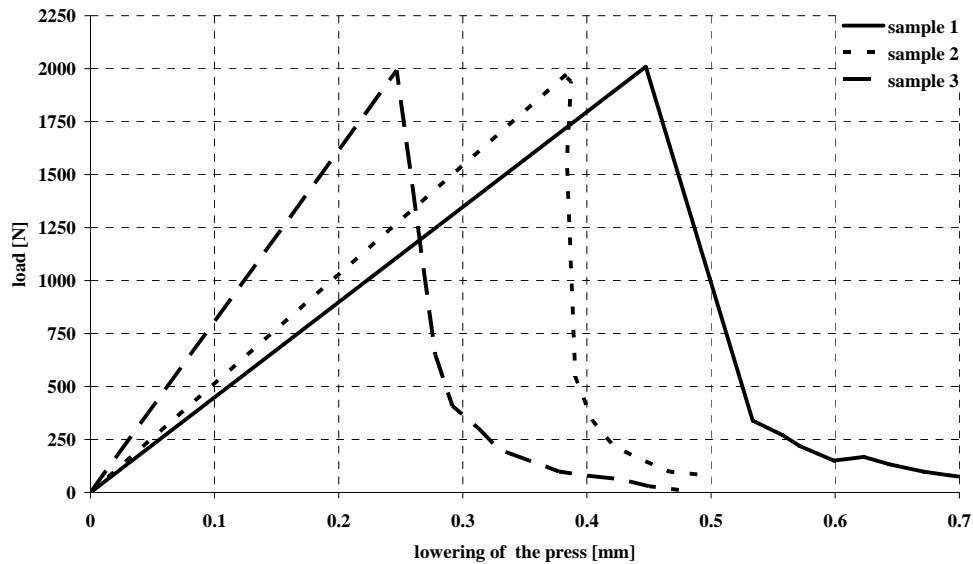


Figure 2.9: type 1 mortar bending tests, load-deformation

<i>Prism</i>	<i>Fmax [N]</i>	<i>f [MPa]</i>
Sample 1	2009	4,70
Sample 2	1975	4,62
Sample 3	1992	4,66
fctm		4,66
fctk=0.7fctm		3,26

Table 2.1: type 1 mortar traction strength

Compression tests on type 1 mortar cylinders

Figure 2.10 illustrates some samples during the compression test. The cylinders have a substantially linear behaviour with a brittle rupture as soon as the maximum stress is reached.



Figure 2.10: Compression tests on mortar cylinders

According to indications provided by *UNI EN 1015-11*, before reaching the maximum load, cycles in an elastic range have been performed in order to guarantee perfect adhesion between the press and the sample. Table 2.II illustrates the compressive strength f and the elastic modulus E determined by each test and the average values. According to test results high compressive strength of mortar has been determined, therefore outside of the *Code* classifications.

The modulus of elasticity, in the absence of specific indications, has been determined with reference to the loading branch limited by 50% and 25% of the maximum load. Figure 2.11 illustrates the final loading *stress-strain* curves. Table 2.II compression test results: maximum load, elastic modulus and the Poisson coefficient are presented.

<i>Cylinder</i>	$f_m[\text{MPa}]$	$E_m[\text{MPa}]$	ν
Sample 1	22.15	-	-
Sample 2	19.48	15157	0.163
Sample 3	24.81	15197	0.181
Sample 4	26.01	18638	0.196
Sample 5	24.09	16900	0.207
Sample 6	26.50	18269	0.207
Sample 7	28.73	17605	0.202
Sample 8	17.96	-	-

Sample 9	21.71	-	-
Average	23.49	16961	0.193
Standard deviation	3.47	1504	0.017
Interval	10.77	3481	0.044
Minimum	17.96	15157	0.163
Maximum	28.73	18638	0.207

Table 2.2: type 1 mortar compression tests results

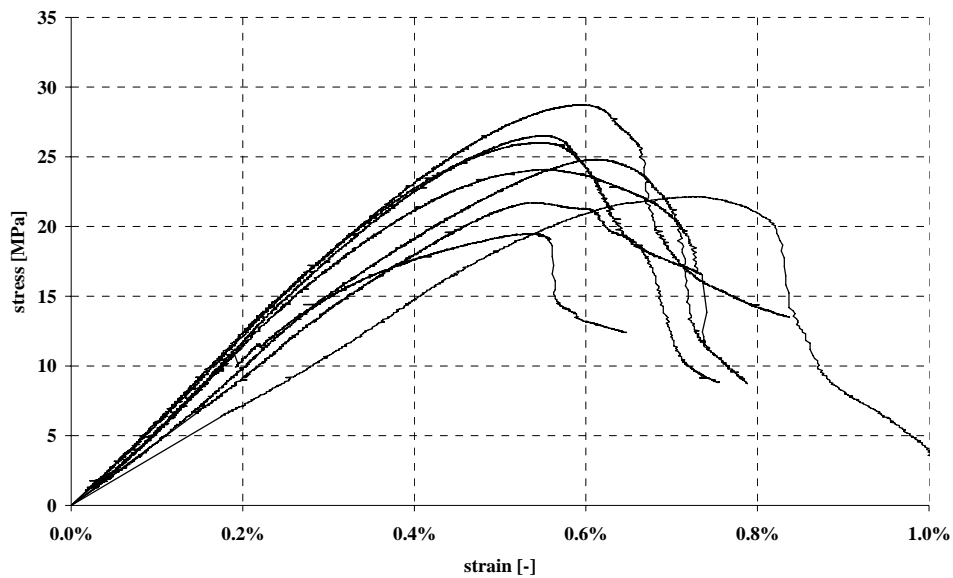


Figure 2.11: type 1 mortar stress–strain curve

2.3.2 Experimental tests on type 2 mortar

The same experimental tests previously described for type 1 mortar have been performed on type 2 mortar: the experimental results are presented as previously done for type 1 mortar. Type 2 mortar, differently from the other one, is a pre-mix consisting of hydrated lime, *Portland* concrete, sands and specific additives in order to reduce the setting time.

This material, chosen as it is widespread in Italy, has the following technical characteristics:

- specific weight in powder 1500 kg/cm³
- granulometry < 3 mm
- minimum thickness 10 mm
- paste water 18%
- elastic modulus after 28 days 8000 Mpa (data from factory)
- class M5 (according *UNI EN998-2* indications)

The results achieved by the experimental tests carried out are briefly illustrated below:

<i>Cylinder</i>	<i>f_m[MPa]</i>	<i>E_m[MPa]</i>	<i>ν</i>
Sample 1	12,83	16049	0,20
Sample 2	12,12	16208	0,21
Sample 3	10,68	16887	0,21
Sample 4	11,22	15405	0,21
Sample 5	12,52	17421	0,23
Sample 6	12,54	16026	0,20
Sample 7	11,05	16113	0,21
Sample 8	10,80	15714	0,24
Average	11,72	16961	0,21
Standard deviation	0,87	1504	0,01
Interval	2,14	3481	0,04
Minimum	12,83	15157	0,20
Maximum	17.96	18638	0,24

Table 2.3: type 2 mortar compression tests results

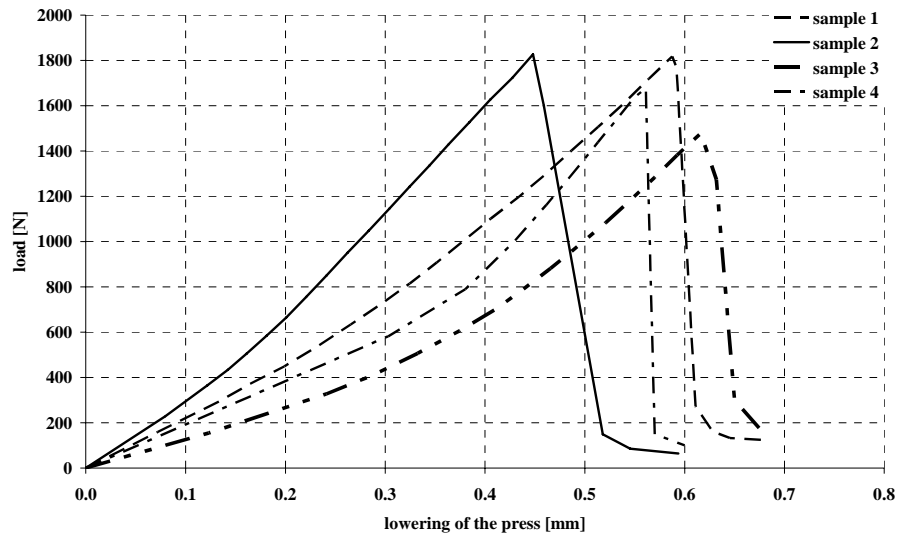


Figure 2.12: type 2 mortar bending tests, load-deformation

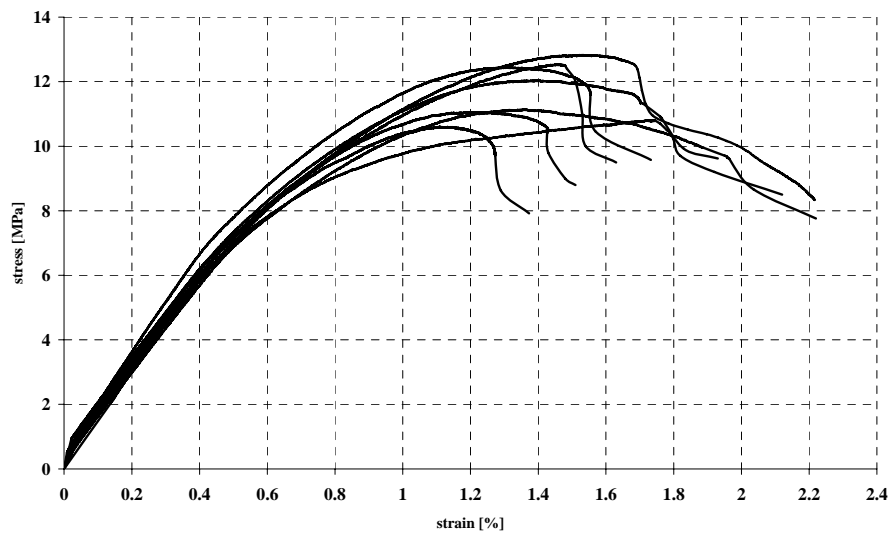


Figure 2.13: type 2 mortar stress-strain curve

<i>Prism</i>	<i>F_{max} [kN]</i>	<i>f [MPa]</i>
Sample 1	1924	2,92
Sample 2	1946	2,89
Sample 3	1542	2,33
Sample 4	1750	2,61
f _{ctm}		2,69
f _{ctk} =0.7f _{ctm}		1,88

Table 2.4: type 2 mortar traction strength

2.4 Experimental tests on bricks

2.4.1 Compression tests on hollow bricks

All the data collected by compression tests on hollow bricks are illustrated below, Figures 2.16 and 2.17 show respectively the *stress-strain* and *load-displacement* curve from compression test orthogonal to holes. In the same way figures 2.18 and 2.19 illustrate the curves related to compression parallel to holes.



Figure 2.14: hollow brick compression tests, compression orthogonal to holes (left); compression parallel to holes (right)

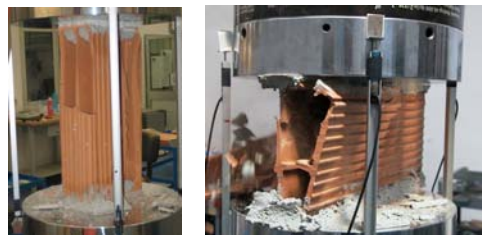


Figure 2.15: failure of a hollow brick sample compression orthogonal to holes (left); compression parallel to holes (right)

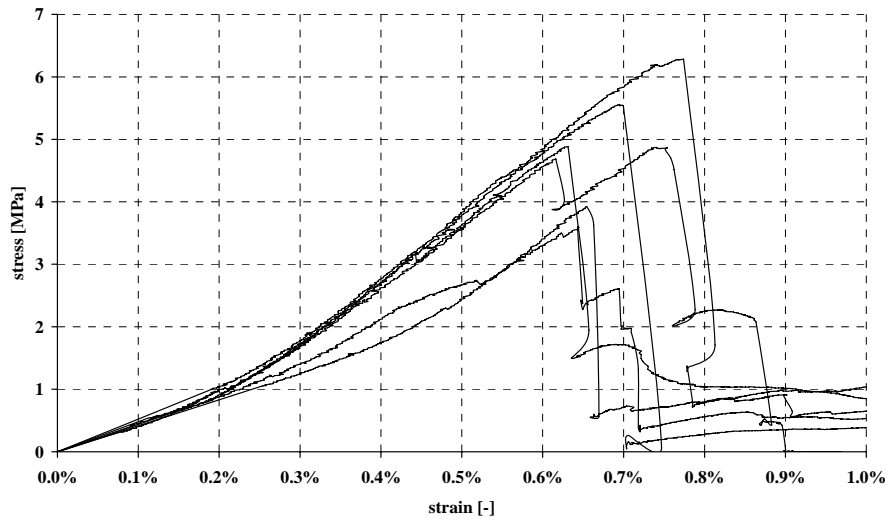


Figure 2.16: hollow bricks stress-strain curve, compression tests orthogonal to holes

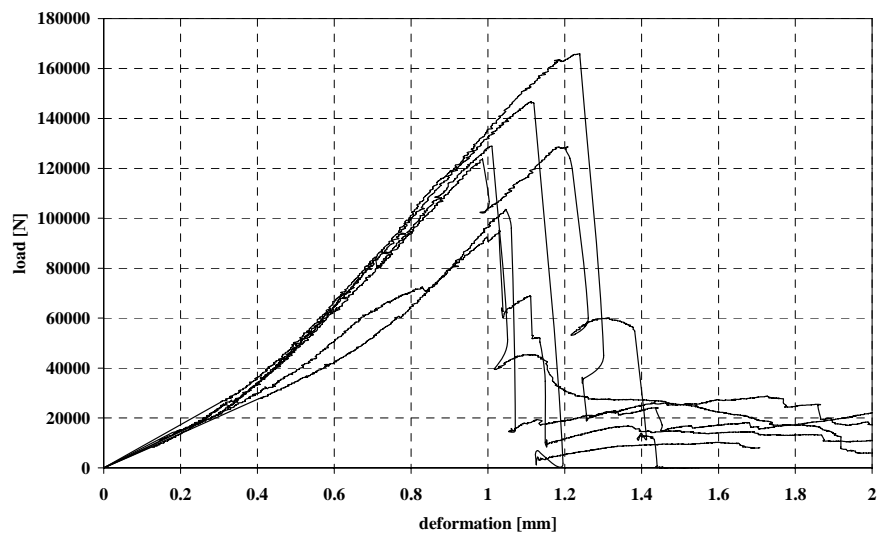


Figure 2.17: hollow bricks load-deformation curve, compression tests orthogonal to holes

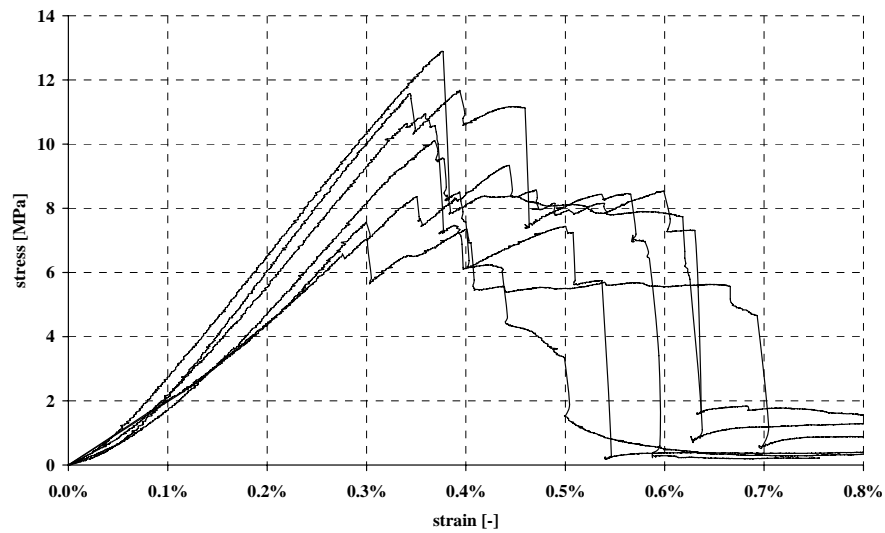


Figure 2.18: hollow bricks stress-strain curve, compression tests parallel to holes

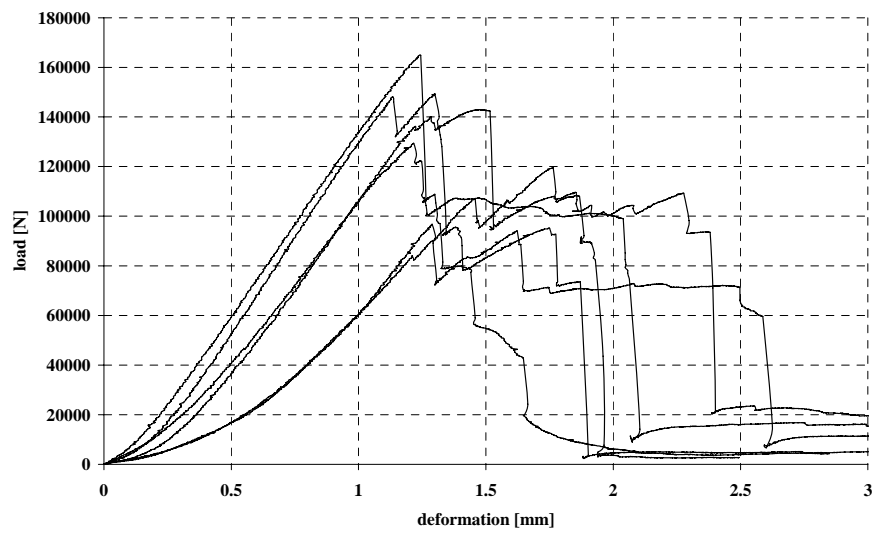


Figure 2.19: hollow bricks load-deformation curve, compression tests parallel to holes

<i>Brick</i>	<i>80x160x330</i>	<i>80x160x330</i>
	$f_{c,p}$ [MPa]	$f_{c,o}$ [MPa]
Sample 1	10,94	4,04
Sample 2	10,11	3,71
Sample 3	9,34	5,04
Sample 4	12,89	6,48
Sample 5	7,56	4,83
Sample 6	11,57	5,73
Average	10,4	4,97
Standard dev.	1,85	1,03
Minimum	7,56	3,71
Minimum	12,89	6,48
Interval	5,33	2,76

<i>Characteristic strength (Italian code)</i>	<i>Code reference</i>		
	<i>D.M. LL.PP. 20th November 1987</i>	7.32	4.97
	<i>D.M. LL.PP. 9th January 1996</i>	5.28	1.48
	<i>D.M. LL.PP. 14th September 2005</i>	7.28	3.48

*Table 2.5: compression tests on hollow bricks: summary of results
($f_{c,p}$ =compression strength parallel to holes; $f_{c,o}$ =compression strength
orthogonal to holes)*

2.4.2 Compression tests on half-full bricks

The data collected during the compression tests are presented below.

Figures 2.21 and 2.22 represent, respectively, the *stress-strain* and *load-displacement* curves from compression test orthogonal to holes, while Figures 2.23 and 2.24 refer to the compression test parallel to holes.



Figure 2.20: half-full bricks compression tests, compression parallel to holes (left); compression orthogonal to holes (right)



Figure 2.21: failure of a sample of half-full bricks, compression parallel to holes (right) and orthogonal holes (left)

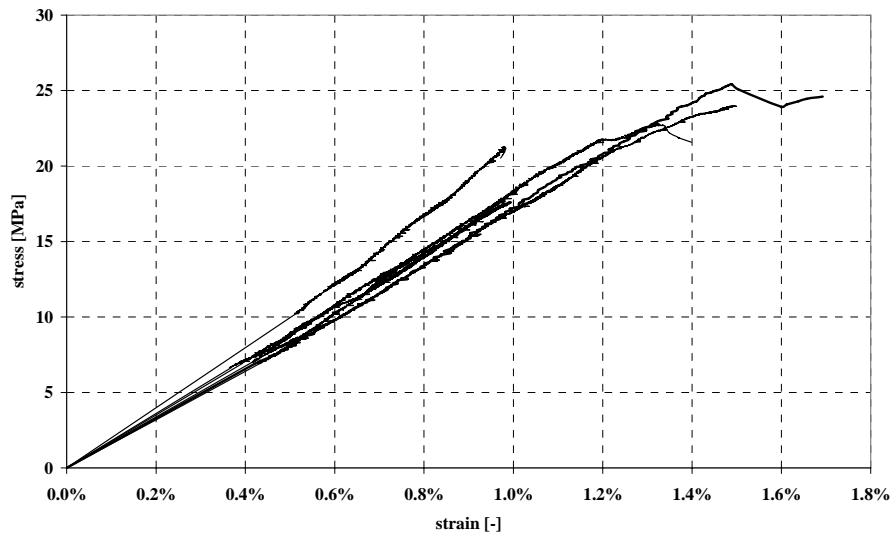


Figure 2.22: half-full bricks stress-strain curve, compression tests parallel to holes

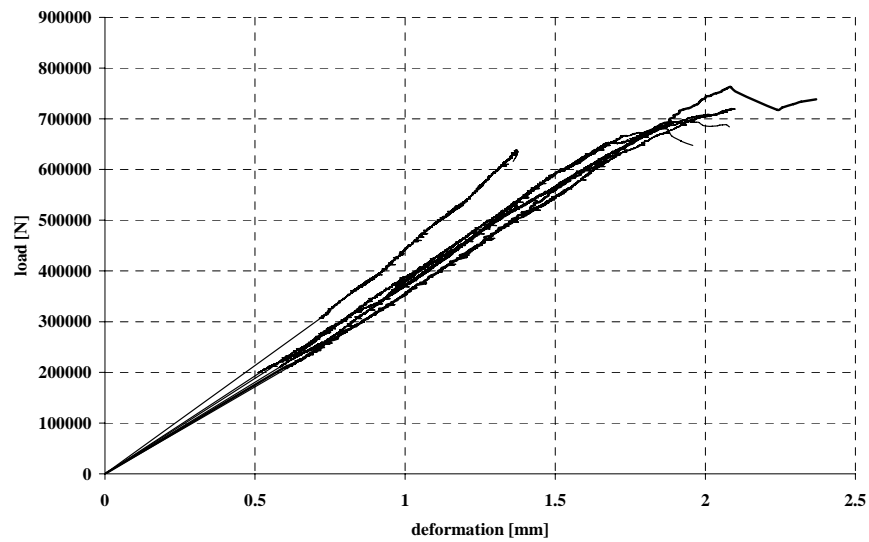


Figure 2.23: half-full bricks load-displacement curve, compression tests parallel to holes

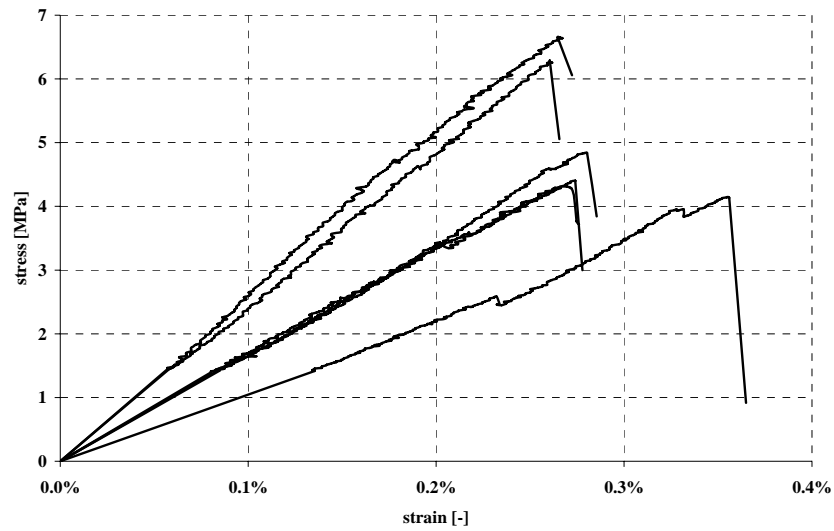


Figure 2.24: half-full bricks stress-strain curve, compression tests orthogonal to holes

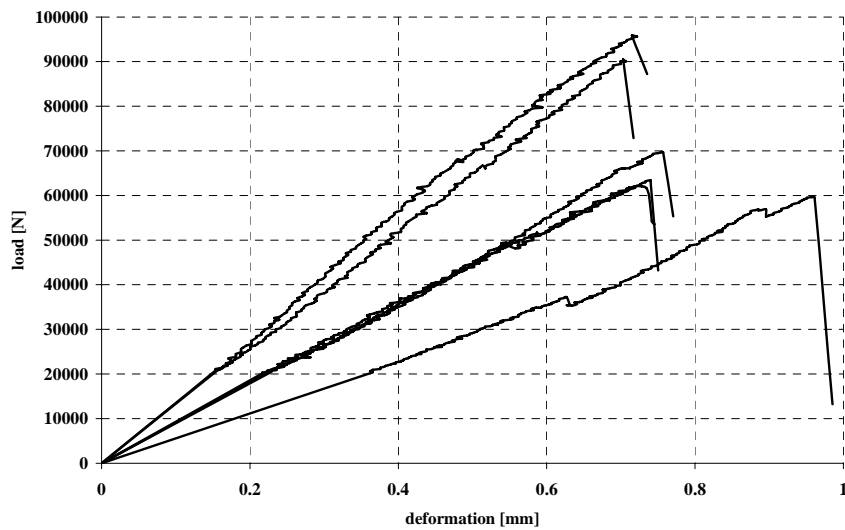


Figure 2.25: half-full bricks load-displacement curve, compression tests parallel to holes

<i>Brick</i>	<i>80x160x330</i>	<i>80x160x330</i>
	<i>$f_{c,p}$ [MPa]</i>	<i>$f_{c,o}$ [MPa]</i>
Sample 1	21,27	6,29
Sample 2	24,01	4,84
Sample 3	25,42	4,40
Sample 4	22,80	4,32
Sample 5	23,63	4,14
Sample 6	23,21	6,65
Average	23,39	5,11
Standard dev.	1,37	1,09
Minimum	21,27	4,14
Minimum	25,42	6,65
Interval	4,15	2,51

<i>Code reference</i>		
<i>D.M. LL.PP. 20th</i>		
<i>November 1987</i>	21,11	5,11
<i>D.M. LL.PP. 9th</i>		
<i>January 1996</i>	514,73	1,58
<i>D.M. LL.PP. 14th</i>		
<i>September 2005</i>	16,37	3,58

Table 2.6: compression tests on half-full bricks: summary of results
($f_{c,p}$ =compression strength parallel to holes; $f_{c,o}$ =compression strength
orthogonal to holes)

2.5 Experimental tests on walls

The wall specimens have been built using the bricks presented in the previous paragraphs. With type 1 mortar twelve walls ($101 \times 101 \times 80 \text{ cm}^3$) have been built using hollow bricks, twelve ($77 \times 77 \times 12 \text{ cm}^3$) using half-full bricks, and twelve double panel walls ($101 \times 101 \text{ cm}^3$ on walls plane and 26 cm depth including a 6 cm air space) coupling the previous walls,. With type 2 mortar other twelve walls ($77 \times 77 \times 12 \text{ cm}^3$) of half-full bricks have been built. All of the walls characterised by constant bed-joints of approximately 10 mm in thickness, have been built by an expert workman with a level of accuracy that can be compared with the procedure commonly used on building sites. The samples have turned out to be well

done but they still have some defects. Walls construction was performed directly on wood bases in order to allow an easy movement. The loading surfaces have been levelled applying a layer of high resistance mortar in order to create smooth and parallel surfaces. Figures 26 and 27 illustrate the walls built in the *Laboratory of experiments on materials and structures* of the University of Roma Tre.



Figure 2.26: walls specimens, walls of half-full bricks (left), walls of hollow bricks (right)

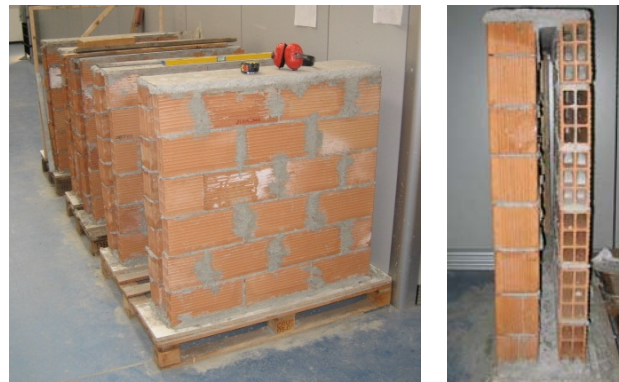


Figure 2.27: double panel walls, specimens ready to be tested (left), side view of double panel wall (right)

After a period exceeding 28 days, the samples were subject to compression tests; of the twelve samples available for each typology, 4 have been loaded parallel to holes, 4 orthogonally to holes and 4 diagonally.

Test equipment

A *Metrocom* press, that can perform compression tests with a defined loading rate, has been used to test walls. Experiments were carried out by applying an increasing monotonic load up to panel failure. The loading speed adopted was 1.6 kNs^{-1} for both of the main compression directions and equivalent to 0.8 kNs^{-1} for the diagonal compression. The load applied has been monitored with an external loading cell equipped with a spherical joint in order to avoid accidental loading eccentricities. In order to guarantee a uniform load distribution on sample faces, two *HEB 300* steel trusses (Figure 2.28), sufficiently stiff in order to guarantee a uniform load distribution, have been inserted between wall and press plates; the equipment is shown in Figures 2.28, 2.29, 2.30. Panels in the diagonal compression test have been inserted between two steel supports specifically designed to transfer load in correspondence with sample corners (Figure 2.29).

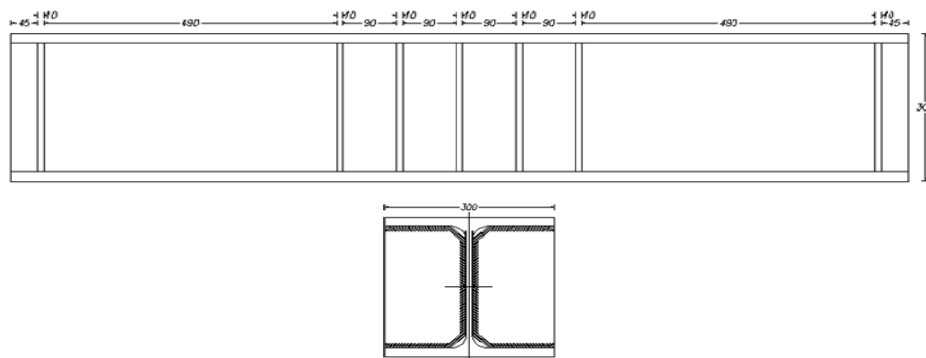


Figure 2.28: steel profile used to transfer the compression load on walls

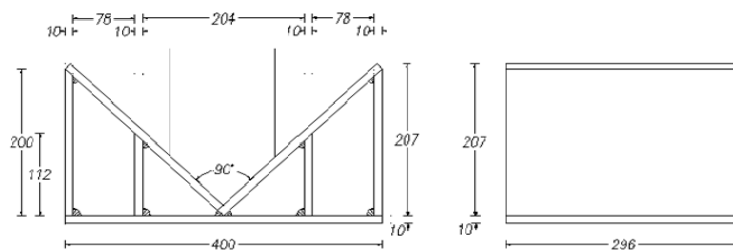


Figure 2.29: steel saddle used to settle the walls diagonally

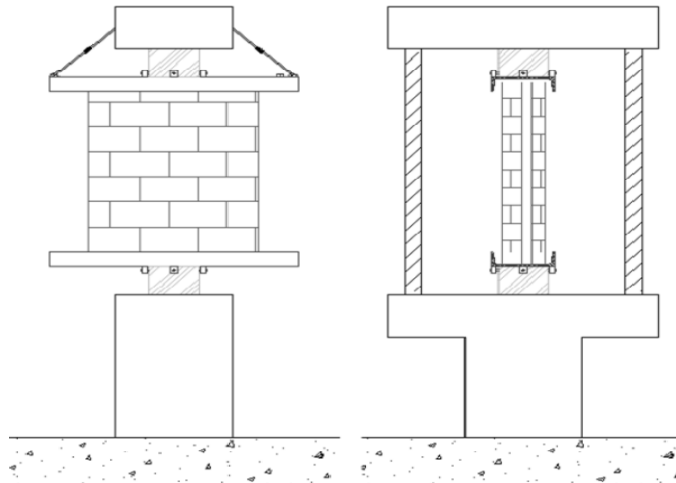


Figure 2.30: vertical compression test, layout of test systems

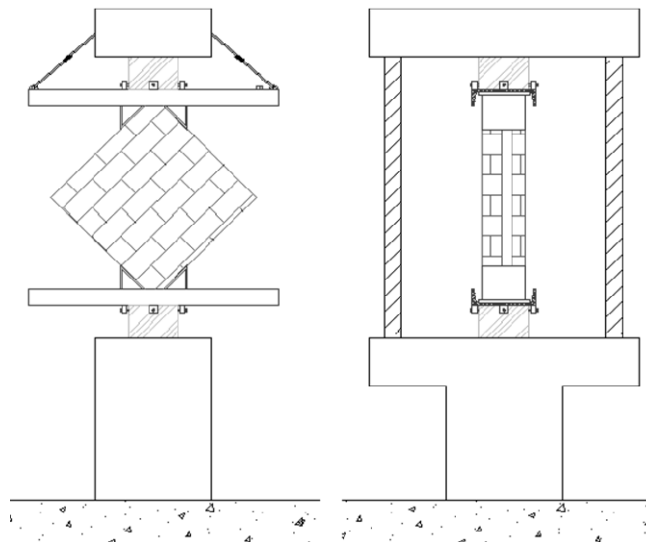


Figure 2.31: diagonal compression test, layout of test system



Figure 2.32: equipment set up for vertical compression tests: the steel profiles fitted onto the Metrocom 3000 kN press (left), a wall ready to be crashed inside the press (right)



Figure 2.33: diagonal compression tests set up, steel supports for diagonal compression tests (left), wall ready to be crashed inside the press (right)



Figure 2.34: suspension system of the upper steel profile

The lower profile, in direct contact with the press piston, has been centred and its position has been checked before each test. Also with regards to the upper profile, connected by chains to the press, the perfectly horizontal position has been constantly controlled by calibrating chains length (Figure 2.34).

With the aim of determining panels deformation, displacement transducers (Figure 2.35) have been positioned; transducer's ends, fitted with spherical joints, have been connected to steel bars inserted in mortar layers.

As illustrated in Figure 2.35, a displacement transducer (in the following *external transducer*) has been installed in correspondence with the mobile plate of the press in order to measure vertical plate's translation; the deformation identified through this instrument coincides with the *global* deformation of the wall sample, that is affected by interface conditions between wall and loading plates that approximately can be compared to the what occurs between the infill-frame interface.

The position of the instruments installed directly on the walls (in the following) is represented in Figures 35 and 43. Measurement from all transducers has been performed at a frequency of 0.1 Hz.



Figure 2.35: transducer adopted to measure deformations (left), the external transducer installed (right)

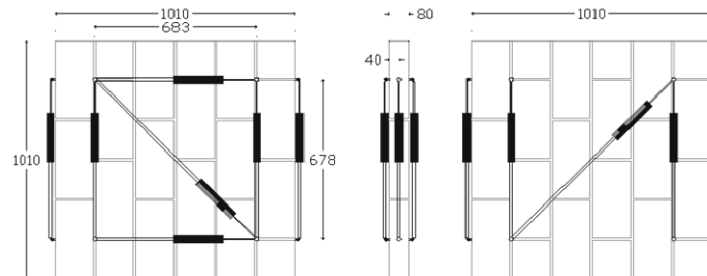


Figure 2.36: hollow brick panels layout of sensors on the wall compressed parallel to holes [mm]

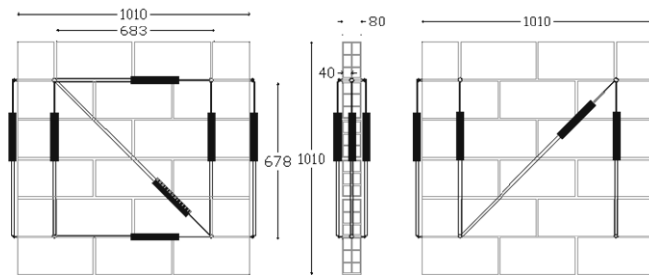


Figure 2.37: hollow brick panels layout of sensors on the wall compressed orthogonally to holes [mm]

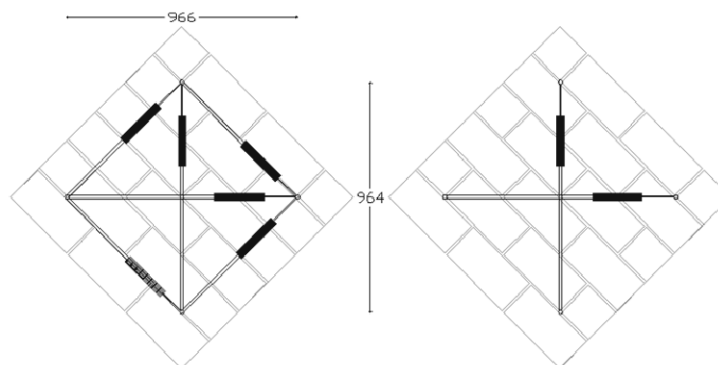


Figure 2.38: hollow brick panels layout of sensors on the wall compressed diagonally [mm]

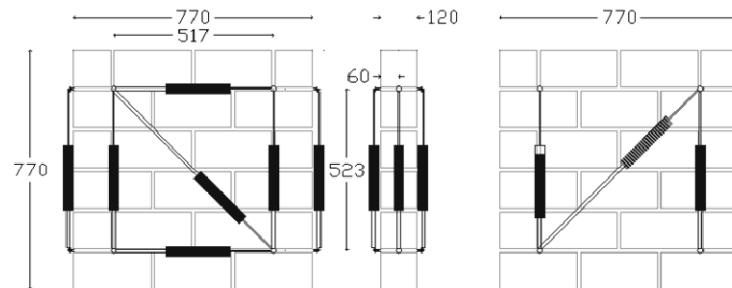


Figure 2.39: half-full brick panels layout of sensors on the wall compressed parallel to holes [mm]

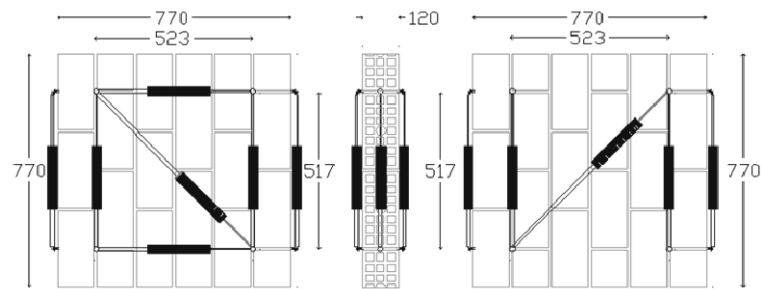


Figure 2.40: half-full brick panels layout of sensors on the wall compressed orthogonally to holes [mm]

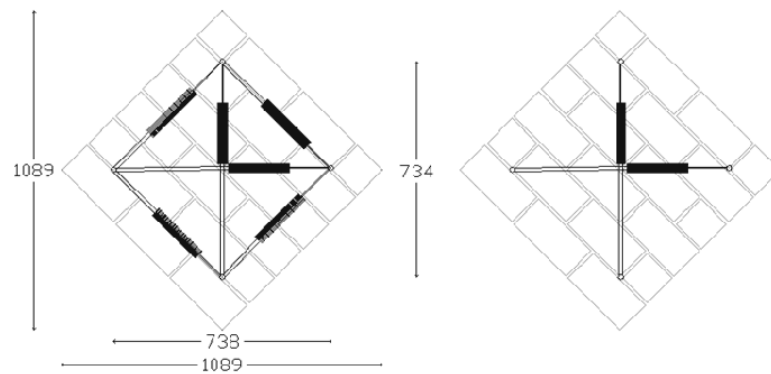


Figure 2.41: half-full brick panels layout of sensors on the wall compressed diagonally [mm]

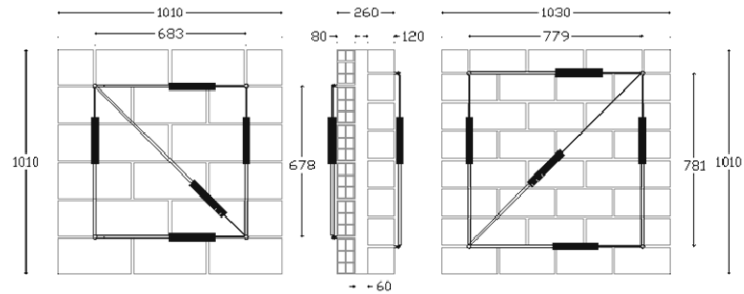


Figure 2.42: double panel walls layout of sensors on the wall compressed parallel to holes [mm]

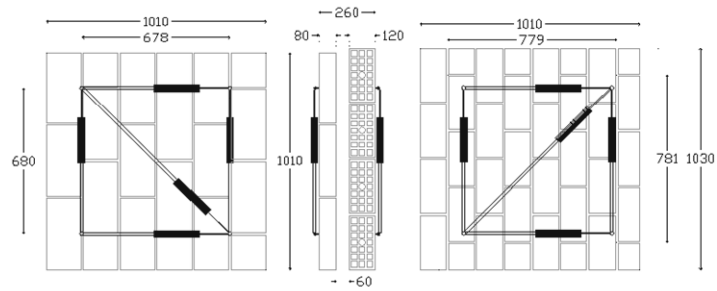


Figure 2.43: double panel walls layout of sensors on the wall compressed orthogonally to holes [mm]

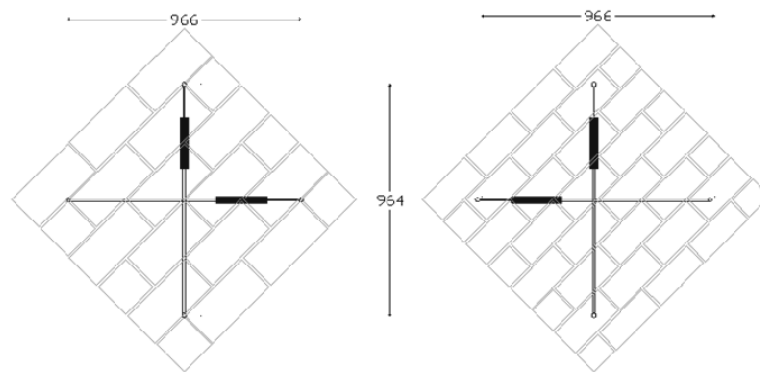


Figure 2.44: double panel walls layout of sensors on the wall compressed diagonally [mm]



Figure 2.45: equipment for compression test parallel to holes on hollow brick walls (front and back view of the panel)

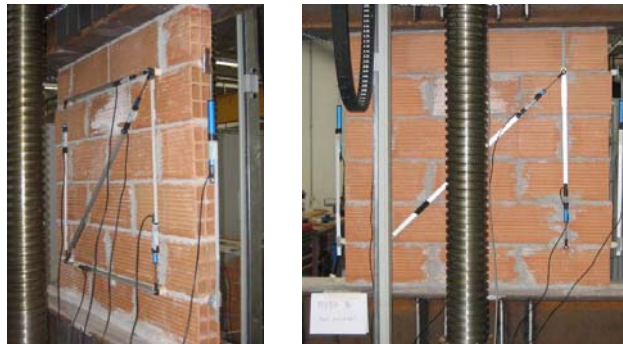


Figure 2.46: equipment for compression test orthogonal to holes on hollow brick walls (front and back view of the panel)

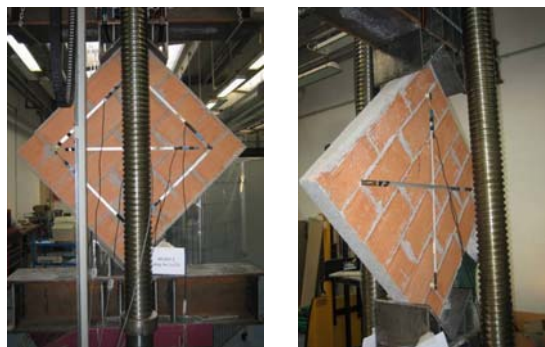


Figure 2.47: equipment for diagonal on hollow brick walls (front and back view of the panel)

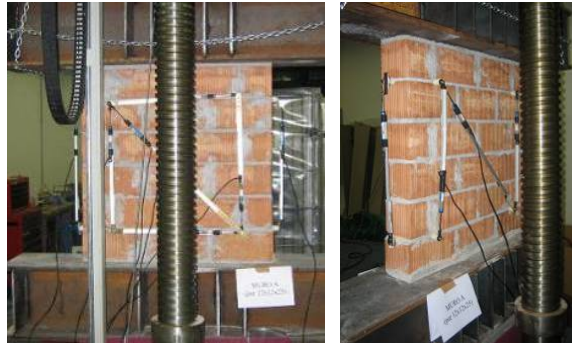


Figure 2.48: equipment for compression test parallel to holes on half-full brick walls (front and back view of the panel)



Figure 2.49: equipment for compression test orthogonal to holes on half-full brick walls (front and back view of the panel)



Figure 2.50: equipment for diagonal compression test half-full brick walls (front and back view of the panel)



*Figure 2.51: equipment for vertical compression on double panel walls
(front and back view of the panel)*



*Figure 2.52: equipment for horizontal compression on double panel walls
(front and back view of the panel)*



*Figure 2.53 equipment for diagonal compression on double panel walls
(front and back view of the panel)*

The following paragraphs describe the experimental results achieved. In this thesis the following symbols are adopted: f_{wv} and f_{wh} are the compression strength in a vertical and horizontal direction respectively calculated as follows:

$$f_{wv} = F / (l \cdot t) \quad \text{Eq. 2.3}$$

$$f_{wh} = F / (h \cdot t) \quad \text{Eq. 2.4}$$

with t , l and h representing thickness, length and height of the walls.

The wall shear strength (f_{wo}) has been determined from diagonal compression tests as the average value of the tangential stress acting parallel to wall's sides corresponding to maximum load F : in accordance with *ASTM E519-81* standards the following has been adopted:

$$f_{wo} = F / (\sqrt{2} \cdot l \cdot t) \quad \text{Eq. 2.5}$$

In the following the symbols E_v , E_h and E_d have been used to indicate vertical, horizontal and diagonal elastic modules while G_w is the shear modulus whose expression is:

$$G_w = f_{wo} / \gamma_w \quad \text{Eq. 2.6}$$

where:

$$\gamma_w = \frac{\varepsilon_{w1} - \varepsilon_{w2}}{2} \quad \text{Eq. 2.7}$$

with ε_{w1} and ε_{w2} being the strains in parallel and orthogonal to load directions.

For the two typologies of bricks adopted, vertical or horizontal loading directions have a different meaning.

In reality the walls made from hollow bricks are built with a horizontal holes, on the other hand half-full bricks have been placed with vertical holes.

For these reasons, for the double panel walls the vertical load refers to loading orthogonally to hollow brick holes or parallel to half-full brick holes: in the following the half-full bricks will be adopted as a reference element.

2.6 Experimental test results on hollow brick and type 1 mortar walls

This paragraph describes the experimental results achieved for hollow brick walls.

By examining the entire development of each test performed, it has been observed that collapse occurs after the detachment of the external parts of blocks due to the first cracks developing on the wall's tight side, in fact these walls, due to their high slenderness inflects under vertical load: in some cases the walls quickly buckle preventing vision of any other mechanism.

In diagonal compression tests collapse occurs due to diffusion of a pseudo-vertical crack that begins at the panel's centre, corresponding to maximum traction stress, and crosses the entire panel side to side; cracks distribution didn't indicate a compressed strut resisting mechanism.

Figures from 2.57 to 2.62 represent *load-displacement* and *stress-strain* curves of samples for all of the compression directions.

Deformations have been determined by measuring relative displacement between the press plates referring to *external transducer*, any other analysis aimed to identifying panel's characteristics, depurated from wall-press interface effects have been determined referring to *internal transducers*.

The mechanical behaviour of panels is *elastic-brittle*, the collapse occurred at maximum strength, the wall didn't offer any residual resistance. Stiffness determined for both of the main loading directions (parallel and orthogonal to holes) is almost the same despite of a 50% increase of parallel to holes strength compared to orthogonal to holes strength.

Tests performed on these walls have highlighted scattered strength values; this result can be correlated with the large number of variables that may influence panel characteristics: relevant peculiarities are the high slenderness and the inevitable imperfections that make of each wall a single element.

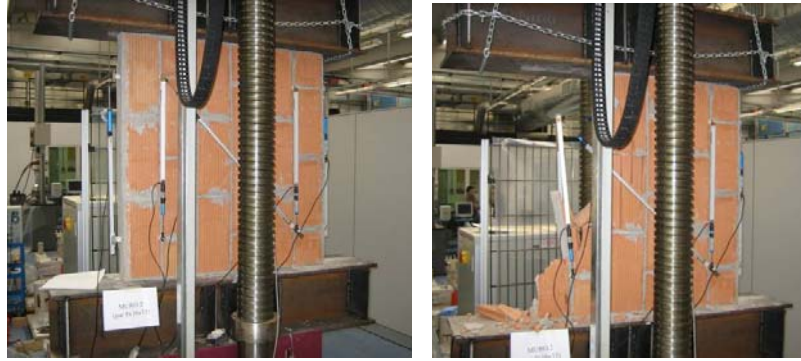


Figure 2.54: compression test parallel to holes, initial phase and collapse



Figure 2.55: compression test orthogonal to hole, initial phase and collapse



Figure 2.56: diagonal compression test, front and side collapse view

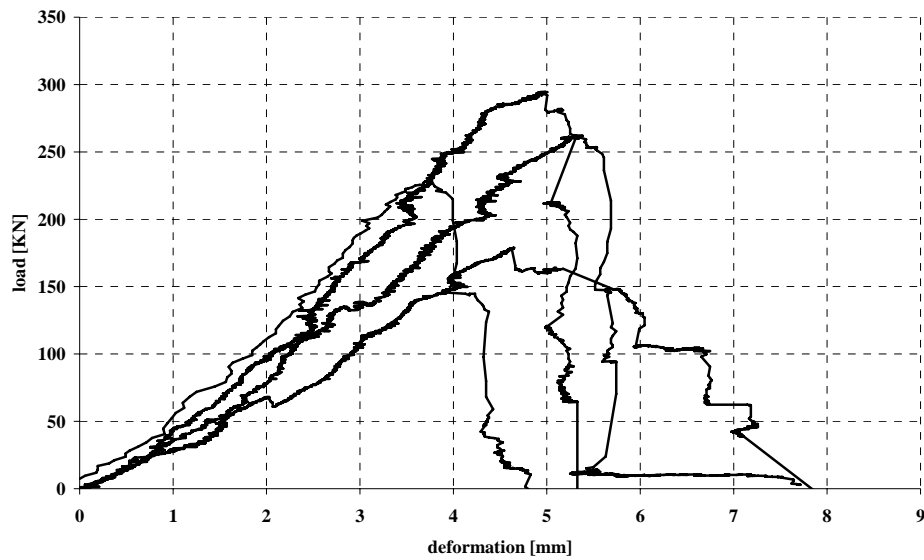


Figure 2.57: compression tests parallel to holes, load-displacement curves of walls of hollow brick and type 1 mortar

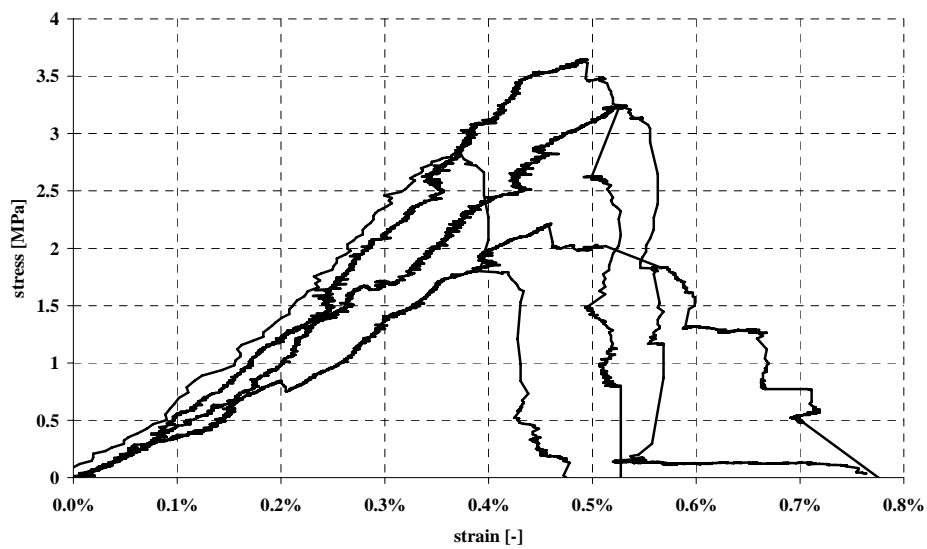


Figure 2.58: compression tests parallel to holes, stress-strain curves of walls of hollow brick and type 1 mortar

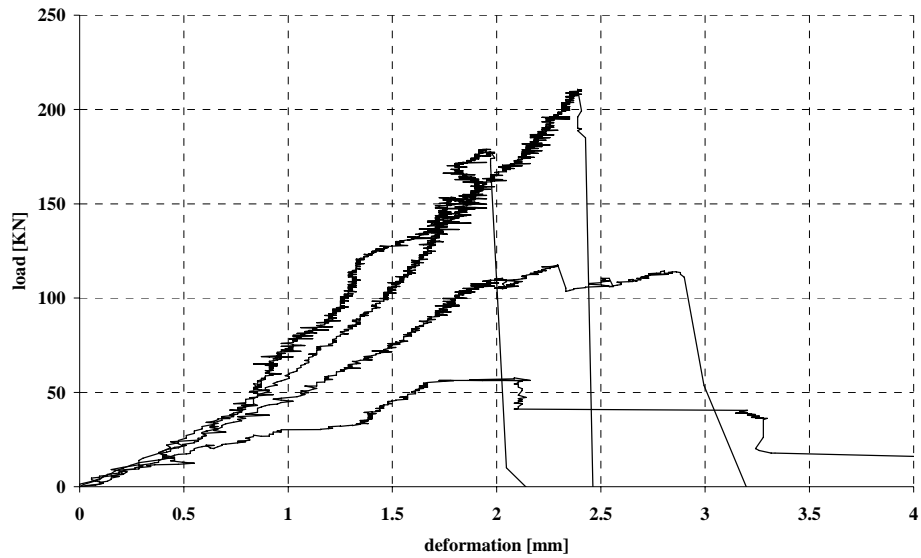


Figure 2.59: compression tests orthogonal to holes, load-displacement curves of walls of hollow brick and type 1 mortar

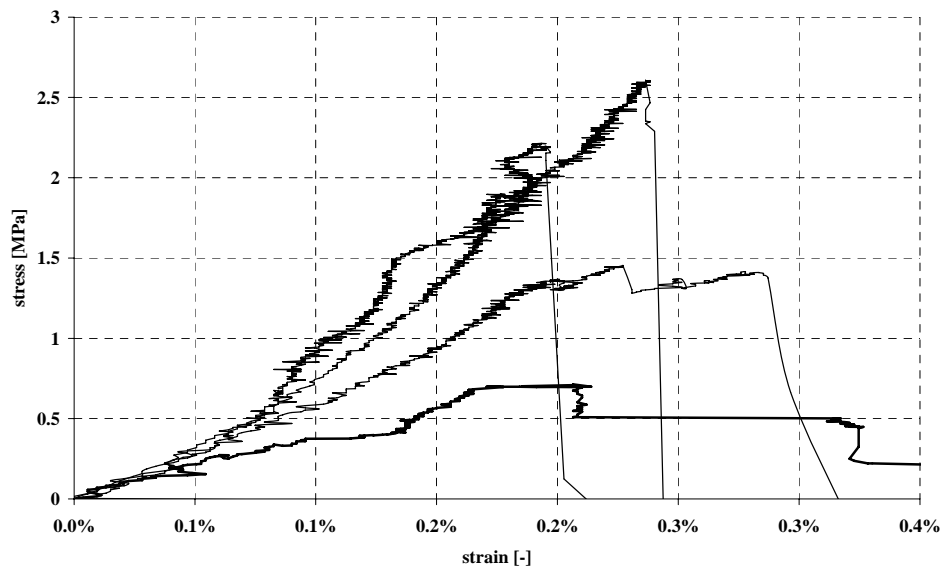


Figure 2.60: compression tests orthogonal to holes, stress-strain curves of walls of hollow brick and type 1 mortar

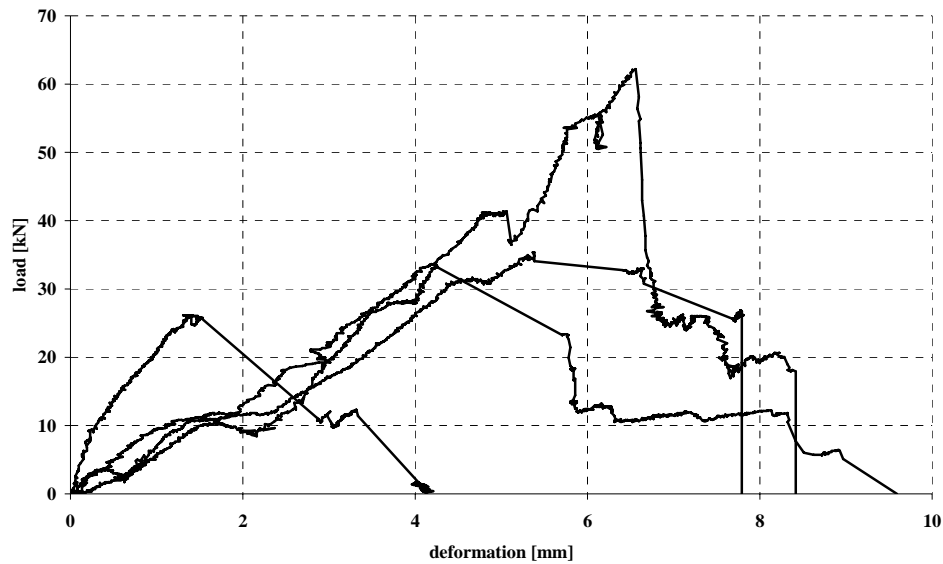


Figure 2.61: diagonal compression tests, load-displacement curves of walls of hollow brick and type 1 mortar

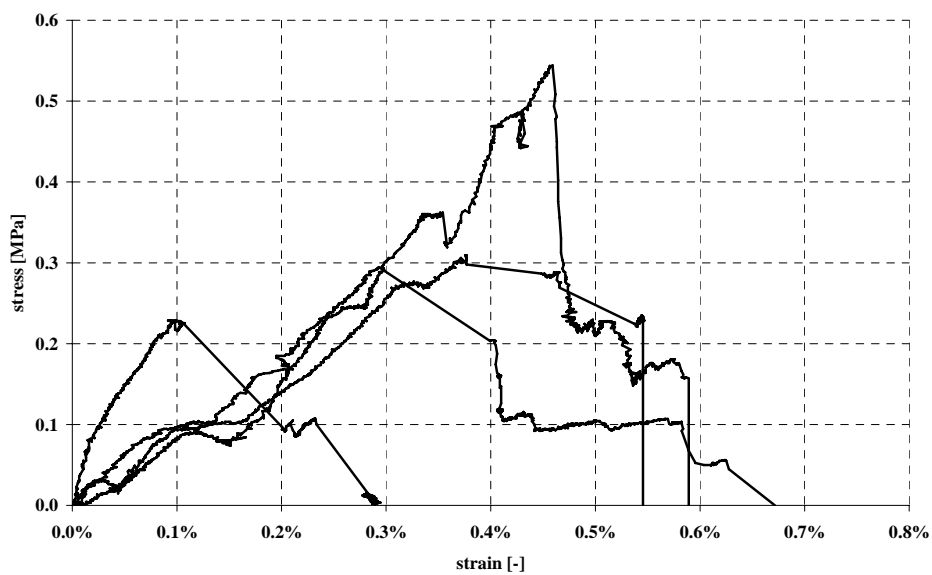


Figure 2.62: diagonal compression tests, stress-strain curves of walls of hollow brick and type 1 mortar

Tables 2.7, 2.8 and 2.9 summarize compression test results in terms of maximum load F , characteristic strength f_k and elastic modulus E as well as their relative average values. In absence of specific indications, the value of elastic modulus E has been calculated along the linear branch between stresses of approximately 25% and 50% of the maximum stress. Walls diagonal strength f_{v0} has been determined as the ratio between maximum load and the area section orthogonal to the corresponding loading direction: its characteristic value has been determined according to the following formula: $f_{vk0}=0,7 \times f_{v0}$.

The results achieved from measurements of *internal transducers* are now presented.

The internal deformations have been calculated as the average value of measurements of all six vertical potentiometers (two on one side, two on the opposite and two laterally).

The values measured by the *internal transducers* are very different from what has been determined referring to *external transducers*.

The feasibility of data acquired may be affected by the numerous variables that influence measurements, a relevant font of disturbance consists in the installation details especially the wall-transducers connections.

In Figure 2.63 and 2.64 the average values of the elastic modulus and of maximum vertical deformation have been compared, estimated with the external transducer or with those inside the panel.

<i>Sample</i>	<i>F</i> [kN]	<i>f_{wh}</i> [MPa]	<i>E_h</i> [MPa]
1	229.63	2.84	761
2	277.39	3.43	567
3	193.27	2.39	429
4	304.19	3.76	683
<i>Average</i>	251.12	3.11	610

Table 2.7: results of compression tests parallel to holes on hollow bricks walls

<i>Sample</i>	<i>F</i> [kN]	<i>f_{wv}</i> [MPa]	<i>E_v</i> [MPa]
1	70.69	0.87	1013
2	189.20	2.34	1040
3	224.20	2.77	986
4	128.96	1.60	751

Table 2.8: results of compression tests orthogonal to holes on hollow brick walls

<i>Sample</i>	<i>F</i> [kN]	<i>f_{v0}</i> [MPa]	<i>f_{vk0}</i> [MPa]
1	34.94	0.31	0.21
2	62.22	0.54	0.38
3	26.39	0.23	0.16
4	37.87	0.33	0.23
<i>average</i>	40.35	0.35	0.25

Table 2.9: results of diagonal compression tests on hollow brick walls

<i>Load parallel to the holes</i>		<i>Load orthogonal to the holes</i>	
<i>Sample</i>	<i>E</i> [MPa]	<i>Sample</i>	<i>E</i> [MPa]
1	4250	1	4400
2	4018	2	7053
3	2867	3	3349
4	6167	4	4415
Average	4326	Average	4804

Table 2.10: elastic modulus determined from internal transducers

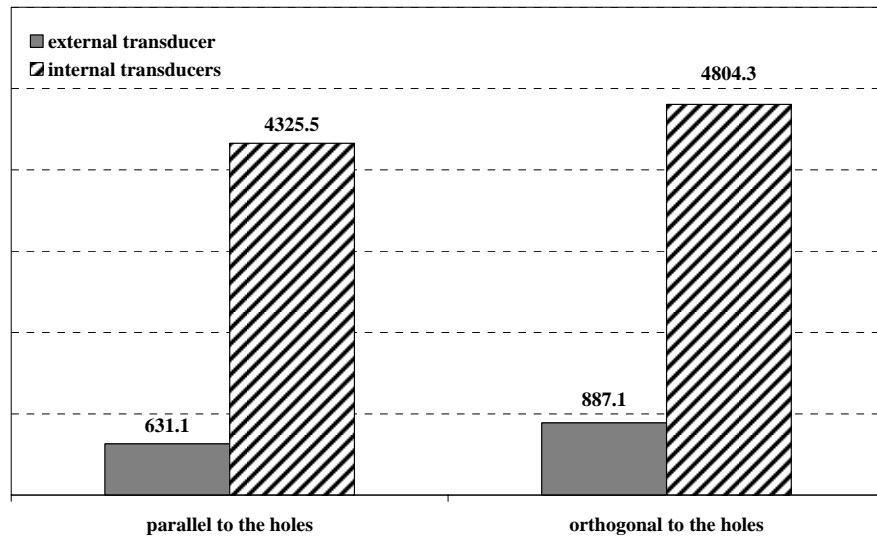


Figure 2.63: comparison between average elastic modulus determined from internal or external transducers [MPa]

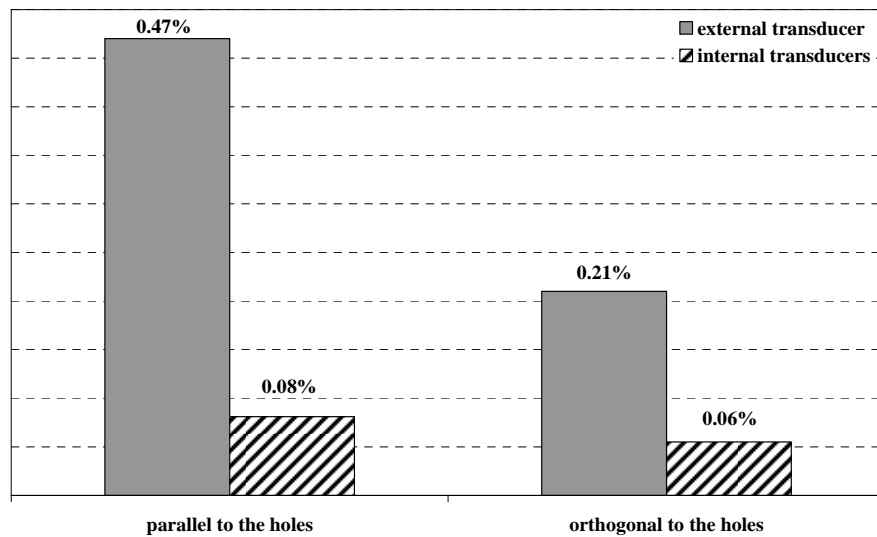


Figure 2.64: comparison between maximum strains determined from internal or external transducers [-]

Characteristics of previously described walls are summarized below:

Compression strength

f_{wv}	1.90	MPa	Vertical direction
f_{wh}	3.11	MPa	Horizontal direction
f_{wo}	0.35	MPa	Diagonal direction

Maximum strains

e_v	0.55	‰	Vertical direction
e_h	0.81	‰	Horizontal direction
e_o	1.17	‰	Diagonal direction

Elastic modulus

E_v	4804.2	MPa	Vertical direction
E_h	4325.5	MPa	Horizontal direction
E_o	2900.0	MPa	Diagonal direction
G_w	500.0	MPa	Shear modulus

Poisson coefficient

n_v	0.36
-------	------

Ratio between f and E

f_{wv} / E_v	0.40	‰
f_{wh} / E_h	0.72	‰
f_{wo} / E_o	0.12	‰

Table 2.11: characterization of infill wall of hollow bricks type 1 mortar

2.7 Experimental test results on half-full bricks and type 1 mortar walls

As similarly performed before for samples wall built using hollow bricks, this paragraph describes the results from compression tests performed on walls built using half-full bricks and type 1 mortar: the testing procedures are the same described for the previous type of wall.

Figures 2.65, 2.66 and 2.67 illustrate, as an example, some samples during compression tests while Figures from 2.68 to 2.72 describe the results achieved. The experimental data has highlighted an elastic behaviour with brittle failure; a low residual strength has been recorded. The residual strength may mainly be attributed to contribution offered by fragments of bricks that are held by mortar flown through holes of bricks themselves; this phenomenon is much more important in orthogonal to holes compression tests. In reality, for this kind of bricks the dimension of holes is sufficiently limited to be saturated by mortar that, due to gravity, drips inside during construction. For horizontal compression, it has been observed a first failure followed by a residual resistance determined by the cooperation of brick's fragments and mortar flown in brick's holes.

From vertical compression tests, the resistance achieved is relatively higher and the residual resistance has not been observed due to violence of the first collapse that destroyed the wall.

Furthermore it is clear that in the main loading directions, deformations towards collapse can be compared while the maximum load achieved varies by approximately 60%; the strong direction is once again parallel to holes.

The wall collapse is typically manifested by detachment of external bricks sides. No instability mechanisms have been registered in any of the experiments carried out.

For diagonal compression, wall failure occurs due to the diffusion of two parallel cracks that limit a central compressed strut.

It is clear that the effects of confinement, as well as a reinforced concrete framing, can drastically improve wall's strength particularly for this load direction: the collapse occurs following detachment of one of the free wall's ends where it is not connected with the loading support.



Figure 2.65: compression test parallel to holes, initial phase and collapse



Figure 2.66: compression test orthogonal to holes, initial phase and collapse



Figure 2.67: diagonal compression test, initial phase and collapse

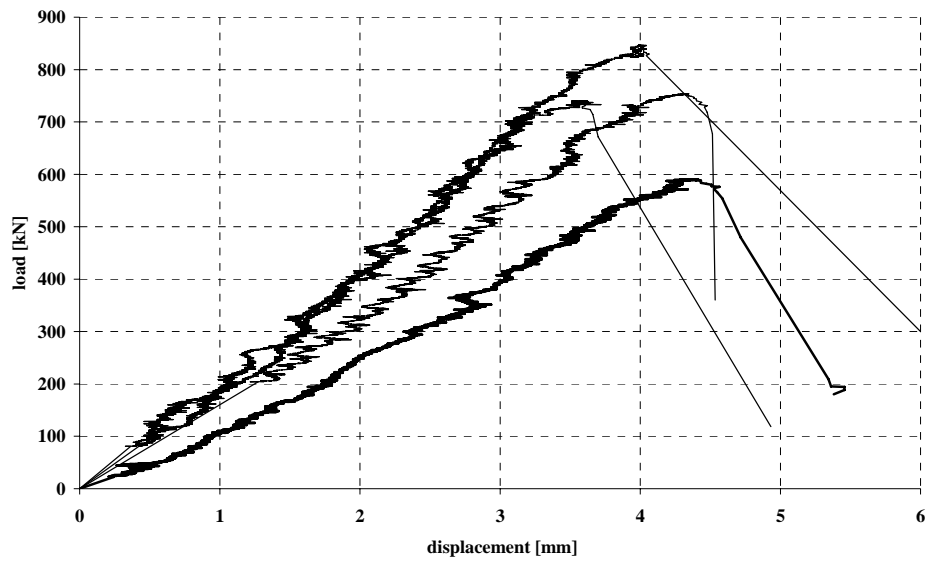


Figure 2.68: compression tests parallel to holes, load-displacement curves of walls of half-full bricks and type 1 mortar

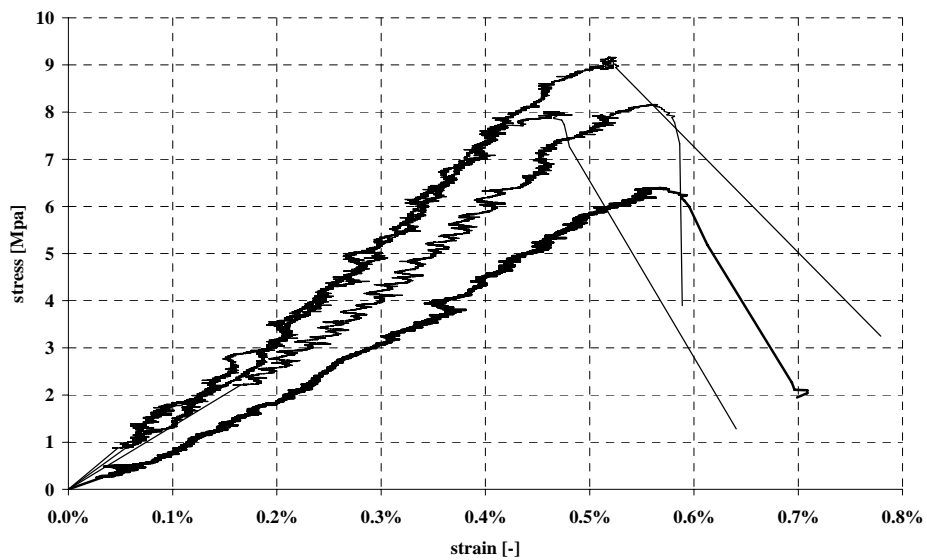


Figure 2.69:: compression tests parallel to holes, stress-strain curves of walls of half-full bricks and type 1 mortar

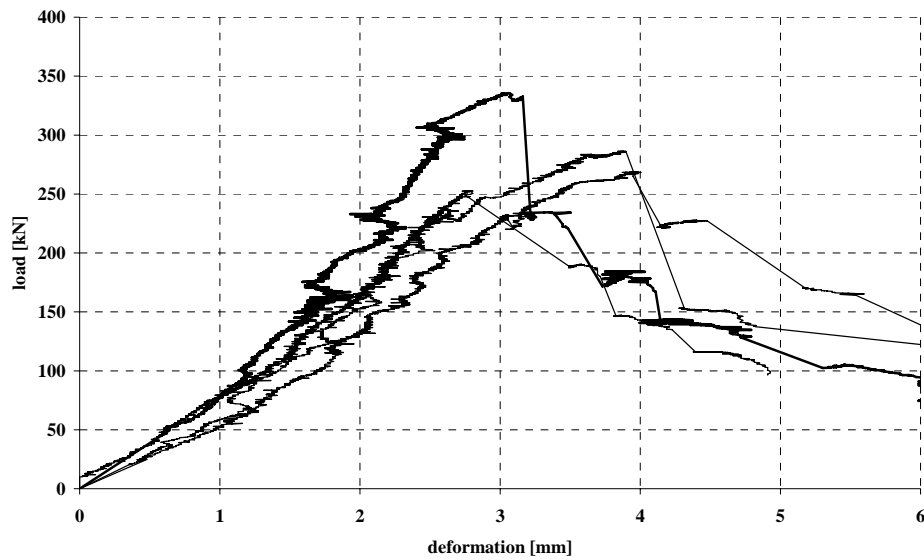


Figure 2.70: compression tests orthogonal to holes, load-displacement curves of walls of half-full bricks and type 1 mortar

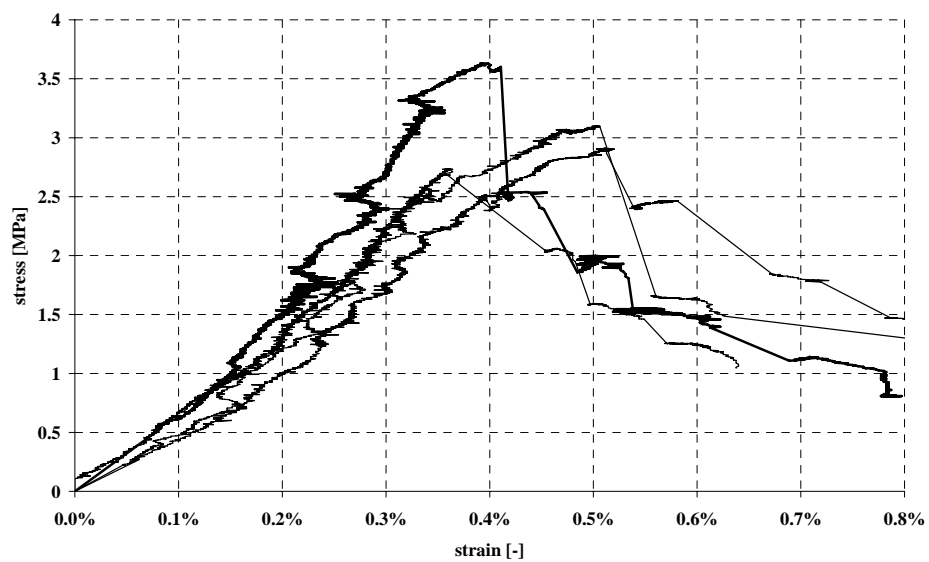


Figure 2.71: compression tests orthogonal to holes, stress-strain curves of walls of half-full bricks and type 1 mortar

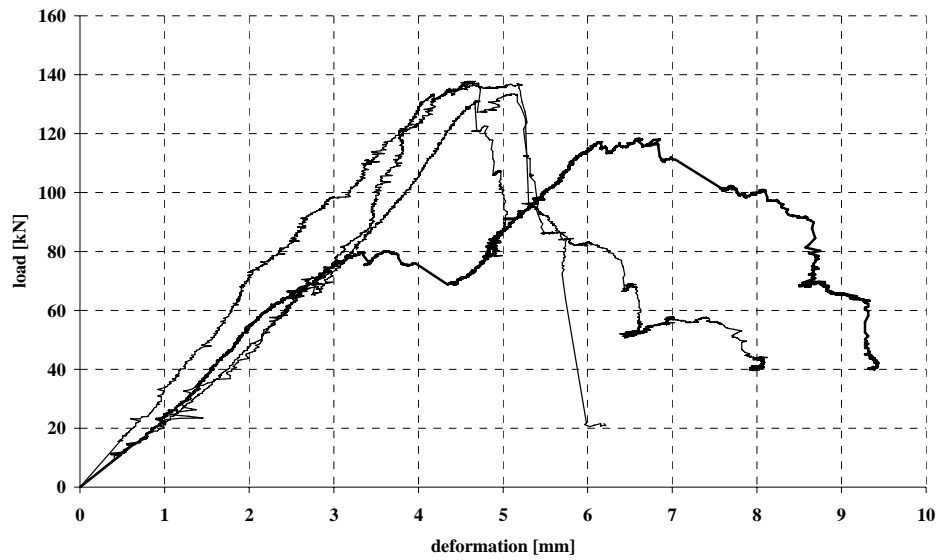


Figure 2.72: diagonal compression tests, load-displacement curves of walls of half-full bricks and type 1 mortar

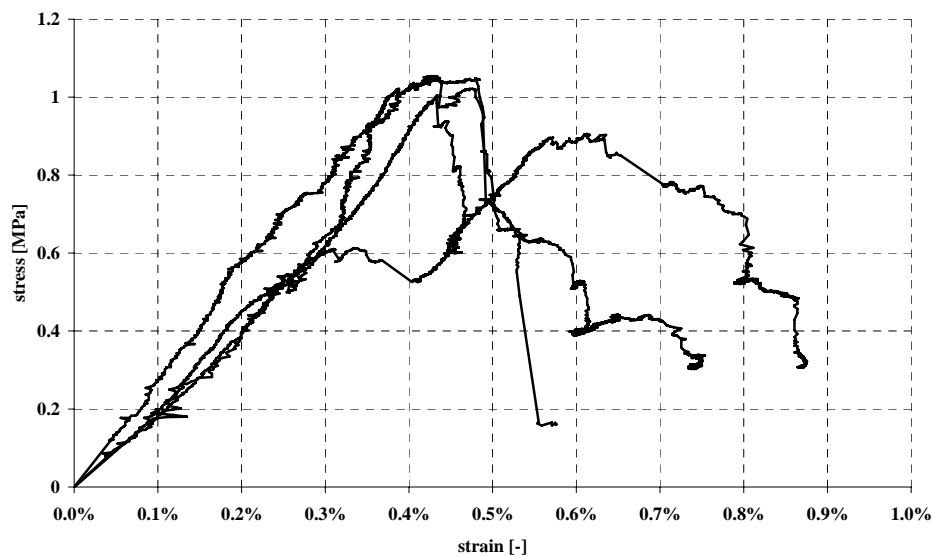


Figure 2.73: diagonal compression tests, stress-strain curves of walls of half-full bricks and type 1 mortar

Tables 2.12, 2.13 and 2.14 illustrate results from compression tests on half-full brick walls in the three loading directions: maximum load F , characteristic strength f_k , elastic modulus E and the relative average values. Strength and elastic modulus have been estimated as already done for the walls previously described. Also in this case the internal elastic modulus have been calculated well above the values obtained from the transducer external to the walls.

<i>Sample</i>	<i>F [kN]</i>	<i>f_{wv} [MPa]</i>	<i>E_v [MPa]</i>
1	590,2	6,4	1286,7
2	846,3	9,2	2148,8
3	739,9	8,0	1984,4
4	753,9	8,2	1470,2
Average	732,6	7,9	1722,6

Table 2.13: results of compression tests parallel to holes on half-full brick walls

<i>Sample</i>	<i>F [kN]</i>	<i>f_{wh} [MPa]</i>	<i>E_h [MPa]</i>
1	335,5	3,6	1091,2
2	286,2	3,1	759,0
3	252,9	2,7	734,0
4	269,1	2,9	755,7
Average	285,9	3,1	835,0

Table 2.14: results of compression tests orthogonal to holes on half-full brick walls

<i>Sample</i>	<i>F [kN]</i>	<i>f_{v0} [MPa]</i>	<i>f_{vk0} [MPa]</i>
1	118,3	0,9	0,6
2	136,5	1,0	0,7
3	131,2	1,0	0,7
4	137,7	1,0	0,7
Average	118,3	0,9	0,6

Table 2.15: results of diagonal compression tests on half-full brick walls

<i>Load parallel to the holes</i>		<i>Load orthogonal to the holes</i>	
<i>Sample</i>	<i>E[MPa]</i>	<i>Sample</i>	<i>E[MPa]</i>
1	11927	1	9507
2	10203	2	3542
3	11390	3	2937
4	7151	4	3567
Average	10168	Average	4888

Table 2.16: elastic modulus determined from internal transducers

Figures 2.74 and 2.75 compare elastic modulus and maximum strains obtained from internal and external transducers.

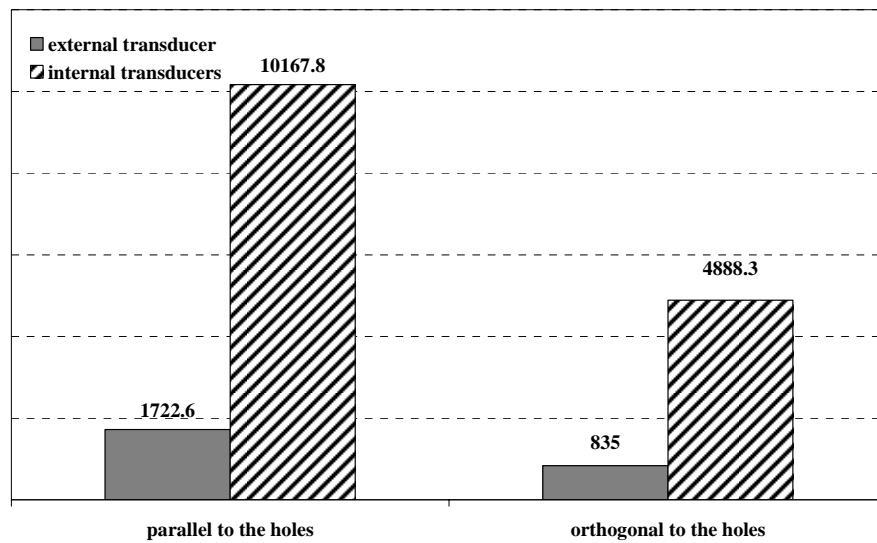


Figure 2.74: comparison between average elastic modulus determined from internal or external transducers [MPa]

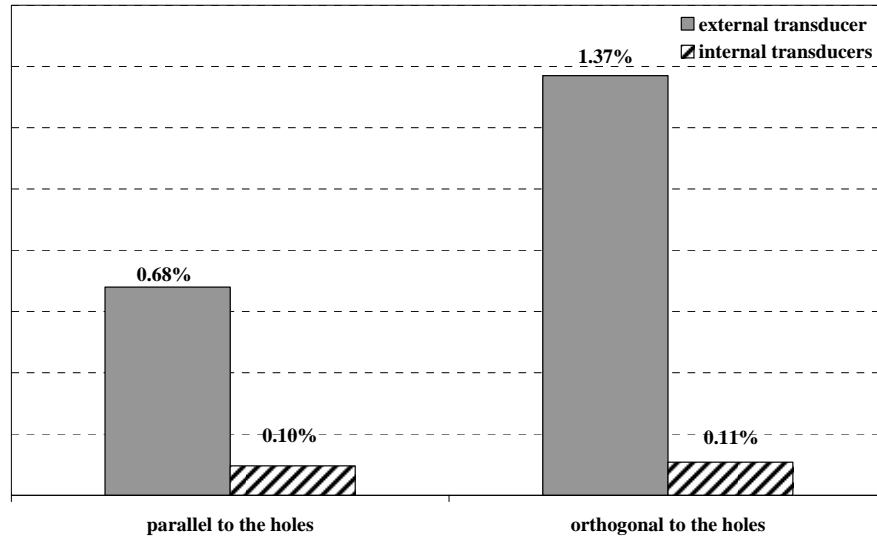


Figure 2.75: comparison between maximum strains determined from internal or external transducers [-]

A summary of the characteristics of the walls discussed in this paragraph is provided below:

Compression strength

f_{wv}	7.93	MPa	Vertical direction
f_{wh}	3.09	MPa	Horizontal direction
f_{wo}	1.01	MPa	Diagonal direction

Maximum strains

ε_v	1.2	‰	Vertical direction
ε_h	1.0	‰	Horizontal direction

ε_o	0.8	‰	<i>Diagonal direction</i>
<i>Elastic modulus</i>			
E_v	10167.0	MPa	<i>Vertical direction</i>
E_h	4888.0	MPa	<i>Horizontal direction</i>
E_o	7094.2	MPa	<i>Diagonal direction</i>
G_w	787.5	MPa	<i>Shear modulus</i>
<i>Poisson coefficient</i>			
ν_v	0.40		
<i>Ratio between f and E</i>			
f_{wv}/E_v	0.78	‰	
f_{wh}/E_h	0.63	‰	
f_{wo}/E_o	0.14	‰	

Table 2.17: characterisation of infill wall of half-full and type 1 mortar

2.8 Experimental tests results on walls of half-full bricks and type 2 mortar

Similarly to experiments previously discussed, compression tests have been performed on walls built using type 2 mortar and half-full bricks.

The results achieved highlighted a behaviour that in general is not different from what has been observed on walls built using the same bricks and the stronger type 1 mortar.

Experimental results from tests carried out are shown below, the following figures have been obtained from measurements of external transducer.

Tables 2.18, 2.19 and 2.20 illustrate results achieved in terms of maximum load F , strength f_w and elastic modulus E .

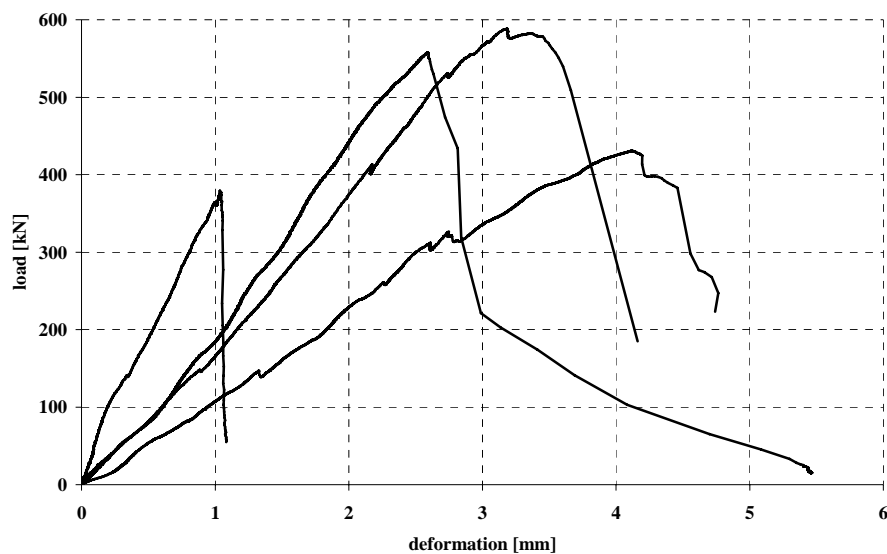


Figure 2.76: compression tests parallel to holes, load-displacement curves of walls of half-full bricks and type 2 mortar

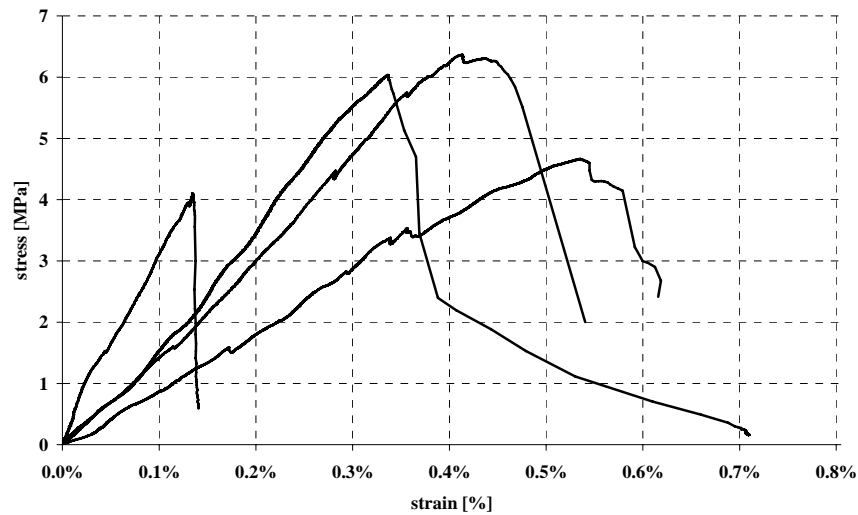


Figure 2.77: compression tests parallel to holes, stress-strain curves of walls of half-full bricks and type 2 mortar

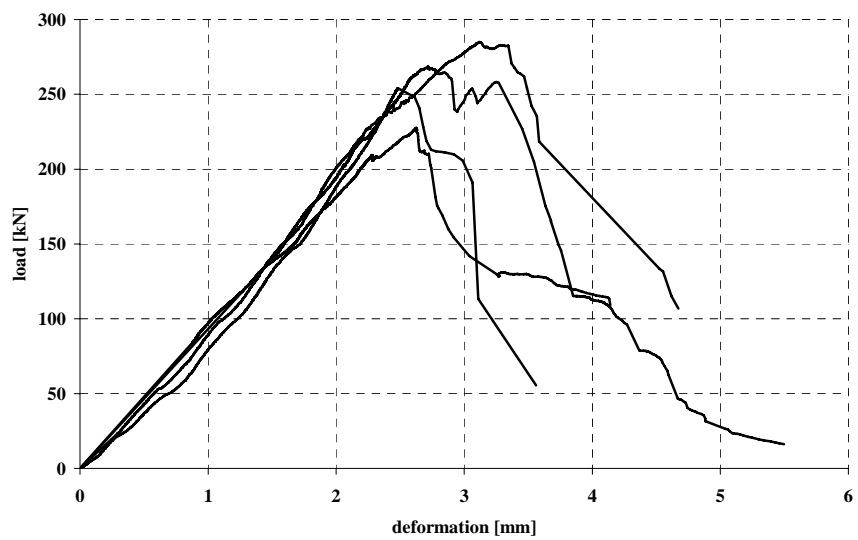


Figure 2.78: compression tests orthogonal to holes, load-displacement curves of walls of half-full bricks and type 2 mortar

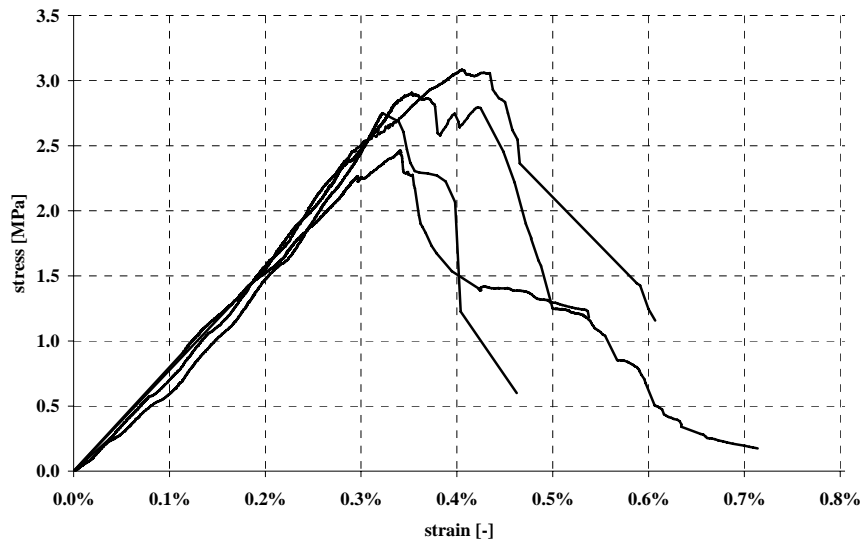


Figure 2.79: compression tests orthogonal to holes, stress-strain curves of walls of half-full bricks and type 2

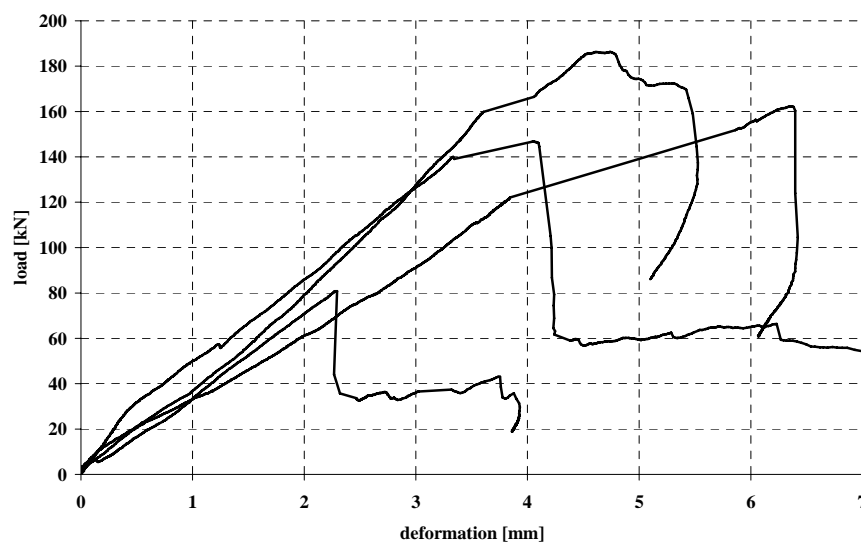


Figure 2.80: diagonal compression tests, load-displacement curves of walls of half-full bricks and type 2

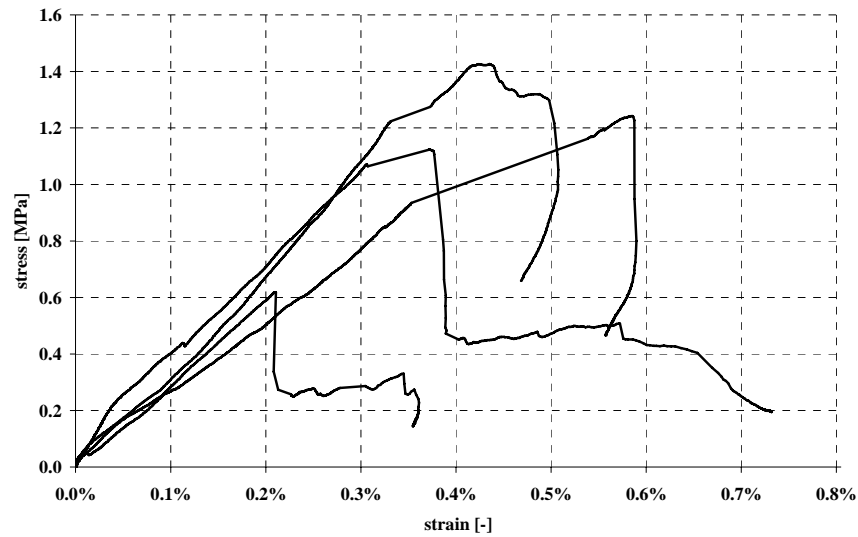


Figure 2.80: diagonal compression tests, stress-strain curves of walls of half-full bricks and type 2 mortar

<i>Specimen</i>	<i>l[mm]</i>	<i>t[mm]</i>	<i>F[kN]</i>	<i>f_{wv}[Mpa]</i>	<i>ε_y</i>	<i>E_v[MPa]</i>
Specimen 1	770	120	431,02	4,66	0,53%	749,20
Specimen 2	770	120	557,46	6,03	0,33%	1900,72
Specimen 3	770	120	588,38	6,36	0,41%	1875,01
Specimen 4	770	120	379,32	4,10	0,26%	1387,97
<i>f_{wv}</i>	5,29	<i>MPa</i>	<i>Average compression strength</i>			
<i>E_v</i>	1478,23	<i>MPa</i>	<i>Average elastic modulus</i>			
<i>S</i>	1,08	<i>Standard deviation</i>				

Table 2.18: results from compression parallel to holes on walls of half-full bricks and type 2 mortar

<i>Specimen</i>	<i>l[mm]</i>	<i>t[mm]</i>	<i>F[kN]</i>	<i>f_{wh}[Mpa]</i>	<i>e_h</i>	<i>E_h[MPa]</i>
Specimen 1	770	120	186,23	2,01	0,166%	749,20
Specimen 2	770	120	268,58	2,90	0,353%	1900,72
Specimen 3	770	120	284,95	3,08	0,405%	1875,01
Specimen 4	770	120	254,13	2,75	0,322%	1387,97
<i>f_{wh}</i>	2,67	<i>MPa</i>	<i>Average compression strength</i>			
<i>E_h</i>	900,70	<i>MPa</i>	<i>Average elastic modulus</i>			
<i>S</i>	0,46	<i>Standard deviation</i>				

Table 2.19: results from compression orthogonal to holes on walls of half-full bricks and type 2 mortar

<i>Specimen</i>	<i>l[mm]</i>	<i>t[mm]</i>	<i>F[kN]</i>	<i>f_{wo}[Mpa]</i>	<i>e_o</i>	<i>E_o[MPa]</i>
Specimen 1	1088,78	120	162,28	1,24	0,58%	1088,78
Specimen 2	1088,78	120	186,28	1,42	0,42%	1088,78
Specimen 3	1088,78	120	146,89	1,12	0,37%	1088,78
Specimen 4	1088,78	120	80,78	0,61	0,21%	1088,78
<i>f_{wo}</i>	1,10	<i>MPa</i>	<i>Average compression strength</i>			
<i>E_o</i>	301,53	<i>MPa</i>	<i>Average elastic modulus</i>			
<i>S</i>	0,34	<i>Standard deviation</i>				

Table 2.20: results from diagonal compression on walls of half-full bricks and type 2 mortar

Experimental tests results achieved from internal transducers are shown below:

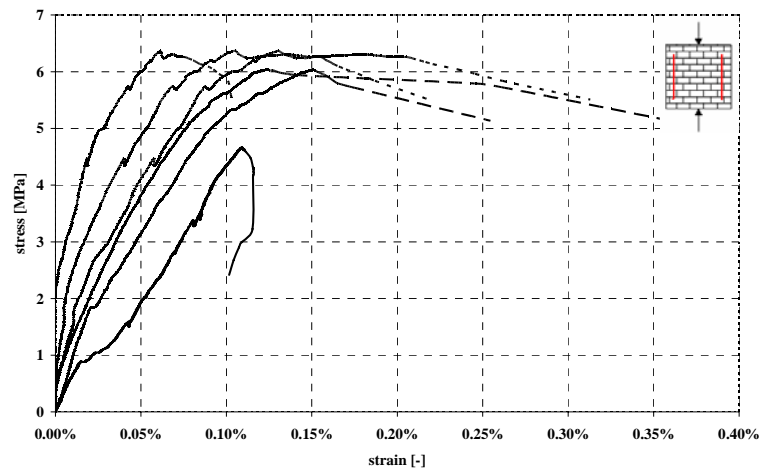


Figure 2.82: stress–strain curves (internal transducer) from compression tests parallel to holes

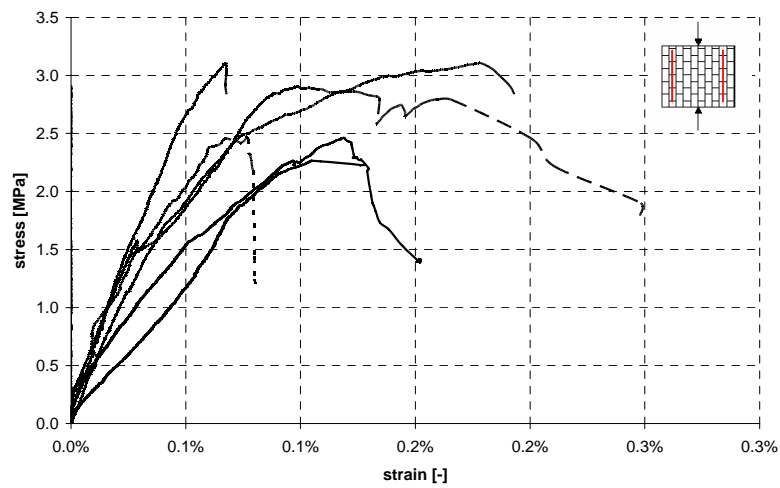


Figure 2.83: stress–strain curves (internal transducer) from compression tests orthogonal to holes

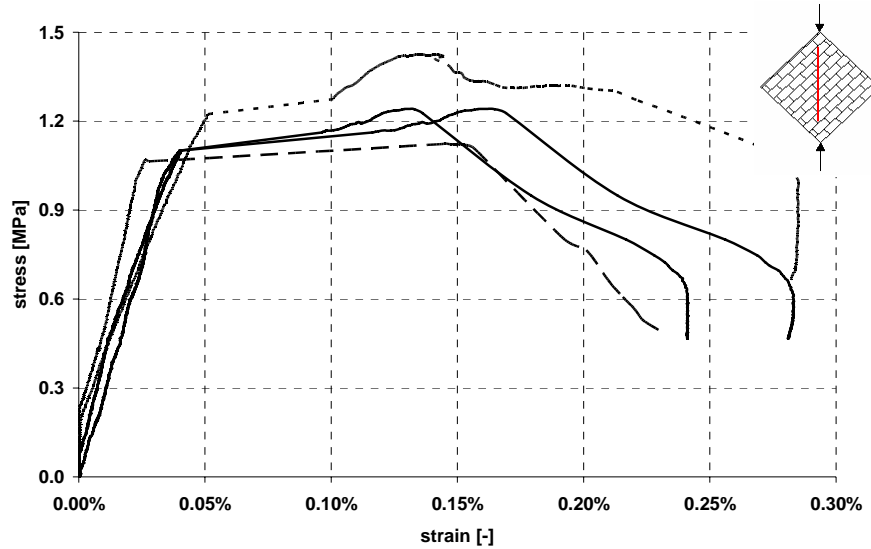


Figure 2.83 stress–strain curves (internal transducer) from diagonal compression tests

From figures, considerably higher initial stiffness can be observed compared with what has been determined referring to the external transducer. Also in this case the difference between elastic modules calculated with the two methods (internal or external transducers) differs.

<i>Parallel load</i>		<i>Orthogonal load</i>		<i>Diagonal load</i>	
<i>Wall</i>	<i>E_v[MPa]</i>	<i>Wall</i>	<i>E_h[MPa]</i>	<i>Wall</i>	<i>E_d[MPa]</i>
Specimen 1	3425	Specimen 1	2340	Specimen 1	2865
Specimen 2	5757	Specimen 2	5291	Specimen 2	5442
Specimen 3	8699	Specimen 3	4237	Specimen 3	3788
Specimen 4	14511	Specimen 4	3889	Specimen 4	2389
Average	8098	Average	3939	Average	3621

Table 2.21: elastic modulus from internal transducers

<i>Parallel load</i>		<i>Orthogonal load</i>		<i>Diagonal load</i>	
<i>Wall</i>	ε_{vmax}	<i>Wall</i>	ε_{hmax}	<i>Wall</i>	ε_{dmax}
Specimen 1	0,00072	Specimen 1	0,00055	Specimen 1	0,00148
Specimen 2	0,00093	Specimen 2	0,00067	Specimen 2	0,00105
Specimen 3	0,00067	Specimen 3	0,00038	Specimen 3	0,00154
Specimen 4	0,00011	Specimen 4	0,00030	Specimen 4	0,00041
Average	0,00060	Average	0,00047	Average	0,00112

Table 2.22: strains from internal transducers

<i>Wall</i>	$f_{wd}[MPa]$	$\delta_{vert}[mm]$	$\delta_{oriz}[mm]$	ε_v	ε_h	γ	$G_w[MPa]$
Specimen 1	1,242	1,086	0,052	0,0014	0,00007	0,0007	1762,16
Specimen 2	1,426	0,774	0,015	0,0010	0,00002	0,0005	2762,47
Specimen 3	1,124	1,130	0,089	0,0015	0,00012	0,0007	1587,63
Specimen 4	0,618	0,300	0,054	0,0004	0,00007	0,0001	3696,53
Average	1,103	0,823	0,052	0,0011	0,00007	0,0005	2452,20

Table 2.23: summary of data for diagonal compression

It is interesting to perform in the following Table 2.24 a comparison of results achieved using the two methods previously described

<i>Load</i>	<i>E[MPa]</i>		<i>e_{max}</i>		<i>F[kN]</i>	<i>f_k[MPa]</i>
	<i>External</i>	<i>Internal</i>	<i>External</i>	<i>Internal</i>	-	-
parallel	1478,23	8097,80	0,00388	0,00060	489,04	5,29
orthogonal	900,70	3939,40	0,00312	0,00047	248,47	2,68
diagonal	301,52	3620,85	0,00460	0,00112	144,06	1,10

Table 2.24: summary of data from external and internal transducers

The following Table 2.25 summarises the parameters determined: values listed have been used in the following steps of numerical analysis discussed in this thesis. The experimental tests described in chapter 7 have been performed on portal infilled with the masonry described in this paragraph.

Compression strength

f_{wv}	5.293	MPa	Vertical direction
f_{wh}	2.669	MPa	Horizontal direction
f_{wo}	1.103	MPa	Diagonal direction

Maximum strains

ε_v	0.605	‰	Vertical direction
ε_h	0.473	‰	Horizontal direction
ε_o	1.120	‰	Diagonal direction

Elastic modulus

E_v	8097.80	MPa	Vertical direction
E_h	3939.40	MPa	Horizontal direction
E_o	3620.85	MPa	Diagonal direction
G_w	2452.20	MPa	Shear modulus

Poisson coefficient

ν_v	0.140
---------	-------

Ratio between f and E

f_{wv} / E_v	0.654	‰
f_{wh} / E_h	0.677	‰
f_{wo} / E_o	0.305	‰

Table 2.25: characterisation of infill wall of half-full bricks and type 2 mortar

2.9 Influence of mortar on experimental results

At the end of the experimental activities performed, it is possible to assess the influence that the mortar adopted has on the behaviour of walls realized with the same bricks that, in this specific case, have been named *half-full*.

	f_m [MPa]	E_m [MPa]	ν
Type 1 mortar	23,49	22571,12	0,19
Type 2 mortar	11,72	16228,43	0,21

Table 2.26: characteristics of type 1 and type 2 mortar

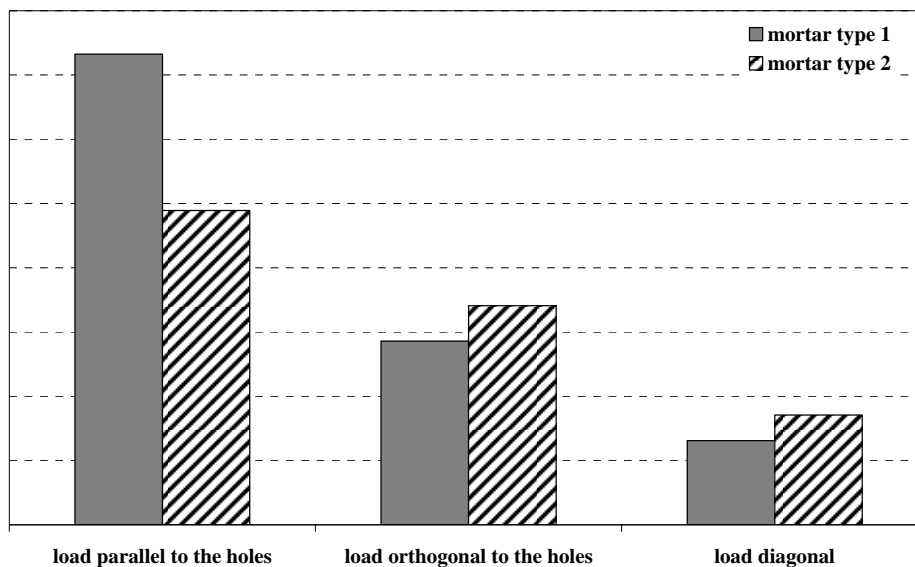


Figure 2.84: comparison between maximum loads of walls with different mortar

By analysing Figure 2.84 it is possible to state that mortar has an important effect on wall's strength in a direction parallel to holes with an increase, for walls made with type 1 mortar, of approximately 50%.

With regards to orthogonal to holes compression tests the measurements recordered indicate much more limited variations; unlike what may be expected walls built with type 2 mortar are stronger of approximately 25% compared to the others built with type 1 mortar. This result can be associated to the higher fluidity of type 2 mortar that, even though it is less resistant, falls in greater quantity within bricks' holes. This holes filling effect has been already pointed out when analyzing orthogonal holes compression tests that improve walls' strength much more than what the sole mortar strength can do.

2.10 Correlation between materials and walls' strength

The following tables illustrate a comparison between infill panels' strength determined with experimental tests with the ones calculated, starting from the experimental strength of mortar and bricks, referring to some well known formulas from scientific literatures and from indications of the Italian *Technical Code* (ITC) and *Eurocode 6* (EC6).

Previously in *Biondi & al. (2000, 2001, 2002)* such reports have been discussed in detail and it has been proved how the *Italian Technical Code*, *Eurocode 6* and *Tassios 2* provide, for elements of medium strength, the very best results. It is important to point out that the values analytically determined from the *ITC* and *EC6* are characteristic strengths and therefore, to be compared with experimental results, they have been converted into average values by dividing them for a factor equal to the ratio between characteristic and experimental strength:

$$f_{wk} = \min \left\{ \frac{f_{wm}}{1,20}, \frac{\min \{f_{wm}\}}{0,90} \right\} \quad Eq. 2.8$$

Eq. 2.3 is a valid formula, as in the current case in question for a limited number of samples, in which:

f_{wi} are the single values of experimental strength

f_{wm} average strength

From the results achieved, presented in the following figures and tables, it has been demonstrated that *Tassios 2* (1998) formula is the most accurate for all the walls considered. The other formulas that, differently from the previous one do not correlate strength and panel's slenderness, provide over estimated or under estimated results.

Reference	
<i>ITC</i> (1987)	f_{wk} Table 2.A from Italian Code (D.M 20.11.1987)
<i>EC6</i>	$f_{wk} = k(\delta f_b)^\alpha f_m^\beta$
<i>Tassios 1</i> (1998)	$f_w = 2/3 f_b + 0,1 f_m$
<i>Tassios 2</i> (1998)	$f_w = f_b (4 + 0,1 f_m) / (12 + 5 h_w / t_w) + 2$
<i>Tassios 3</i> (1998)	$f_w = 0,7 \sqrt{f_b} \sqrt[3]{f_m}$
<i>Guidi</i> (-)	$f_w = 0,1 f_b \log(f_m + 2)$
<i>Cuomo</i> (1997)	$f_w = 0,4 f_b^{0,7} f_m^{0,435}$

Table 2.27: formula adopted to determine walls' strength

	f_{wv} parallel [MPa]	f_{wh} orthogonal [MPa]
<i>Experimental</i>	3,11 (2,59)	1,90 (0,97)
<i>ITC.</i>	3,56 (4,96)	1,40 (1,95)
<i>EC6</i>	6,86 (6,60)	3,42 (3,29)
<i>Tassios 1</i>	9,28	5,66
<i>Tassios 2</i>	2,88	2,42
<i>Tassios 3</i>	6,47	4,47
<i>Guidi</i>	1,46	0,70
<i>Cuomo</i>	8,14	4,85

Table 2.28: average strength of walls of hollow bricks and type 1 mortar
(the characteristic values are expressed in brackets)

	f_{vv} parallel [MPa]	f_{vh} orthogonal [MPa]
<i>Experimental</i>	7,93 (6,63)	3,10 (2,56)
<i>ITC</i>	15,11 (14,99)	1,98 (1,96)
<i>EC6</i>	12,03 (10,83)	3,99 (3,59)
<i>Tassios 1</i>	17,94	5,75
<i>Tassios 2</i>	5,37	2,74
<i>Tassios 3</i>	9,70	4,53
<i>Guidi</i>	3,29	0,72
<i>Cuomo</i>	14,35	4,94

Table 2.29: average strength of walls of half-full bricks and type 1 mortar (the characteristic values are expressed in brackets)

	f_{vv} parallel [MPa]	f_{vh} orthogonal [MPa]
<i>Experimental</i>	5.29	2.69
<i>ITC</i>	5.78 (4.80)	3.25 (2.70)
<i>EC6</i>	7.65 (6.35)	3.38 (2.81)
<i>Tassios 1</i>	16.77	4.58
<i>Tassios 2</i>	3.61	2.35
<i>Tassios 3</i>	7.69	3.59
<i>Guidi</i>	2.66	0.58
<i>Cuomo</i>	10.60	3.65

Table 2.30: average strength of walls of half-full bricks made from type 1 mortar (the characteristic values are expressed in brackets)

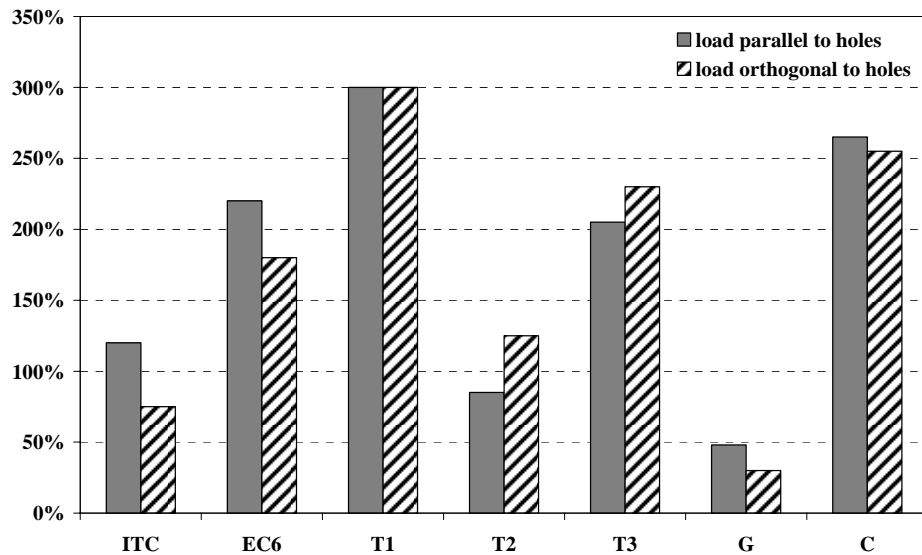


Figure 2.85: comparison between theoretical and experimental strength walls of hollow bricks and type 1 mortar

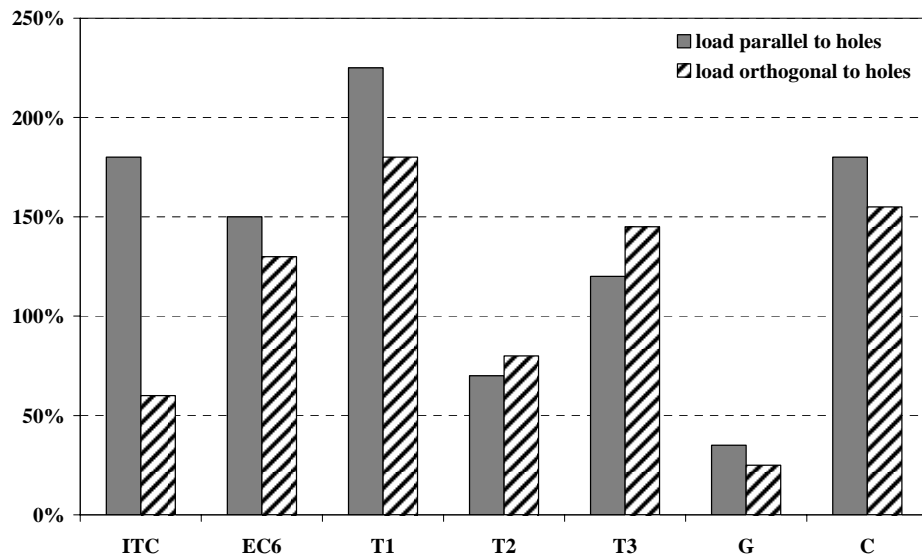


Figure 2.86: comparison between theoretical and experimental strength of walls of half-full bricks and type 1 mortar

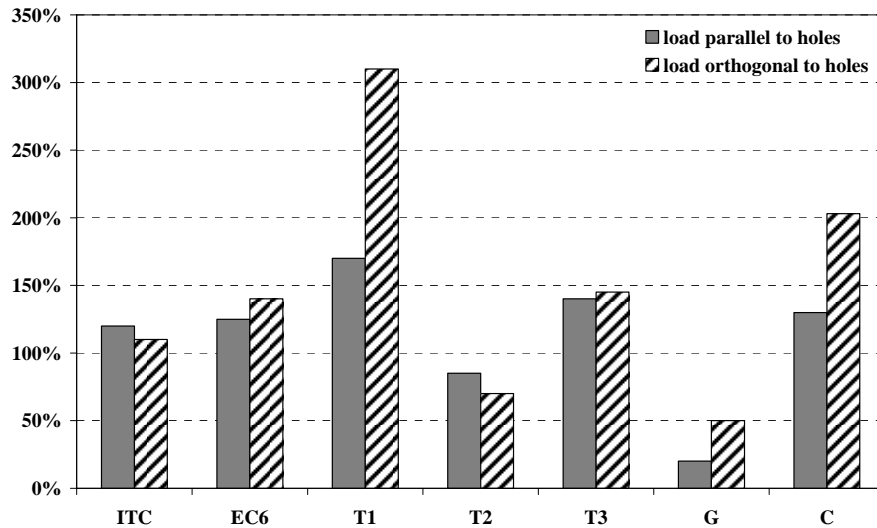


Figure 2.87: comparison between theoretical and experimental strength of walls of half-full bricks and type 2 mortar

However, with regards to Codes formulas, the *Italian Code* provides, for walls built using type 2 mortar and hollow ones, as well as half-full bricks, results that are more in agreement with experimental ones, *Eurocode 6* however is much more reliable, even if with a non negligible over estimation, in the case of half-full bricks and type 1 mortar panels. This observation confirms what has been discussed in other studies referring to the same panels typology [Biondi & al. 2001]; it is also important to see how both formulas from *ITC* and *EC6* appear to be much more suitable to walls built using mortars of medium to low strength as in the case of type 2 mortar. From a comparison between Figures 2.85, 2.86 and 2.87 it can be observed that, in the case of hollow brick panels, theoretical formulas provide strength levels that, both for parallel and orthogonal to holes compression, are affected from the same over estimation or under estimation error; in the case of half-full brick panels this does not occur. An explanation of what has been observed comes from what has been determined from compression tests on bricks, in fact while the strength of perforated bricks doesn't differ considerably for the two loading directions, for half-full bricks very different values have been determined. Figure 2.88 compares walls' strength for parallel and

orthogonal to holes compression of both typologies of panels built using type 1 mortar, expressed as a percentage of strength of bricks with which they are made. As it can be seen, the walls' strength in each case is lower than the hollow or half-full brick strength. In the case of hollow brick panels for both of the loading directions, percentage values of achievement of bricks maximum strength have been determined that are not so different, in fact bricks have similar strengths for the two loading directions. Less exploitation of perforated bricks' strength (parallel to holes compressed) justifies their position within the panel, as they are loaded along their maximum slender direction they provide a higher level of fragility to the wall. However in the case of half-full bricks and type 1 mortar panels the difference between the loading directions is much clearer as the difference between bricks strength resistance orthogonal and parallel to holes is much clearer. Once again, in the orthogonal to holes direction walls' strength is closer to maximum strength of bricks; it is important to point out how achieving 38% of brick's resistance parallel to holes results in a walls resistance of approximately 50% higher than what occurs achieving 60% of orthogonal bricks strength.

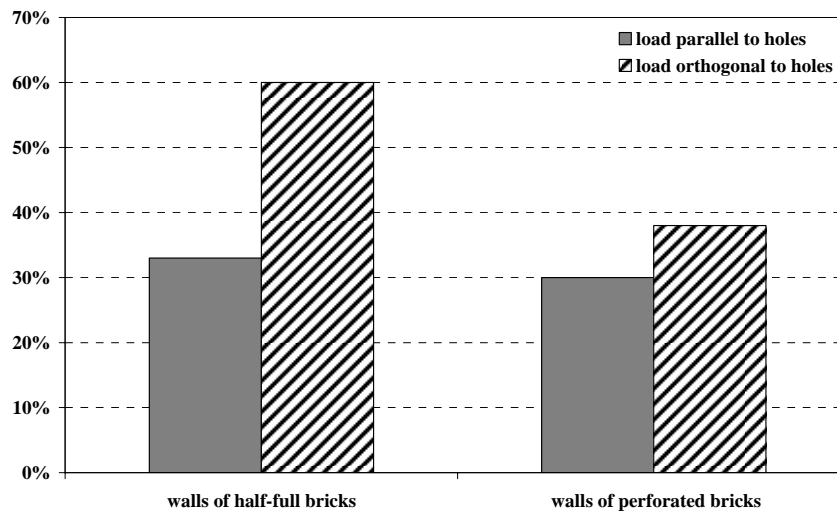


Figure 2.88: comparison between experimental strength of walls as a percentage of bricks strength

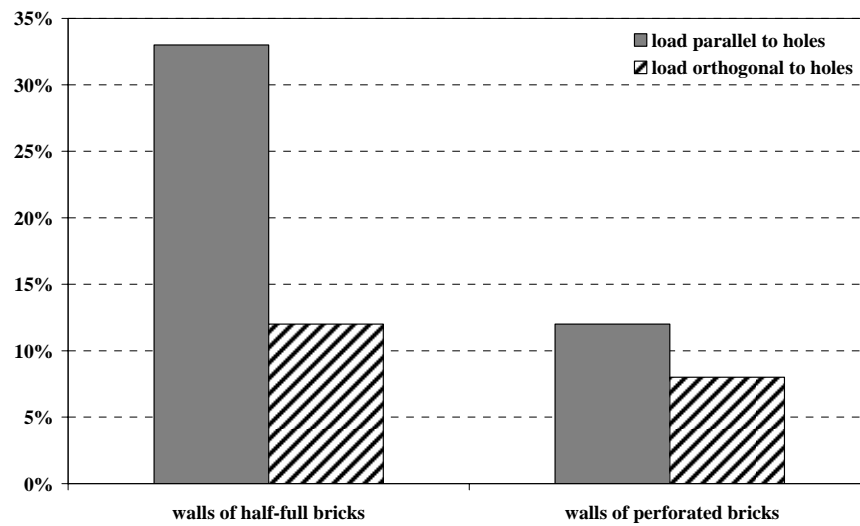


Figure 2.89: comparison between experimental strength of walls as a percentage of type 1 mortar strength

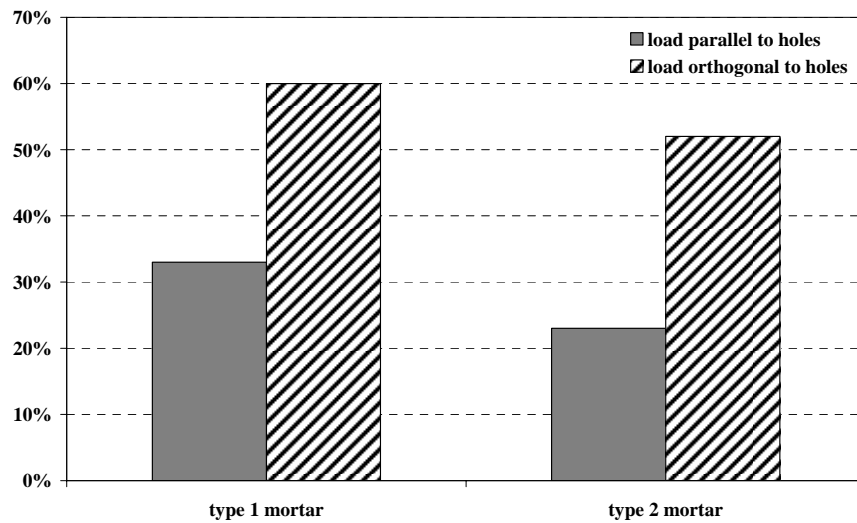


Figure 2.90: comparison between experimental strength of half-full bricks walls as a percentage of bricks strength

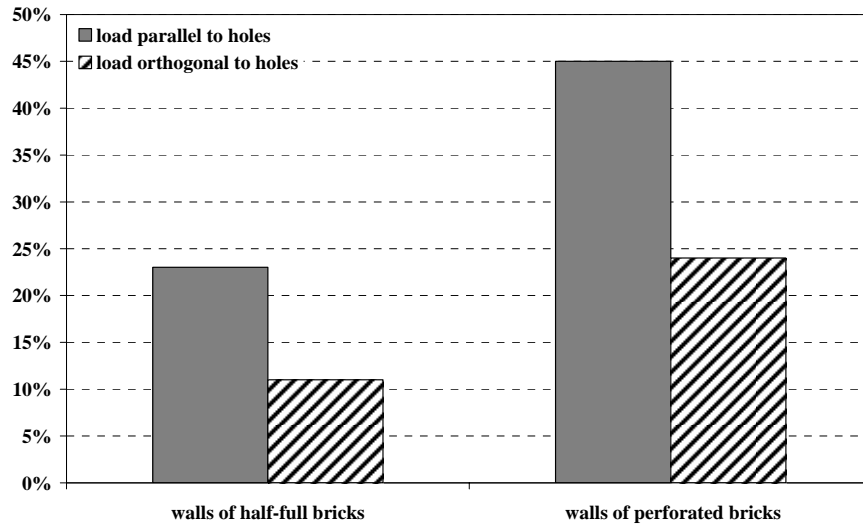


Figure 2.91: comparison between experimental strength of walls as a percentage of mortar's strength

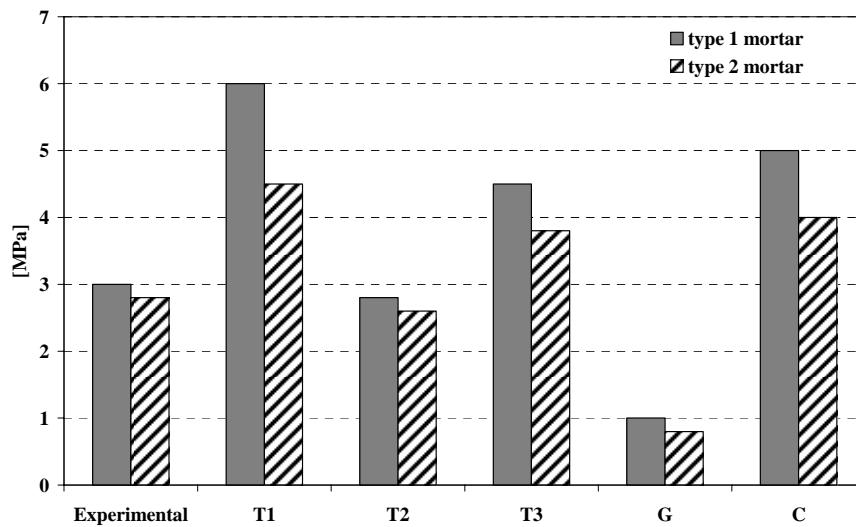


Figure 2.92: comparison between experimental and theoretical orthogonal to holes strength, of walls built using half-full bricks with type 1 and type 2 mortar

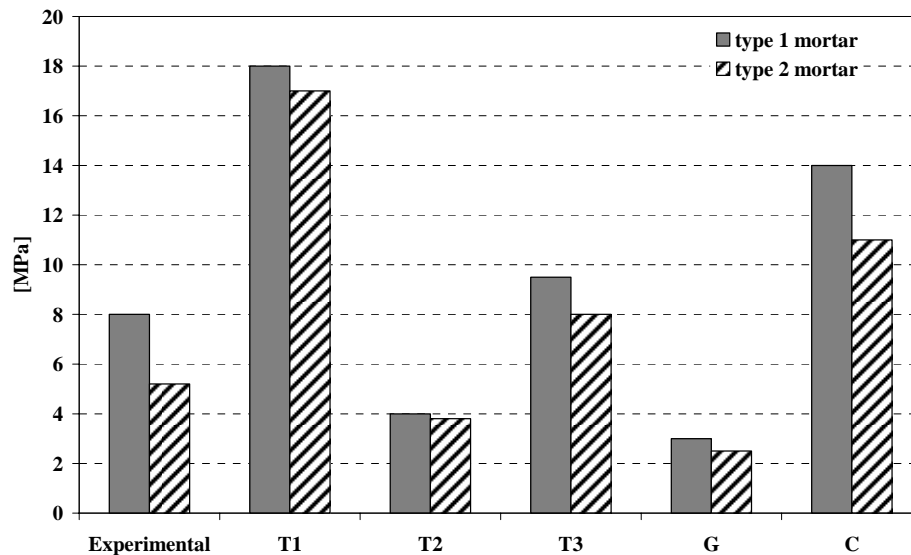


Figure 2.93: comparison between experimental and theoretical parallel to holes strength of walls built using half-full bricks with type 1 and type 2 mortar

In a similar way to previous indications, Figure 2.89 compares resistances parallel and orthogonal to holes for all the panels, expressed as a percentage of mortar's strength. It is still in the stronger direction, therefore parallel to holes of half-full bricks, that the highest percentage is achieved; however the value determined is lower than 35%. In the remaining cases, it does not deviate much from 10% and therefore using such high resistant mortar seems superfluous.

Furthermore we must point out how, for all the panels, despite that mortar's strength exceeds hollow bricks strength, an ideal exploitation of weaker material's strength, in this case are hollow and half-full bricks, is never reached. Figures 2.90 and 2.91 compare results, expressed as a percentage of strength of bricks and mortar, achieved for half-full brick walls built using the two different mortars adopted.

Figures 2.92 and 2.93 compare experimental and theoretical data for walls of half-full bricks. We must point out how *Tassios 2* formula does not substantially feel the effects of mortar's strength variation, the other formulas confirm, regardless of the type of mortar, their inclination to

over estimating or under estimating resistance of half-full brick walls for both loading directions.

2.11 Experimental tests results of double panel walls

Double panel walls have been realized, coupling one panel of hollow bricks and one of half-full bricks both realized with type 1 mortar, the panels have opposite holes direction. For the tests indicated herein, the direction corresponding to holes of half-full bricks is considered as the direction of vertical loading. Differently from single panels, an important residual resistance is found. This phenomenon is rather clear for walls vertically loaded in which, due to different strength offered by the panels (the wall of hollow bricks loaded orthogonally to holes resists approximately 80% less than a half-full brick wall parallel to holes loaded), half-full bricks remain substantially integral even after hollow brick panels collapse; the residual resistance coincides therefore with the capacity of the half-full brick panel slightly damaged.

The phenomenon previously described can be neglected when the load is horizontally applied: in this case the resistance offered by the panels is similar and the rupture involves both of the walls that, at the end of the test, don't offer a relevant residual resistance.

From the considerations previously made, we can understand why horizontal compression tests, therefore along the weakest direction of the strongest panel, provide the greatest resistance. Horizontal strength is more than 30% of vertical strength, deformation to collapse is however similar for both of the cases examined. Diagonal compression tests, as previously observed for single panel walls, have developed much lower resistance than the others previously described: from experimental observation the wall resists with a compressed strut mechanism, the strut has more or less the same dimensions on both of the panels even though it is the panel of hollow bricks that causes the collapse. The compressive strength registered for all loading directions is lower than what has been determined for walls built using half-full bricks and type 1 mortar and is slightly higher than hollow brick walls' strength.



Figure 2.94: compression test parallel to holes, initial phase and collapse



Figure 2.95: compression test orthogonal to the holes: initial phase and collapse



Figure 2.96: diagonal compression test, front and side view of collapse

The following figures illustrate *load–displacement* and *stress–strain* curves of double panel walls for the three loading directions; displacements and correspondent strains have been calculated from external transducer.

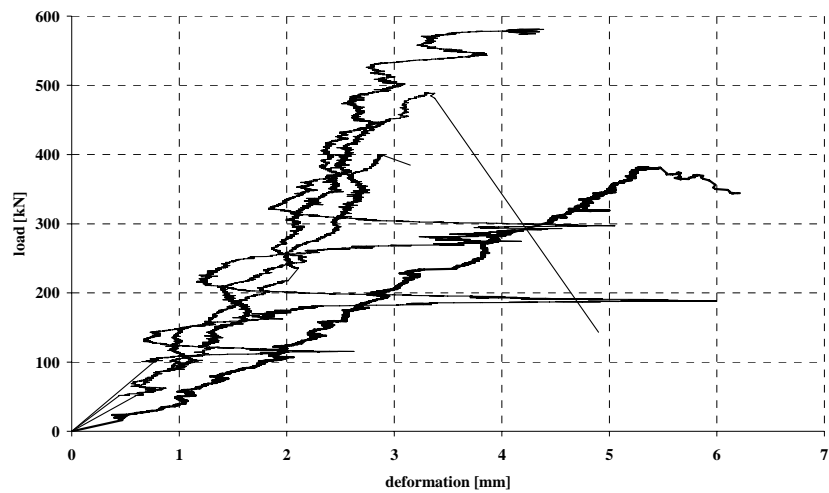


Figure 2.97: *load–displacement curves from parallel to holes compression tests of double panel walls*

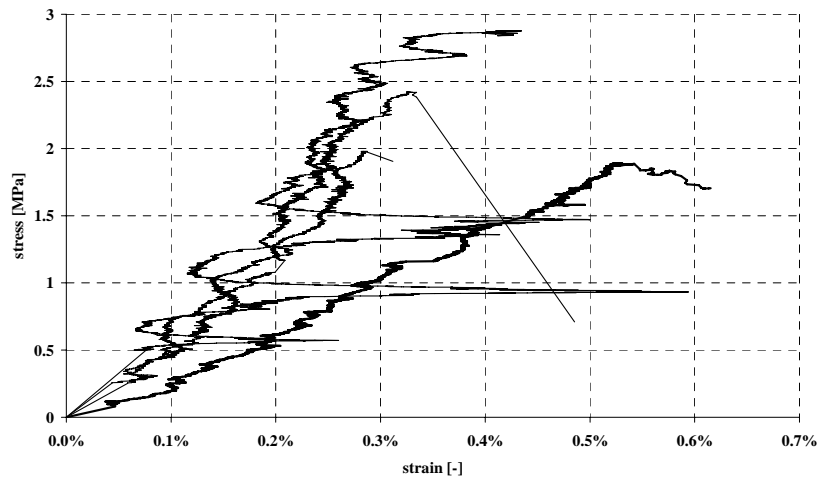


Figure 2.98: *stress–strain curves from parallel to holes compression tests of double panel walls*

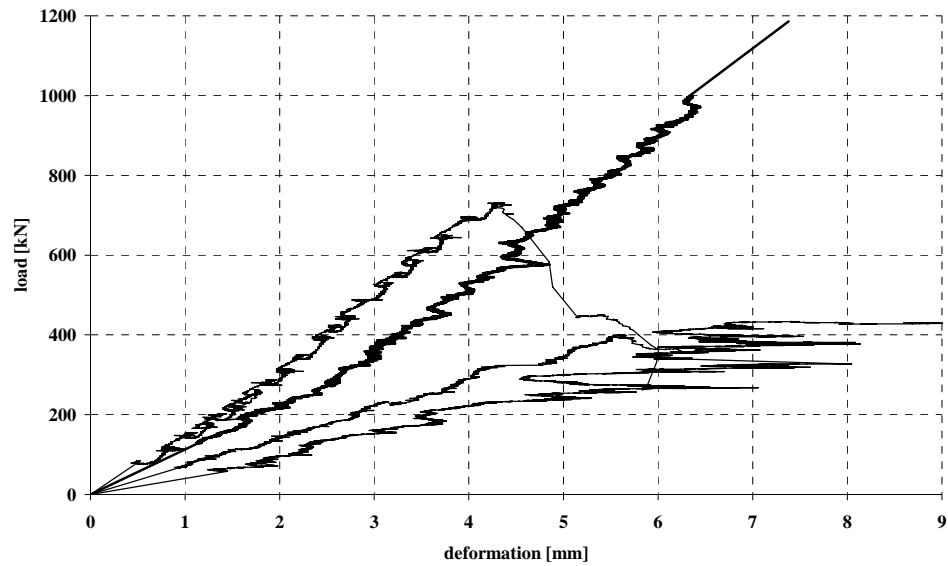


Figure 2.99: load–displacement curves from orthogonal to holes compression tests of double panel walls

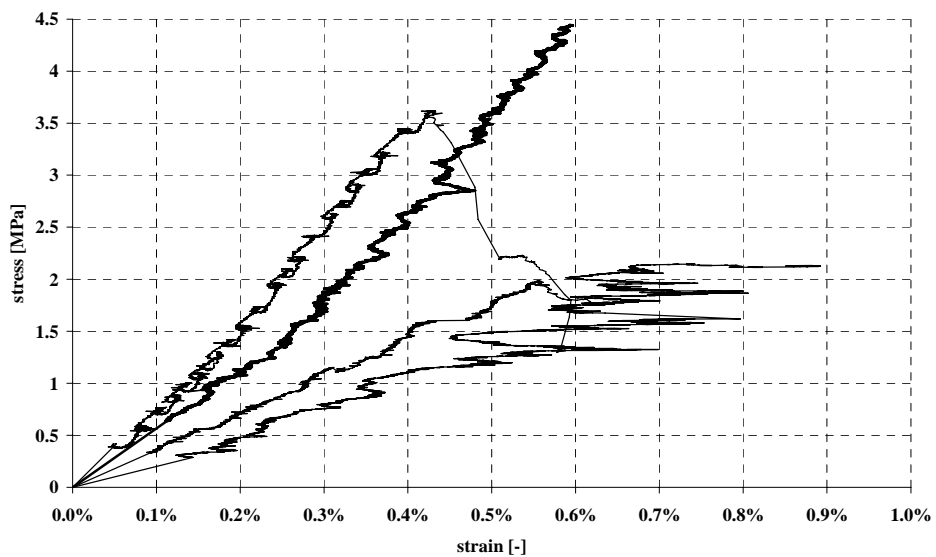


Figure 2.100: stress–strain curves from orthogonal to holes compression tests of double panel walls

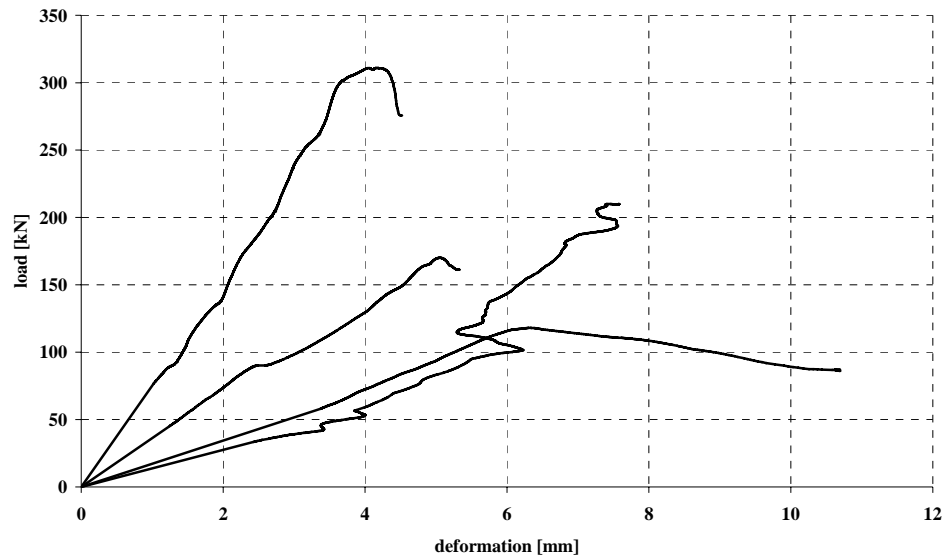


Figure 2.101: load–displacement curves from diagonal compression tests of double panel walls

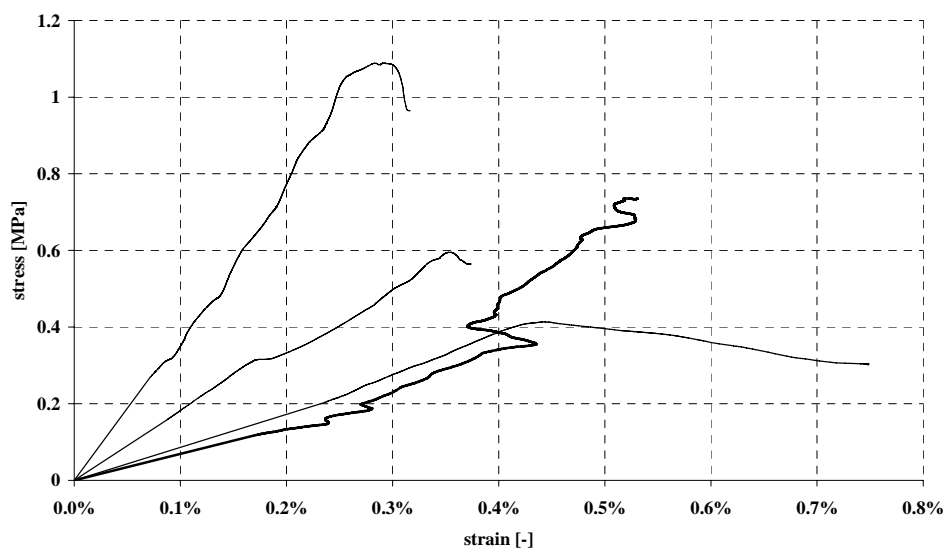


Figure 2.102: stress–strain curves from diagonal compression tests of double panel walls

The following Table 2.31 summarises some of the mechanical parameters achieved from tests previously described for double panel walls (the elastic modulus have been calculated from the external transducer).

<i>parallel loading</i>			
Wall	F [kN]	f_{kv} [MPa]	E_v [MPa]
Sample 1	381.80	1.89	361.21
Sample 2	488.97	2.42	744.86
Sample 3	399.69	1.98	688.57
Sample 4	581.11	2.88	667.98
average	462.9	2.29	615.7

<i>orthogonal loading</i>			
Wall	F [kN]	f_{kh} [MPa]	E_h [MPa]
Sample 1	1185.90	5.87	803.46
Sample 2	433.66	2.15	289.30
Sample 3	730.68	3.62	850.08
Sample 4	399.98	1.98	356.45
average	687.6	3.40	574.8

<i>diagonal loading</i>			
Wall	F [kN]	f_{v0} [MPa]	f_{vk0} [MPa]
Sample 1	211.38	0.75	0.52
Sample 2	124.49	0.44	0.31
Sample 3	316.67	1.12	0.78
Sample 4	177.27	0.63	0.44
average	207.5	0.73	0.51

Table 2.31: results of compression tests on double panel walls

3. Experimental tests on portal's materials

3.1 Introduction

For an in-depth knowledge of mechanical characteristics of prototype portal (described in chapter 4) as included in the experimental activities and in the numerical modelling discussed in the following chapters, experimental tests have been carried out in order to define mechanical characteristics of materials with which they have been made.

The materials used to build the portals are:

- steel FeB 44 k in bars of 6 mm diameter (stirrups of beams and columns);
- steel FeB 44 K in bars of 8 mm diameter (longitudinal rebars of columns);
- steel FeB 44 K in bars of 10 mm diameter (longitudinal rebars of beams);
- concrete R_{ck} 30 for the entire structure.

3.2 Experimental tests on reinforcing bars

Through monotone tensile tests on rebars samples, the mechanical characteristics have been determined; all the tests have been performed at the *Laboratory of experiments on materials and structures* of the University of Roma Tre.

The bars available for the tests were the followings:

- 2 samples of 6 mm diameter;
- 3 samples of 8 mm diameter;
- 4 samples of 10 mm diameter.

Bars have been weighed, measured and therefore the equivalent diameter (d_{eq}) has been established; values acquired are shown in the following tables.

In order to establish d_{eq} the following formula has been used:

$$P_i = \mu \cdot l_i \cdot \frac{\pi \cdot d_{eq}^2}{4} \quad Eq. 3.1$$

with:

$$\mu = 7850 \frac{\text{kg}}{\text{cm}^3} \quad \text{specific weight of steel}$$

$$P_i \quad \text{sample's weight}$$

$$l_i \quad \text{sample's length}$$

6 mm diameter	weight [g]	length [mm]	ϕ_{eq} [mm]
Sample 1	237	998	6,2
Sample 2	238	998	6,2

8 mm diameter	weight [g]	length [mm]	ϕ_{eq} [mm]
Sample 1	400	999	8,06
Sample 2	401	999	8,07
Sample 3	398	998	8,04

10 mm diameter	weight [g]	length [mm]	ϕ_{eq} [mm]
Sample 1	611	997	9,96
Sample 2	614	998	9,98
Sample 3	612	999	9,97
Sample 4	617	1000	10

Table 3.1: weight, length and equivalent diameter of samples

Each bar has been fixed to the MTS press with vices designed for this kind of experimental test. By pulling the bar stresses are transferred from vices to bar by means of the transfer stress length l_{tr} , in the specific case an $l_{tr} = 4 \text{ cm}$ has been adopted (l_{tr} is the length of the bar's portion that is connected to traction vices).

The parameters used to characterise bar's steel are:

E	<i>elastic modulus;</i>
ε_y	<i>yelding strain;</i>
σ_y	<i>yelding stress;</i>
ε_h	<i>strain in correspondence with hardening;</i>
σ_h	<i>stress in correspondence with hardening;</i>
E_h	<i>hardening modulus;</i>
ε_u	<i>strain in correspondence with breakage;</i>
σ_u	<i>stress in correspondence with breakage.</i>

The following tables indicate the parameters previously described for each one of the bars tested.

6 mm diameter	E [MPa]	ε_y [-]	σ_y [MPa]	ϕ_{eq} [mm]
Sample 1	224366,2	0,37	608,67	6,2
Sample 2	218818,4	0,25	391,3	6,2
Average	221592,3	0,31	500,5	6,2

8 mm diameter	E [MPa]	ε_y [-]	σ_y [MPa]	ϕ_{eq} [mm]
Sample 1	219298,2	0,28	536,59	8,06
Sample 2	212314,2	0,256	420,4	8,07
Sample 3	213675,2	0,24	385,16	8,04
Average	215095.87	0.26	447.38	8.06

10 mm diameter	E [MPa]	ε_y [-]	σ_y [MPa]	ϕ_{eq} [mm]
Sample 1	213219,6	0,26	507,63	9,96
Sample 2	208768,3	0,149	459,5	9,98
Sample 3	214132,8	0,25	488,93	9,97
Average	212040.23	0.22	485.35	9.97

Table 3.2: mechanical parameters from traction tests (part A)

6 mm diameter E_h [MPa] ε_h [%] σ_h [MPa]

Sample 1	755,65	3,2	624,07
Sample 2	836,60	3,2	417,05
Average	796,13	3,20	520,56

8 mm diameter E_h [MPa] ε_h [%] σ_h [MPa]

Sample 1	1122,60	2,97	580,04
Sample 2	986,01	2,86	462,5
Sample 3	980,78	3,00	447,19
Average	1029,80	2,94	496,58

10 mm diameter E_h [MPa] ε_h [%] σ_h [MPa]

Sample 1	1096,21	2,8	533
Sample 2	1019,6	2,8	472,2
Sample 3	1081,09	2,75	537,15
Average	1065,63	2,78	514,12

Table 3.3: mechanical parameters from traction tests (part B)

6 mm diameter ε_u [%] σ_u [MPa] σ_{\max} [MPa]

Sample 1	8,86	666,84	671
Sample 2	7,55	456,97	460
Average	8,21	561,91	565,50

<i>8 mm diameter</i>	ε_u [%]	σ_u [MPa]	σ_{\max} [MPa]
Sample 1	7,35	629,21	639
Sample 2	8,94	522,45	528
Sample 3	7,32	489,56	502
Average	8,13	506,01	515,00

<i>10 mm diameter</i>	ε_u [%]	σ_u [MPa]	σ_{\max} [MPa]
Sample 1	9,4	605,35	616
Sample 2	8,36	528,9	537
Sample 3	6,4	576,6	585
Average	7,38	552,75	561,00

Table 3.4: mechanical parameter from traction tests (part C)

3.3 Experimental tests on concrete

With the same objectives previously described, non-destructive experimental tests have been performed on portal's concrete and destructive tests have been performed on cylindrical samples extracted during the casting phases.

The non-destructive tests performed are: sclerometric and ultrasonic tests. Results from non-destructive tests provide an indication of homogeneity of mass. By correlating the results from one or more tests, it was possible to estimate the compressive strength of portal's concrete.

The sclerometric test includes an assessment of concrete quality using the correlation formula that exists between stiffness and strength to compression.

The method is based on the rebound of a mass striking a piston hitting on concrete surface; the higher the strength, the greater the rebound.

Sclerometric index is strictly related to the surface layer's properties of the sample examined, on which the impact is applied. The rebound generated is definitely influenced by concrete compressive strength, the value may be lower if the material is impregnated with humidity and vice

versa if the superficial layer has undergone an important carbonation process.

The sclerometric index does not feel the effects of the deeper layers' properties of examined material and it may be used to assess the evenness of concrete on site, in order to outline areas of a poor quality or deteriorated concrete in structures; the test method is not an alternative to define compressive strength of concrete (*EN 12390-3*) but, using a suitable corformula, it may provide an estimate of on-site strength.

The objective of the ultrasonic research is to perform a non destructive test for quality control of material, its homogeneity or, in any case, to research any possible faults in the body of the element analysed. The method consists in measuring the speed of diffusion of elastic compression waves duly released into the element. The issuing probe produces ultrasonic impulses with a predefined frequency that are captured by the receiving probe after having crossed the material: the transit time is measured by a quartz timer visualised on a display.

The ratio between transmission point to reception point with regards to length and reception time provides the speed that depends on material compactness that is positively affected by its humidity content (water is a good vehicle of diffusion of ultrasonic waves) and the presence of steel.

Figure 3.1 illustrates one of the stages of execution of sclerometric and ultrasound tests on the portal.



Figure 3.1: sclerometric test (left) and ultrasonic test (right) on a column of the portal

Sclerometer and ultrasonic, can be combined through a well-known technique called *Sonreb* method.

By correlating these two non-destructive methods with a formula that combines the two measurements it is possible to reduce the error affecting both and therefore acquiring a much more feasible estimate of strength.

The advantages of the method can be summarised as follows: while the sclerometric index is affected by superficial layer properties, the ultrasonics speed is affected by the internal part of the sample; on the other hand, the presence of an important amount of humidity produces an estimate in defect, of the sclerometer, and in excess for the ultrasonic.

The expression used in this thesis to estimate concrete strength is:

$$R = 7,695 \cdot 10^{-11} \cdot V^{2,6} \cdot S^{1,4} \quad \text{Eq. 3.2}$$

with R representing concrete compressive strength [MPa], V the average speed measured by the ultrasonics and S the average value of the rebound indexes acquired from sclerometric tests.

3.4.1 Non-destructive tests

The tables from 3.5 to 3.8 indicate the values collected, an estimate of the average values and a calculation of concrete compressive strength; Table 3.9 includes the values calculated using the Sonreb method.

<i>Sclerometric index</i>									
test number	1	2	3	4	5	6	7	8	9
column 1	40	43	41	41	42	43	41	41	44
column 2	43	42	40	43	43	44	40	42	42
Average column 1	41,7								
Average column 2	42,1								
Average	41,9								

Table 3.5: sclerometric test on portal 1

<i>Sclerometric index</i>									
test number	1	2	3	4	5	6	7	8	9
column 1	44	42	42	42	40	42	40	41	40
column 2	40	40	40	40	41	43	40	40	41

Average column 1	41,4
Average column 2	40,5
Average	41,0

Table 3.6: sclerometric test on portal 2

Measurements

[illegible]

Table 3.7: ultrasonic test on portal 1

Measurements

[illegible]

Table 3.8: ultrasonic test on portal 2

S_m [-]	41,166
V_m [m/s]	4177,99
R [N/mm ²]	36,4

Table 3.9: concrete compressive strength from Sonreb method

3.4.2 Destructive tests

Testing instruments and method are the same used for compression tests on mortar cylinders, as described in the previous chapter.

Values of cylindrical strength f_c , cubic strength R_c , elastic modulus E and the Poisson modulus ν have been achieved from experimental results.

Tests results are shown below:

Sample	E [MPa]	ν [-]	f_c [MPa]	R_c [MPa]
1	36704,47	0,288087	25.8	31.0
2	32048,24	0,216745	26.1	31.4
3	30701,83	0,205555	26.2	31.5
4	32223,48	0,222304	25.7	30.9
5	29934,11	0,166277	25.9	31.2
6	29681,52	0,203425	25.3	30.4
7	33442,17	0,205749	26.3	31.6
St. dev.	2432,94	0,036695	0.34	0.41
E_m	32105,12	average elastic module		[MPa]
ν_m	0,215449	coefficient of average Poisson		[mm/mm]
f_c	25.9	average cylindrical strength		[MPa]
R_c	31.2	average cubic strength		[MPa]

Table 3.10: destructive tests results

4. Experimental models

4.1 Introduction

This chapter describes the characteristics of all the structural types object of this study.

First of all the characteristics of the r.c. portal, modelled and also realized in four identical samples in the *Laboratory of experiments on materials and structures* of the University of Roma Tre, will be described; the portals have been used for the experimental activities that will be described in Chapter 7.

The other structures, adopted as numerical models only, are frames with the same r.c. structure of the frame from which the above mentioned portal has been extracted, but distinct from each other from a different infills layout; comparison is used to assess the influence of distribution of the walls on the structural response.

Subsequently the criteria adopted for modelling structures and performing numerical analyses carried out with the software of structural analysis *OpenSees* are described.

It is preliminary remarked that principles and constitutive models adopted for all of the numerical models are the same, regardless of geometry or the scale ratio adopted.

4.2 Description of the samples

The sample structures chosen can be distinguished in two groups: reinforced concrete frames with an identical structure but with different infill layout, that have been exclusively modelled, and the reinforced concrete portal representing one single link of the previous frames, that have been built and also modelled in a 1:2 scale ratio.

The structural type corresponds to one of the most diffused in Italy designed referring to the outdated Italian Code *D.M. LL.PP. 9.01.1996*.

The structures, according the concept provided from the mentioned Italian Code, are free of any of the structural details that modern structural design codes imposes in seismic areas. Nowadays in Italy the presence in seismic areas of structures designed to resist to vertical loads only is a frequent condition following the seismic reclassification of the country.

The mentioned portals, in accordance with the potentials of the structures available in the *Laboratory of experiments on materials and structures* of the University of Roma Tre, have been built in scale.

The impossibility of respecting the scale adopted with the commercial elements such as rebars and bricks selected for the infills has been taken into consideration in the choice of the scaling criteria. For this purpose it has been decided to build the portals in a 1:2 scale ratio, on the frame's plane, and in a 1:1 scale ratio in the orthogonal direction.

Maintaining the real depth of columns and beam has allowed for using commercial bricks: with the aim of reducing errors as much as possible, the smaller bricks available have been chosen.

The mentioned choices have definitely generated several differences that derive from the impossibility of completely respecting physical mechanisms in the scaling operation such as bond between steel and concrete or frame-infill interaction.

However for the question analyzed and for the scale ratios adopted such inaccuracies have been considered negligible.

If, however, we consider that the elastic modulus in walls is generally proportional to compressive strength, it is sufficient to imagine that the bricks chosen represent a different type with the same level of strength.

The scale factors adopted are shown in Table 4.1.

<i>Characteristic</i>	<i>Scale ratio</i>
<i>Thickness</i>	1:1
<i>Height, length, movement</i>	1:2
<i>Time, speed, period</i>	1: $\sqrt{2}$
<i>Tension, elastic modulus, acceleration</i>	1:1
<i>Stiffness</i>	1:1
<i>Bending moment</i>	1:4
<i>Diameter of the bars</i>	1: $\sqrt{2}$

Table 4.1: scale ratio factors

The vertical load acting on beam has not been considered, therefore the beam is a connecting element.

Figures 4.1 and 4.2 illustrate the structural details of the prototype sample: some details of rebar, such as the specific rebar of the beam's central area and of the joints, have the only function to allow the execution of the experimental tests, more details will be described in Chapter 7.

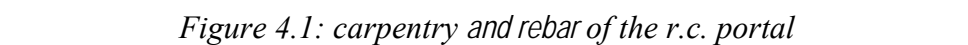


Figure 4.1: carpentry and rebar of the r.c. portal

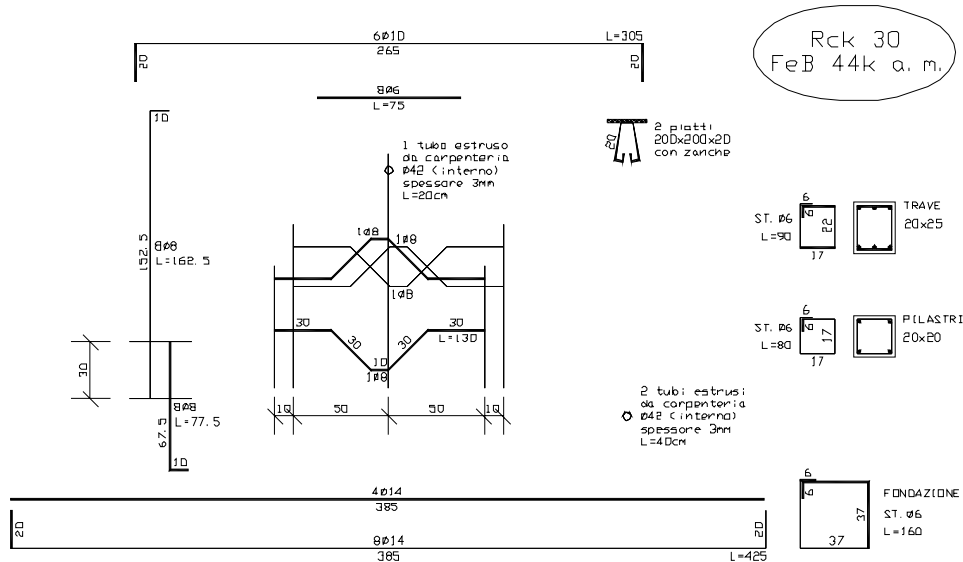


Figure 4.2: rebar of the r.c. portal

With reference to a building which layout and perspective are illustrated in Figures 4.3 and 4.4, the gravity loads acting on the base-central portal of the external frame have been calculated.

A dead loads of 5 kN/m^2 (additional to the weight of beams and columns) and a live load of 2 kN/m^2 have been chosen.

The structures have been designed to resist to vertical loads only, while their resistance to horizontal loads has been analyzed with the studies performed. In all the analysis discussed in this thesis the frame in a real scale ratio and consequently the portal have been considered stressed by gravitational loads in accordance with what the Italian Code *O.P.C.M.* 3274 indicates to be combined with seismic action.

Table 4.2 illustrates the analysis of loads for the structure in a 1:1 scale ratio; *Eq 4.1* is the load combination.

Loads N and nodal masses M allocated to each node of the structure (1:1 scale ratio 2D frame) are described in Table 4.3.

$$N = G_k + \psi Q_k$$

Eq. 4.1

G_k	=	5	kN/m^2
$Q_{k, floor}$	=	2	kN/m^2
$Q_{k, roof}$	=	2	kN/m^2
ψ_{21}	=	0,3	residences and offices
ψ_{22}	=	0,2	roofs

Table 4.2: analysis of loads of the frame (1:1 scale ratio)

first storey				
central nodes				
axial load per node	$N_{1,c}$	=	311.95	kN
nodal mass	$M_{1,c}$	=	10.90	t
side nodes				
axial load per node	$N_{1,s}$	=	155.98	kN
nodal mass	$M_{1,s}$	=	5.45	t
second storey				
central nodes				
axial load per node	$N_{2,c}$	=	218.75	kN
nodal mass	$M_{2,c}$	=	10.90	t
side nodes				
axial load per node	$N_{2,s}$	=	109.38	kN
nodal mass	$M_{2,s}$	=	5.45	t
Third storey				
central nodes				
axial load per node	$N_{3,c}$	=	98.05	kN
nodal mass	$M_{3,c}$	=	9.99	t
side nodes				
axial load per node	$N_{3,s}$	=	49.03	kN
nodal mass	$M_{3,s}$	=	5.00	t

Table 4.3: nodal loads ad masses of the frame (1:1 scale ratio)

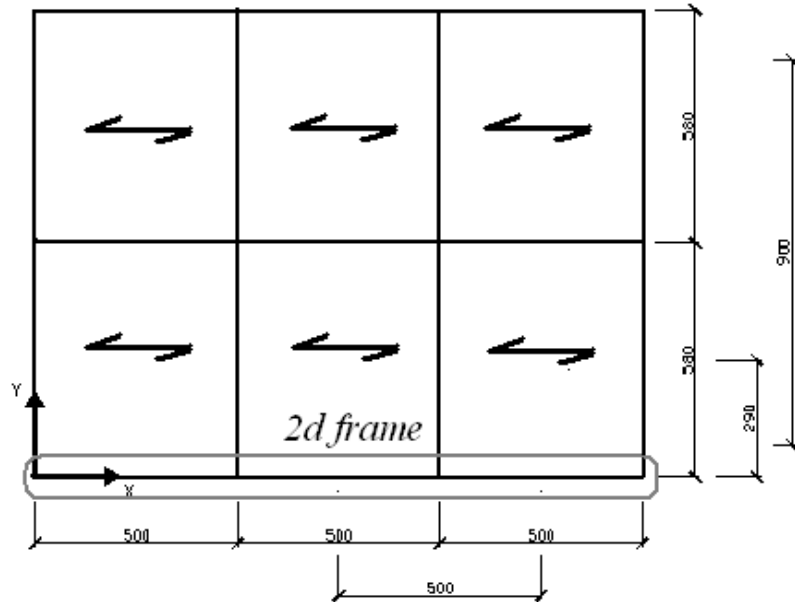


Figure 4.3: plans of the building which the frame examined belongs to (scale ratio 1:1, length in [cm], the frame is highlighted)

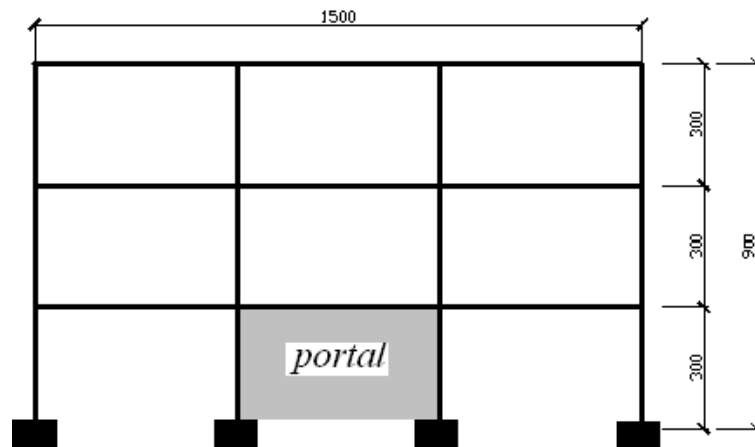


Figure 4.4: the frame analyzed (scale ratio 1:1), the position of the portal (realized in reduced scale ratio) is highlighted [cm]

Once the loads are known and the masses have been assessed for the structure in a real scale ratio, the corresponding values to be applied to

portal's nodes have been calculated: Figure 4.5 illustrates a portal specimen, the gravity load and nodal masses.

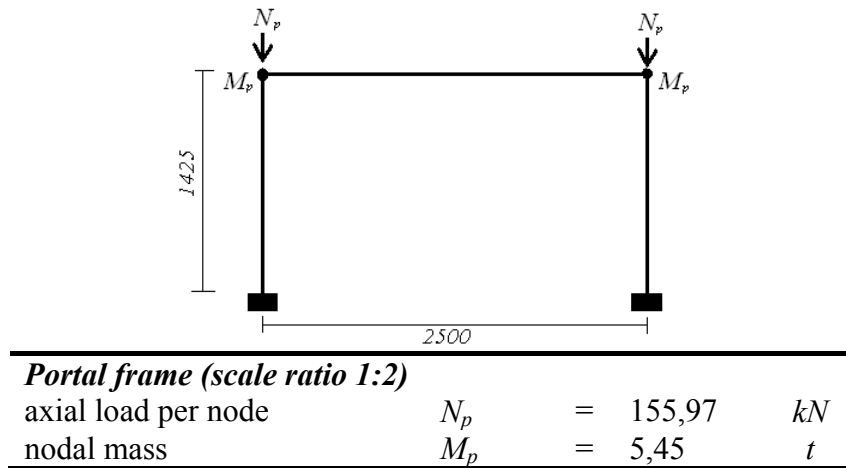


Figure 4.5: characteristics of the portal frame

4.3 Description of OpenSees

OpenSees is an open system for structural analysis, both linear and non linear: the development of this software has the objective of improve modelling and simulation in seismic engineering.

OpenSees allows to analysing the non linear response of systems modelled through a wide range of elements, materials and procedures.

The software consists of four main parts: the *Model Builder*, the *Domain*, the *Record Object* and the *Analysis Object*.

The creation of the *Model Builder* represents the first step towards modelling and consists in dividing of the structural body into frames and nodes, and it defines the acting loads and restrains. In order to register everything that has been defined in *Model Builder* and to make it accessible to analysis, the *Domain* is created. Subsequently, monitoring commands of the model need to be defined, these are the *Record Objects* that register all of the parameters defined by the user during the analysis.

The *Analysis Object* is, however, part of the software that is in charge of simulation, and it imposes the analysis' steps on the model.

4.4 Description of the numerical model

The global model consists in a division of single dimension elements according to the following hierarchy:

- beams or columns have been divided up into one or more single dimension non linear elements;
- a flat section perpendicular to element's axis has been associated for each Gaussian point;
- each section has been divided up into a specific number of fibres;
- a specific constitutive model is assigned to each fibre: unconfined concrete, confined concrete, steel.

As previously described, there are three different materials adopted (unconfined concrete, confined concrete, steel), for each one a specific constitutive model have been chosen and calibrated, as described below.

It is important to underline that material constitutive models calibration has been performed referring to experimental tests performed on materials used to build the portal samples described in Chapters 3.

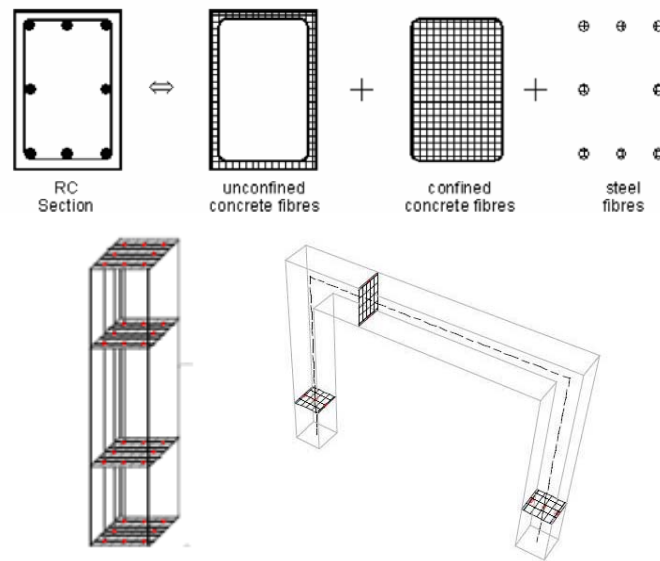


Figure 4.6: fibre-based model

For the confined concrete of beams and columns, that is the portion of section shut inside stirrups, and the unconfined concrete, that is the cover

area (outside stirrups), the model proposed by *Kent & Park* has been adopted: the law is constituted of the following three branches:

$$\begin{aligned}
 \varepsilon_c < \varepsilon_{c1} \quad \sigma_c &= f_c \left[\frac{2\varepsilon_c}{\varepsilon_{c1}} - \left(\frac{\varepsilon_c}{\varepsilon_{c1}} \right)^2 \right] \\
 \varepsilon_{c1} < \varepsilon_c < \varepsilon_{c20} \quad \sigma_c &= f_c [1 - z(\varepsilon_c - \varepsilon_{c1})] \\
 \varepsilon_c > \varepsilon_{c20} \quad \sigma_c &= f_c 0.2
 \end{aligned} \tag{Eq. 4.2}$$

where:

- ε_{c1} strain at the stress peak, equivalent to 2‰;
- ε_{c20} strain corresponding to 20% of maximum stress;
- ε_{c50} strain corresponding to 50% of maximum stress;
- f_c concrete compression strength;

$$\begin{aligned}
 z &= \frac{0.5}{\varepsilon_{c50} - \varepsilon_{c1}} \\
 \varepsilon_{c50} &= \frac{3 + 0.29 f_c}{145 f_c - 1000}
 \end{aligned} \tag{Eq. 4.3}$$

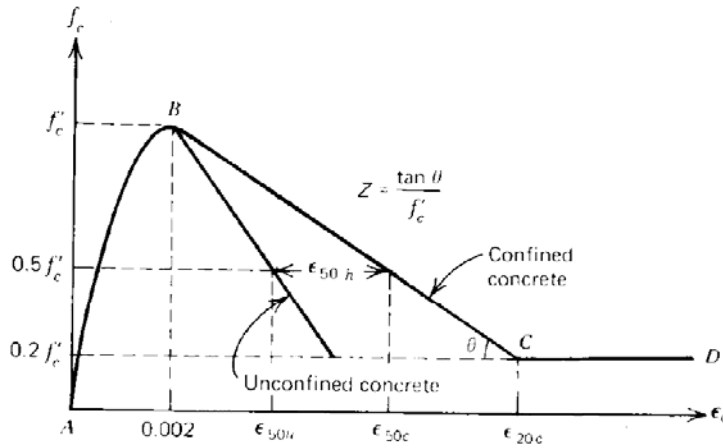


Figure 4.7: Kent & Park concrete model

The compressive strength of confined core is directly related to the effective confining stress the can be developed at yeld of the transverse reinforcement. In order to consider that the following expression can be adopted:

$$\begin{aligned}\sigma_{cc} &= \sigma_c k \\ k &= 1 + \omega_w \\ \omega_w &= \rho_w \frac{f_{yw}}{f_c}\end{aligned}\tag{Eq. 4.4}$$

where:

ρ_w effective section area ratios of transverse reinforcement;
 f_{yw} steel traction strength.

The material selected in the *OpenSees* library to model confined concrete and uconfined concrete has been *CONCRETE02*. In the following paragraphs, the *stress-strain* curves of the unconfined and confined concrete fibres for the existing elements are described.

Traction behaviour of the concrete has been considered by presuming a brittle elastic trend.

The tensile strength f_{ct} has been adopted equal to 14% of the compression strength. The elastic modulus of the branch of traction has been assumed equal to:

$$E_t = \frac{f_{ct}}{0.002}\tag{Eq. 4.5}$$

Furthermore, the cyclic behaviour of concrete has been characterised, referring to the experimental data achieved. The model adopted for the concrete allows, if a cyclic analysis is performed, for an assessment of the cyclic degradation of resistance as well as the variation of the elastic modulus following the diffusion of cracks with expansion of the cycles.

In the same way as the method performed for the concrete, the mechanical characteristics of steel, determined through experimental tests, have been used to define the parameters of the steel model *STEEL02* available in *OpenSees*.

In the following paragraphs the *stress-strain* curves assigned to steel fibres will be explained.

The following diagrams represent the constitutive models adopted in modelling in *OpenSees*.

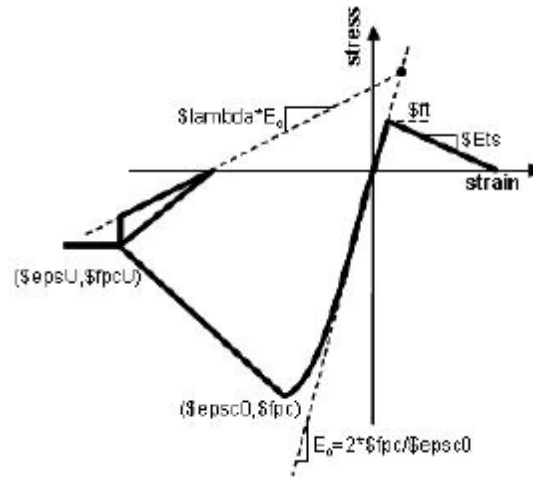


Figure 4.8: analytical response for cycling load of concrete

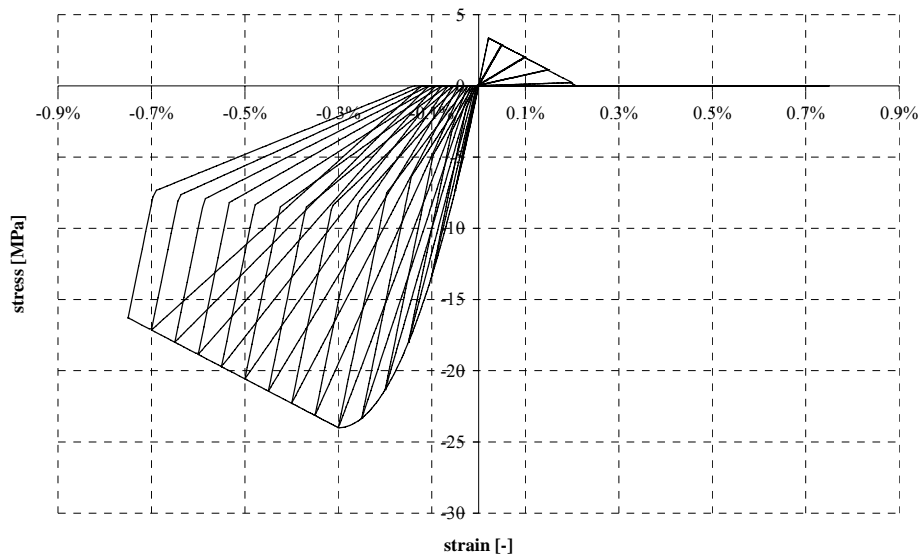


Figure 4.9: OpenSees CONCRETE02 response for cycling load (unconfined concrete)

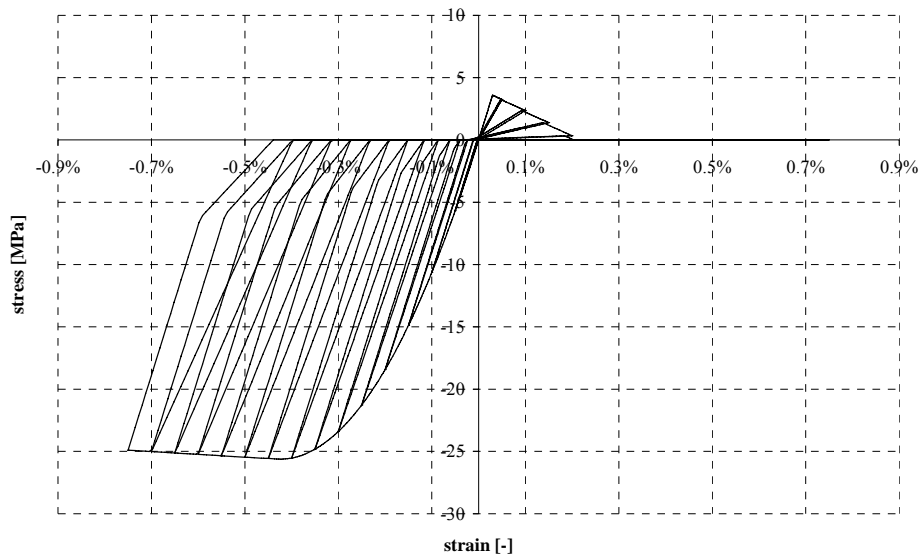


Figure 4.10: OpenSees CONCRETE02 response to cycling load (column confined concrete)

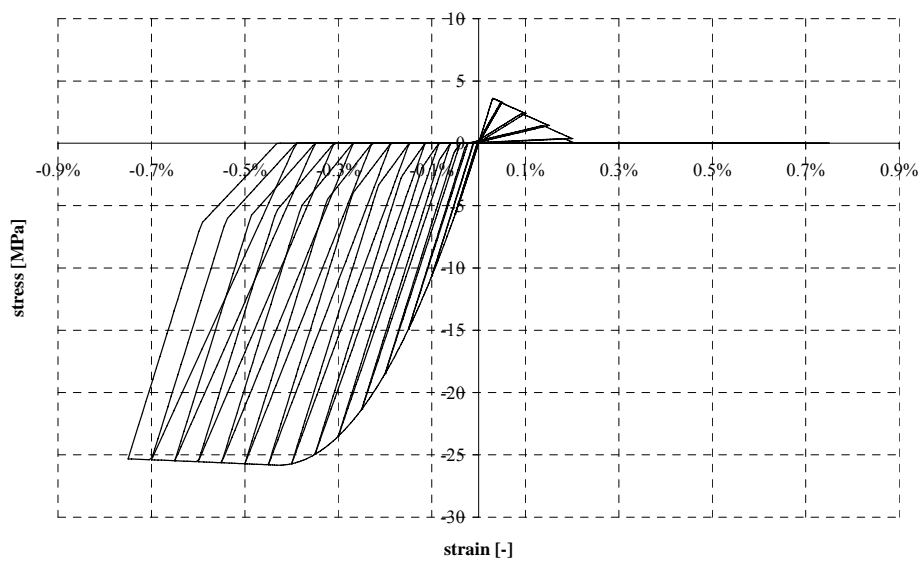


Figure 4.11: OpenSees CONCRETE02 response to cycling load (beam confined concrete)

In Figure 4.12, the type of element adopted in the model and the restrains of the adopted are indicated alongside each structural element.

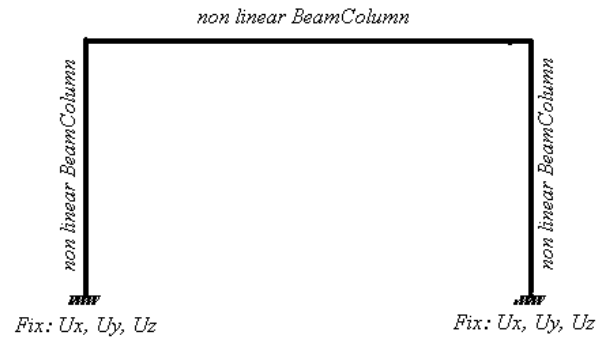


Figure 4.12: OpenSees model of the portal

Once the non linear elements that form beams and columns have been defined the *moment-curvature* relationship of each sections has been provided.

The *moment-curvature* curve of columns and beams forming the portal in question are illustrated below.

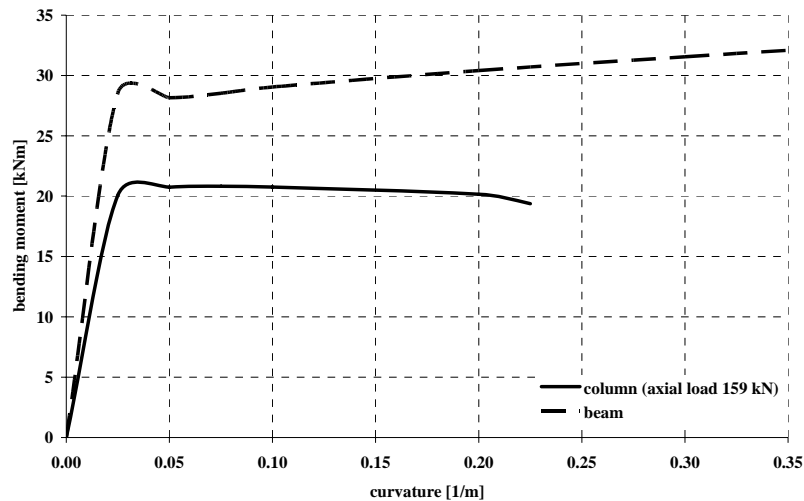


Figure 4.13: curvature–moment relationship of portal's sections

On the models described, with the objective of performing a static non-linear analysis (herein after referred to as *pushover*) as well as the vertical loads and the masses previously defined, horizontal nodal loads have been allocated. The *pushover* analysis has been performed with displacement control, therefore by increasing the horizontal nodal loads until achieving the desired displacement increase at each step of the analysis: the analyses have been pushed up until structural collapse.

4.5 Description of the 1:1 scaled frame

The same models implemented for the portal frame described in the previous paragraph, have been extended to the frame (scale ratio 1:1) consisting of three stories and three bays.

The materials adopted for developing of this frame are the same ones used for the portal frame, which characteristics have been determined on an experimental level and are described in the relative chapter. The procedure adopted to implement the models in Opensees is the same one as previously described for the portal frames.

Details of the framework of the typical sections of beams and columns for the structure model in a 1:1 scale ratio are provided.

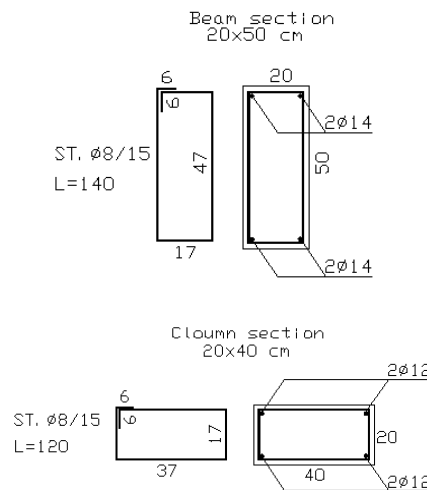


Figure 4.13: resistant sections of beams 50x20 cm (top) and columns 40x20 cm (bottom) of the frame (scale ratio 1:1)[cm]

Also for the section of beams and columns of the frame, by virtue of the loads calculated and described in the previous paragraph, the diagrams of moment-curvature are provided.

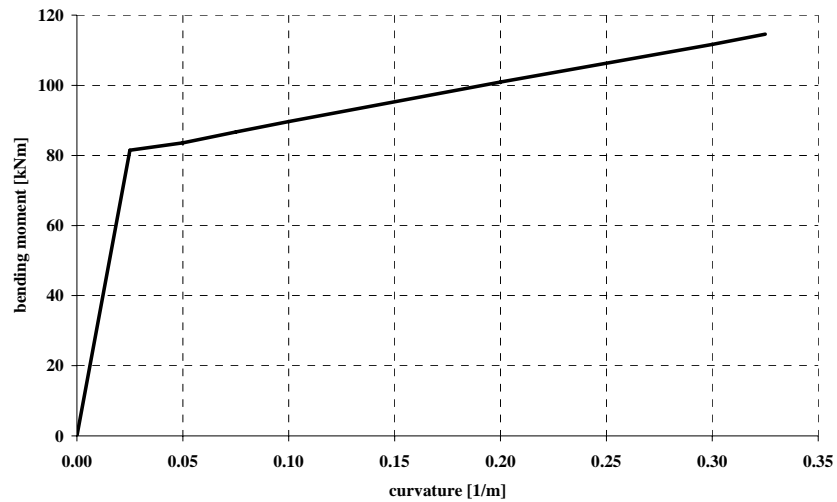


Figure 4.14: curvature-moment relationship of frame's beams

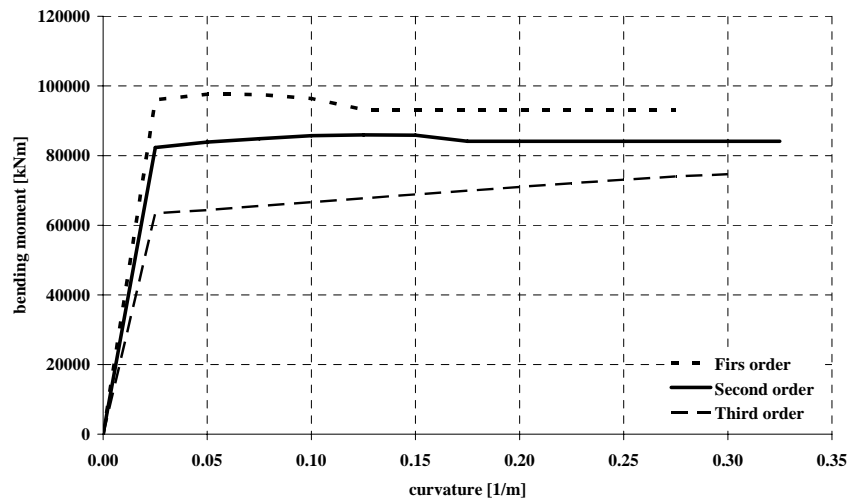


Figure 4.15: curvature-moment relationship of frame's columns

5. Global models of Infilled r.c. frames

5.1 Introduction

This chapter describes the methods adopted in this study for modelling the masonry infilled r.c. frames, specifically the strut infill models.

It is important to highlight how the objectives of the models discussed herein are not to seize the mechanisms of resistance of the infill but to assess interaction with the reinforced concrete frame that constitutes the structural component.

With these objectives, many technical and scientific documents include several models that provide information on the effects that brickwork has on the global reaction of the structure to horizontal loads, such as seismic action, without excessively increasing computational costs.

These models, called *global*, replace the wall with simple strut elements, that connect diagonally the nodes of the frame; the mechanical and geometric characteristics of strut elements presented in some of the existing models will be discussed in this chapter.

Besides these models, which characteristics are well known, it is necessary to have direct knowledge of the mechanical properties of the material used in order to build the walls: in this study it has been possible to apply modelling by using the experimental details collected on the walls examined during the same experimental campaign; for further details, reference is made to Chapter 2 dedicated to the experimental activities on materials and walls with specific reference to the walls built using half-full bricks and type 2 mortar.

Use of the *global* models for studying infilled frames implies a choice and therefore calibration of constitutive and phenomenological relationship.

5.2 Structural response of infilled frames

This paragraph describes the main principles on which infill modelling is based, through the *global* models chosen in this study that are also called *single strut model* and *triple strut model*.

With reference to the simple layout of an infilled portal subject to horizontal load (Figure 5.1), the following can be deduced:

In an elastic range, and therefore in absence of cracks in the wall and detachment from the framing structure that contains it, it is possible to presume that the reaction of the infilled frame is that of a composed shelf consisting of the wall and the columns that confine it.

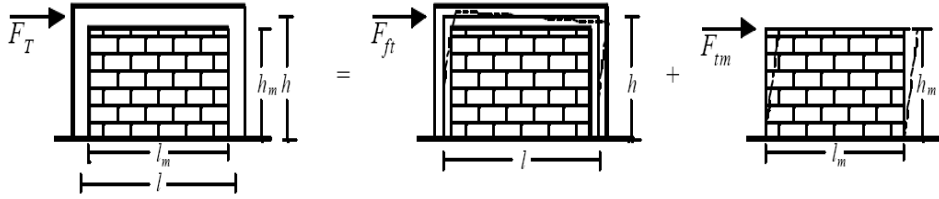


Figure 5.1: shelf consisting of frame and infill

Considering the above, flexibility of the composed shelf, K_T^{-1} (with K_T being stiffness of the composed shelf), is equivalent to the amount of flexural deformation of the frame, K_{ft}^{-1} , and of shear deformation of the wall, K_{tw}^{-1} .

$$\frac{1}{K_T} = \frac{1}{K_{ft}} + \frac{1}{K_{tw}} \quad \text{Eq. 5.1}$$

being:

K_{fc} flexural stiffness of r.c. columns adopting the elastic modulus E_c and a full section without cracks A_c ;

K_{fw} flexural stiffness of the infill panel adopting the elastic modulus in a vertical direction E_{wv} and thickness t_w ;

The flexural stiffness of the frame K_{ft} is equivalent to:

$$K_{ft} = K_{fc} + K_{fw} \quad \text{Eq. 5.2}$$

with:

$$K_{fc} = \frac{3E_c}{h^3} \left(2I_c + \frac{2A_c l^2}{4} \right) \quad \text{Eq. 5.3}$$

$$K_{fw} = \frac{3E_{wv} I_w}{h_w^3} = \frac{3E_c}{h^3} \left(\frac{E_{wv} h^3 t_w l_w^3}{E_c h_w^3 12} \right) \quad \text{Eq. 5.4}$$

$$I_w = \frac{t_w l_w^3}{12} \quad \text{Eq. 5.5}$$

From previous reports, the following relationship is achieved:

$$K_{fi} = \frac{3E_c}{h^3} \left(2I_c + \frac{2A_c l^2}{4} + \frac{E_{vw} h^3}{E_c h_w^3} I_w \right) = \frac{3E_c}{h^3} I^* \quad Eq. 5.6$$

Where I^* is the fictitious inertia valid in the initial phase without any cracks. As far as shear stiffness is concerned, reference can only be made to the contribution provided by the infill:

$$K_{tw} = \frac{G_w t_w l_w}{h_w} \quad Eq. 5.7$$

Therefore the total stiffness of the composed shelf is:

$$K_T = \frac{3E_c I^* G_w t_w l_w}{h^3 (G_w t_w l_w) + h(3E_c I^*)} \quad Eq. 5.8$$

5.3 Single strut model

As previously mentioned the most common methods for modelling of the infill consist in replacing, in order to simulate *infill-structure* interaction, the wall with a strut. This way the models are intuitive and easy to apply, therefore much more similar to real behaviour in terms of resistance and stiffness also in the case of complex structures. The global stiffness of the *frame-strut* system, K_P , is achieved by considering the two elemental systems in parallel and therefore adding together the flexural stiffness of the bare cracked frame, K_{tff} , with the stiffness to horizontal translation of the free node of the *diagonal strut-taut column* system, K_{cp} (Figure 5.2).

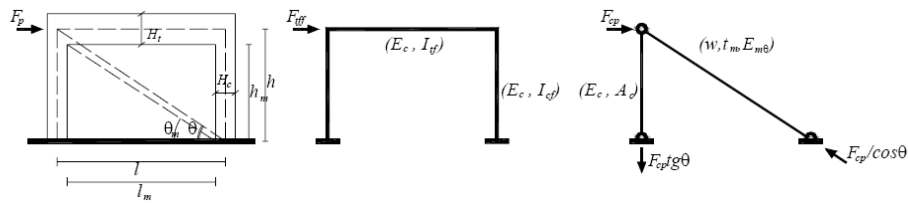


Figure 5.2: stiffness of the bare frame and the diagonal strut in parallel

$$K_P = K_{tff} + K_{cp} \quad Eq. 5.9$$

The flexural stiffness of the bare frame has the following formula:

$$K_{tff} = \frac{12EI}{h^3} = \frac{12E_c I_{cf}}{h^3} \left(\frac{6I_{tf}h + I_{cf}l}{3I_{tf}h + 2I_{cf}l} \right) \quad Eq. 5.10$$

Where it is good practice to consider the cracked values of the inertia of the beam, I_{tf} , and also of the column, I_{cf} .

The stiffness of the *diagonal strut-taut column* system is:

$$K_{cp} = \left(\frac{1}{K_{ct}} + \frac{1}{K_{w\theta}} \right)^{-1} = \frac{1}{\frac{htg^2\theta}{E_c A_c} + \frac{d}{b_w t_w E_{w\theta} \cos^2 \theta}} \quad Eq. 5.11$$

where, for simplicity, the section of the full column A_c is considered (as the presence of the vertical compressive load is known) and it is indicated with $E_{w\theta}$ the elastic modulus of the infill along the diagonal and with b_w the height (on the panel's plane) of the diagonal strut.

The following expression obtained due to the global stiffness of the composed shelf is achieved:

$$K_p = K_{tff} + K_{cp}$$

$$K_p = \frac{12E_c I_{cf}}{h^3} \cdot \frac{6I_{tf}h + I_{pf}l}{3I_{tf}h + 2I_{pf}l} + \left(\frac{htg^2\theta}{E_c A_c} + \frac{d}{b_w t_w E_{w\theta} \cos^2 \theta} \right)^{-1} \quad Eq. 5.12$$

By comparing bending moments action on the frame with those that correspond to cracks in the walls, we can deduce that the frame are in an elastic range when the cracking of the infill occur. Therefore from the measurement of stiffness of the samples with the cracked wall, K_{TP} , it is possible to determine the axial stiffness of the ideal diagonal strut $K_{w\theta}^*$, equivalent to the infill.

Therefore the following expression is known:

$$K_{TP} = K_T = K_{ft} + K_{cp}^* = \frac{12E_c I_{cf}}{h^3} \cdot \frac{6I_{tf}h + I_{pf}l}{3I_{tf}h + 2I_{pf}l} + \left(\frac{1}{K_{ct}} + \frac{1}{K_{w\theta}^*} \right)^{-1} \quad Eq. 5.13$$

It is possible to calculate, in correspondence with the end of the phase characterised by perfect adhesion between the wall and the frame, the stiffness of the infilled frame as follows:

$$K_{w\theta}^* = \frac{E_{w\theta} t_w b_w}{d_w} \cos^2 \theta = K_{TP} - K_{ft} \quad Eq. 5.14$$

where K_{ff} and K_{fi} are, respectively, stiffness of the frame with a cracked infill and of the frame without cracks in the concrete and without infill.

5.4 Infill constitutive material model

Definition of the constitutive material model (*load-displacement* and *stress-strain* curves) represents an important phase in the definition of the model in order to gain the real structural behaviour.

The model adopted in this thesis is a curve proposed by *Combescure* (1996) consisting of 4 branches, initially it has been calibrated as suggested by the author on the basis of the experimental data determined by tests on walls (walls realized with half-full bricks and type 2 mortar) and afterwards comparing the initial model with the results of tests on portals; experimental tests on portals and the following model calibration are discussed in Chapter 7.

As first step the model proposed by *Combescure* (1996) has been defined in all of its four branches. The first one represents the non cracked behaviour, the second one is characterized, for progression of cracks, by a lower stiffness. The third branch, characterized by a constant acting load, simulates failure of the wall and is followed by the fourth softening branch simulating collapse.

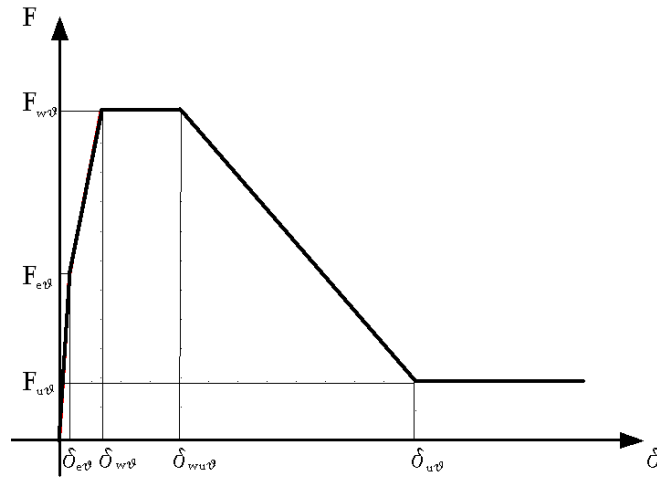


Figure 5.3: strut model proposed by (Combescure 1996)

For the definition of the curve it is necessary to determine the parameters that describe the behaviour of frame and infill: in particular the compression strength and the diagonal elastic modulus of the infill should be defined.

$$F_{w\theta} = f_w \cdot t_w \cdot b_w \quad \text{Eq. 5.15}$$

The parameter of the Eq. 5.15 are the thickness of the wall t_w , the width of the strut b_w and the compression strength of the wall (along the diagonal direction) f_w .

The term t_w is known by the geometry of the wall while b_w can be determined through one of the formulas available in literature, as described below.

Initially f_w has been assumed, as a starting hypothesis, as the average value of the strength determined during vertical and horizontal tests on walls.

The elastic modulus of the infill has been determined starting from the elastic modulus, assessed by the results of the compression tests, in a parallel and orthogonal direction in relation to the holes's direction. It is known that for an orthotropic material, in a state of biaxial stress, the normal elastic modulus $E_{w\theta}$ in the inclined direction is:

$$E_{w\theta} = \frac{1}{\frac{\cos^4 \theta}{\overline{E_{wo}}} + \frac{\sin^4 \theta}{\overline{E_{wv}}} + \sin^2 \theta \cdot \cos^2 \theta \left(\frac{1}{\overline{G_w}} - 2 \frac{\overline{\nu_{vo}}}{\overline{E_{wo}}} \right)} \quad \text{Eq. 5.16}$$

In Eq.5.16 the overlined symbols represent the input values obtained from experimental tests and the Poisson modulus is expressed as:

$$\nu_{vo} = \frac{2\overline{\nu}}{\left(1 + \frac{\overline{E_{wv}}}{\overline{E_{wo}}} \right)} \quad \text{Eq. 5.17}$$

The parameters of the model used have been determined, as described below, on the basis of the proposal made by the author himself.

The cracking load of the infill has been assumed as the 50% of the maximum load and therefore:

$$F_{e\theta} = \frac{F_{w\theta}}{2} \quad \text{Eq. 5.18}$$

Displacement in correspondence with the first crack may be defined as:

$$\delta_{e\theta} = \frac{F_{e\theta}}{2K_{w\theta}^*} \quad \text{Eq. 5.19}$$

The second branch of the curve has an inclination equivalent to the stiffness of the infill, therefore the horizontal displacement value for which the peak load is obtained is given by:

$$\delta_{w\theta} = \frac{f_w}{E_{w\theta}} d_w \quad \text{Eq. 5.20}$$

with:

d_w *length of the diagonal strut*

The plastic branch corresponds to the displacement, $\delta_{wu\theta}$, determined by presuming a stiffness value equivalent to what corresponds to a strut of width b_w .

In this study, the following has been assumed:

$$\delta_{wu\theta} = 0,005 \frac{h_w}{\cos \theta} \quad \text{Eq. 5.21}$$

Unanimously with *Combescure* (1996) the branch characterised by a negative inclination has been achieved on the basis of the following parameters:

$$\delta_{u\theta} = 18\delta_{w\theta} \quad \text{Eq. 5.22}$$

$$F_{u\theta} = \frac{F_{w\theta}}{10} \quad \text{Eq. 5.23}$$

5.4.1 Determination of the single strut dimension

The model described in the previous paragraph is affected by the determination of b_w . In the phase of elastic monolithic behaviour and in the cracking range, a gradual detachment occurs between the wall and the frame; an infill panel subject to horizontal action resists to external action according to resistance and deformation of the frame and also of the masonry. These parameters are connected with the mechanical characteristics of materials as well as the geometric dimensions of the structure. In particular, the relationship between b_w and the length of the diagonal strut d_w is correlated to the actual stiffness of the infilled structure that is being analysed.

In order to determine b_w , among the numerous formulas present in literature, the proposal made by *Mainstone* (1974) has been used, whose formula is:

$$\frac{b_w}{d_w} = 0.192 \sin(2\theta) \left(\frac{E_w g t_w h^4 \sin(2\theta)}{E_c I_p h_w} \right)^{-0.1} \quad \text{Eq.5.24}$$

Following the calculation of the strut height, all the information required to define the *load-displacement*, as described in the previous paragraph, is known.

The parameters determined as previously described, for the infilled portal (scale ratio 1:2, half-full bricks and type 2 mortar), are summarised below.

It is important to point out that for all of the analyses described in this study, mechanical characteristics of materials will remain the same, therefore the values indicated should be considered valid for the entire study.

Concrete

f_c	25.86	MPa	Average compression strength of the concrete
E_c	32105.00	MPa	Elastic modulus of the concrete

Steel

f_y	564.00	MPa	Average yielding stress of steel
-------	--------	-----	----------------------------------

Infill (half-full bricks and type 2 mortar)

	5.29	MPa	Average compression strength
f_{wkv}			(vertical load)
f_{wko}	2.67	MPa	Average compression strength
			(horizontal load)
E_{wv}	8097.80	MPa	Vertical elastic modulus
E_{wo}	3939.41	MPa	Horizontal elastic modulus
$E_{w\theta}$	4682.88	MPa	Diagonal elastic modulus
$f_{w\theta}$	3.98	MPa	Diagonal resistance of the strut
			(first hypothesis)
G_w	2643.43	MPa	Shear modulus
ν	0.14	-	Poisson coefficient

Table 5.1: summary of mechanical infill's parameter adopted

Frame	
l	<i>Length of the frame</i>
h	<i>Height of the frame</i>
l/h	<i>dimension ratio</i>
Beam	
b	<i>base</i>
h	<i>height</i>
I_t	<i>inertia of the beam</i>
A_t	<i>cross section area</i>
Column	
b	<i>base</i>
h	<i>height</i>
I_p	<i>inertia of the column</i>
A_p	<i>cross section area</i>

Table 5.2: symbols adopted

5.5 Triple strut model

Interaction between the frame and the wall results in the columns being subjected to shear loads, so much so as possible to cause a brittle collapse. This mechanism cannot be predicted if the simple *single strut* model is adopted. It is therefore necessary to search for a struts layout that can also simulate the transfer mechanism of shear actions on columns. For this purpose a whole range of models have been created and widely discussed in the scientific literature replacing the *single strut* with a system of several struts: in this study reference is made to the so-called *triple strut model* proposed by *Biondi et al.* (1991). With this system, that will be investigated later on, three independent ad parallel struts are used (one on the main diagonal and the other parallel above and below). The procedure states that, once the stiffness of the infilled frame have been defined, the position of the side struts can be defined according to contact stress distribution between the wall and the frame. The objective is to define a struts-frame system that, compared with the infilled frame, have the same level of stiffness, the same stress at the interface between wall and frame and therefore similar forces in beams and columns. While the first

objective may be achieved using a system with an equivalent single strut, the second may be achieved by using systems of more than one strut or a finite elements model. The system proposed by *Biondi et al.* (1991) is based on the hypothesis of congruency and equilibrium of forces and neglects the effects of interaction along the diagonal axis of the struts. The parameters that characterise the mentioned model are the position of the struts, that affects the level of stress transmitted to the r.c. elements, and the mutual dimension of each strut, that affects global stiffness of the system. For simplicity, starting from what has been discussed and determined previously, it is considered necessary to presume a level of stiffness equivalent to the one achieved with the *single strut* model.

The phases that characterise the definition of the global model with three struts, and that will be developed for the cases in question, can be summarised as follows:

- definition of geometry of the *triple strut* starting from the characteristics of the *single strut* by imposing the equivalence of stiffness in the elastic range;
- experimental definition of the constitutive model of the infill;
- definition of contact area between infill and columns, resulting in determining the position of the side struts;
- definition of the geometrical dimensions of the struts.

5.5.1 Determination of the triple strut geometry

In elastic range the reaction of the infill, in terms of horizontal, is represented by the equivalent strut model. By defining the horizontal stiffness of the infill with K in the case of a system with the *single strut*, and with $K_{\theta o}$ and $K_{\theta l}$ respectively the generic diagonal stiffness of the central and side struts of the system with the *triple strut*, the criteria of equivalence to horizontal translation is expressed with the following formula:

$$K = K_{\theta o} \cos^2 \theta + 2K_{\theta l} \left[1 - \left(\frac{z}{h} \right) \right]^2 \cos^2 \theta \quad \text{Eq.5.25}$$

The previous equation is obtained from the following formulas between horizontal components of load and displacement (F, δ) and the diagonal components $(F_{\theta}, \delta_{\theta})$, determined as follows:

$$F_{\theta} = \frac{F}{\cos \theta} \quad \text{Eq.5.26}$$

$$\delta_{\theta} = \delta \cdot \cos \theta \quad \text{Eq.5.27}$$

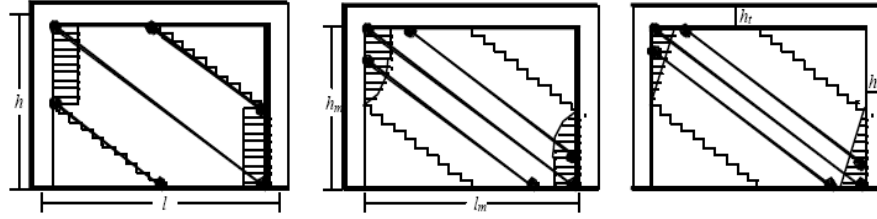


Figure 5.4: triple strut models with different distributions of contact stress between the infill and frame

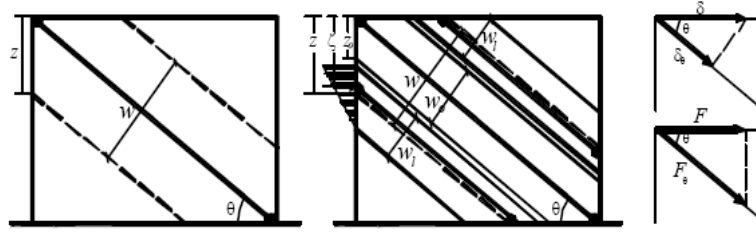


Figure 5.5: loads and stress components of the model

Aware of the criteria of equivalence to horizontal translation, it is possible to assume that:

$$b_w = b_{w0} + 2 \left(1 - \frac{\xi}{h} \right) b_{wl} \quad \text{Eq.5.28}$$

where b_{w0} and b_{wl} are respectively the height of the central and side struts, ξ represents the coordinate that identifies the position of the side strut.

By assuming a distribution of contact stress the side struts are identified by connecting them with the columns in correspondence with the barycentre of the stress. By presuming, as done so in this study, a triangular distribution of the contact stress along z (Figure 5.4 and 5.5) the following is obtained:

$$\xi = z_0 + \frac{z - z_0}{3} \quad \text{Eq.5.29}$$

where z_o is the ordinate of the central strut (Figure 5.4), from Eq. 5.29 the following is obtained:

$$w_o = \frac{b_w}{2} \quad \text{Eq.5.30}$$

$$w_l = \frac{b_w}{4 \left(1 - \frac{b_w}{3h \cos \theta} \right)} \quad \text{Eq.5.31}$$

The position of the side struts ζ is therefore equivalent to:

$$\zeta = z_1 + \frac{z - z_1}{3} = \frac{3z_1 + z - z_1}{3} = \frac{w}{6 \cos \theta} + \frac{2w_l}{3 \cos \theta} \quad \text{Eq.5.32}$$

Therefore, known what has been determined above, the area of the central strut is equivalent to:

$$A_{wo} = \frac{A_w}{2} = \frac{b_w t_w}{2} = b_{wo} t_w \quad \text{Eq.5.33}$$

Consequently the central strut's height is determined:

$$b_{wo} = \frac{b_w}{2}$$

The area of the side struts is however determined by the following formula:

$$A_{wl} = \frac{1}{4(1 - \zeta/h)} A_w = \frac{1}{4(1 - \zeta/h)} b_w t_w = b_{wl} t_w$$

with:

$$b_{wl} = \frac{b_w}{4(1 - \zeta/h)} \quad \text{Eq.5.34}$$

Imposing:

$$\alpha = \frac{\zeta}{h}$$

the following is obtained:

$$b_{wl} = \frac{b_w}{4(1 - \alpha)} \quad \text{Eq.5.35}$$

where α is equivalent to:

$$\alpha = \frac{b_w}{6h \cos \theta} + \frac{b_w}{6h \cos \theta (1 - \alpha)} \quad \text{Eq.5.36}$$

therefore:

$$\beta = \frac{b_w}{6h \cos \theta} \quad \text{Eq.5.37}$$

$$\alpha = \frac{1 - \alpha + 1}{1 - \alpha} \beta \quad \text{Eq.5.38}$$

$$\alpha^2 - (1 + \beta)\alpha + 2\beta = 0 \quad \text{Eq.5.39}$$

$$\alpha = \frac{(1 + \beta) \pm \sqrt{(1 + \beta)^2 - 8\beta}}{2} \quad \text{Eq.5.40}$$

Adopting the following solution:

$$\alpha_1 = \frac{(1 + \beta) - \sqrt{(1 + \beta)^2 - 8\beta}}{2} \quad \text{Eq.5.41}$$

therefore:

$$\zeta = \frac{(1 + \beta) - \sqrt{(1 + \beta)^2 - 8\beta}}{2} h \quad \text{Eq.5.42}$$

The models described in this chapter will be subject to applications on all the numerical models described in the following chapters.

6. Analyses results for the portal model

6.1 Introduction

The global models of the infill, adopting both the *single strut* and the *triple strut* models already described in Chapter 5, have been adopted for the structures analysed: it is important to remember that in the cases examined, the infill is considered as consisting of half-full bricks and type 2 mortar described in details in Chapter 2.

The results achieved from numerical analyses are now presented and discussed: the first target of this analysis was to allow for a correct preparation of the experimental activity to be performed on the same structures modelled (bare portal and infilled portal) and subsequently, after proper re-calibration, the creation of reliable models for future studies.

6.2 Numerical model of the portal with single strut

The descriptions provided in the previous chapters have been applied to the sample portals, the results achieved from the first analyses performed have provided valid indications for the set-up of the subsequent experimental tests.

As we can see from this chapter, the initial hypothesis on which initial modelling is based, has led to coherent results for an initial assessment of loads that may be developed during the tests on the real portal's samples, therefore allowing for the set-up of a well dimensioned experimental structure.

Following the aforementioned experimental activity, it was possible to perform calibration of the model by intervening exclusively on the sole step that was uncertain, the infill 's constitutive model.

A table is provided below illustrating the geometries adopted to define the resistant section of the strut.

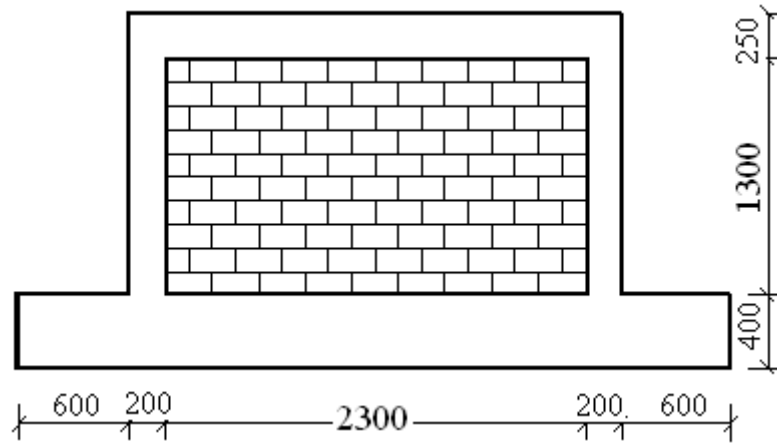


Figure 6.1: geometry of the infilled portal (width: r.c. elements=200 mm; wall=120 mm) [mm]

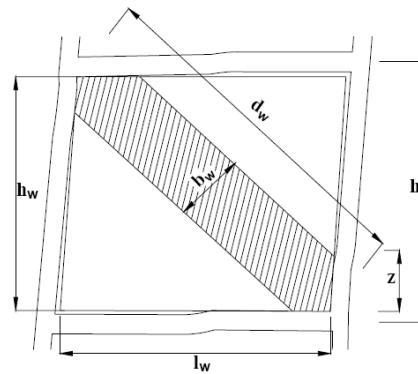


Figure 6.2: position of the equivalent strut

Geometric parameters of the single strut

l_w	2300	mm	length of the infill
h_w	1325	mm	height of the infill
d_w	2654.36	mm	length of the strut
θ	0.52	rad	inclination of the strut
t_w	120	mm	thickness of the panel
b_w	254.64	mm	height of the strut (Mainstone)

Table 6.1: parameters of the single strut model

The wide range of elements and materials available in *OpenSees* makes of this an extremely ductile instrument, allowing for excellent reproduction of the mentioned global model. In particular the element chosen for the strut is the *Truss element* and the material adopted in order to reproduce the infill's constitutive model is the *Hysteretic Material*.

The *Hysteretic Material* (Figure 6.3) is a material that allows, through 4 branches, the reconstruction of the model desired and, at the same time, calibration of pinching and stiffness decay. As previously mentioned, at the end of the experimental activities, a calibration of the infill model (*load-displacement* and *stress-strain* model) was performed. In particular a redefinition of the point of maximum strength and the extension of the plastic branch was performed. Observations found that once the geometry of the strut was defined, the constitutive model to be allocated to the infill, in order to gain the correct stiffness of the infilled frame, is mostly the same; the reduction of the plastic branch adopted depends on the substantial sliding registered during the experimental tests between two consecutive bricks layers. The decision to intervene only on the constitutive model of the infill originates from the fact that the numerical model of the bare portal has provided results that are strictly coherent with the experimental ones; furthermore, once the *capacity curve* (the capacity curve expresses the structural response to an increasing horizontal load or displacement in terms of *base shear-displacement*, this kind of analysis is commonly named *pushover*) of the bare portal and of the infilled portal have been determined, the *capacity curve* to be attributed to the strut was calculated as the difference of the first two. Initially, the resistance allocated to the strut (in detail to the material of which the strut is made of), was calculated as an average value of the resistance measured along the two main loading directions (vertical and horizontal), and were:

$$f_{w\theta,initial} = 3,98 \text{ MPa}$$

the subsequent redefinition of the parameters has increased it by 8%; the increase in strength can be attributed presumably to the confining offered by the r.c. frame, the value adopted is therefore:

$$f_{w\theta,calibrated} = 4,3 \text{ MPa}$$

Figure 6.4, 6.5 and 6.6 illustrate and compare the *load-displacement* diagrams adopted in the numerical model.

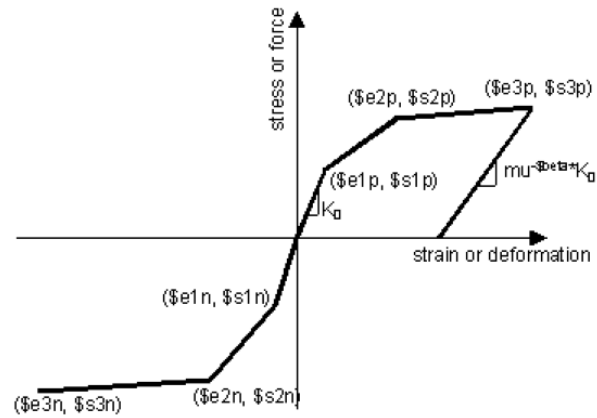


Figure 6.3: the Hysteretic Material

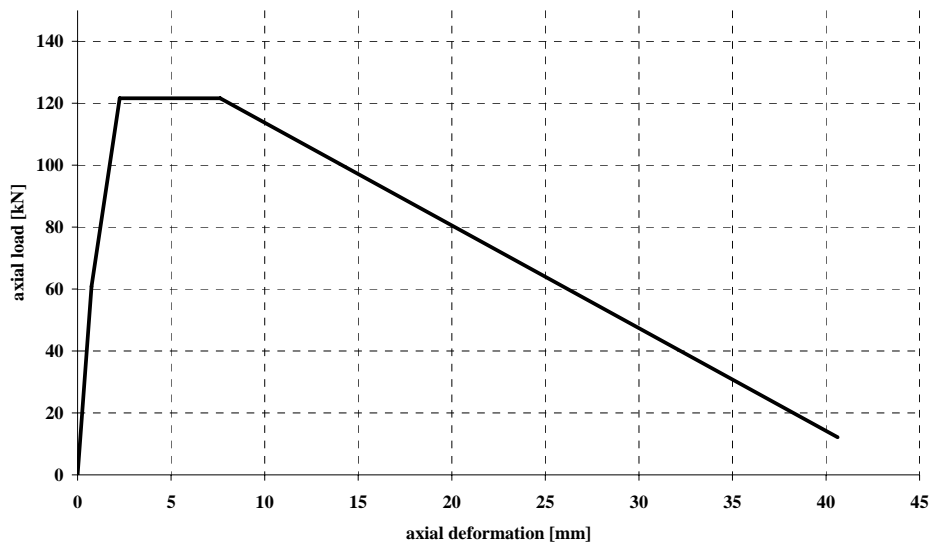


Figure 6.4: axial load–axial deformation of the single strut initially defined

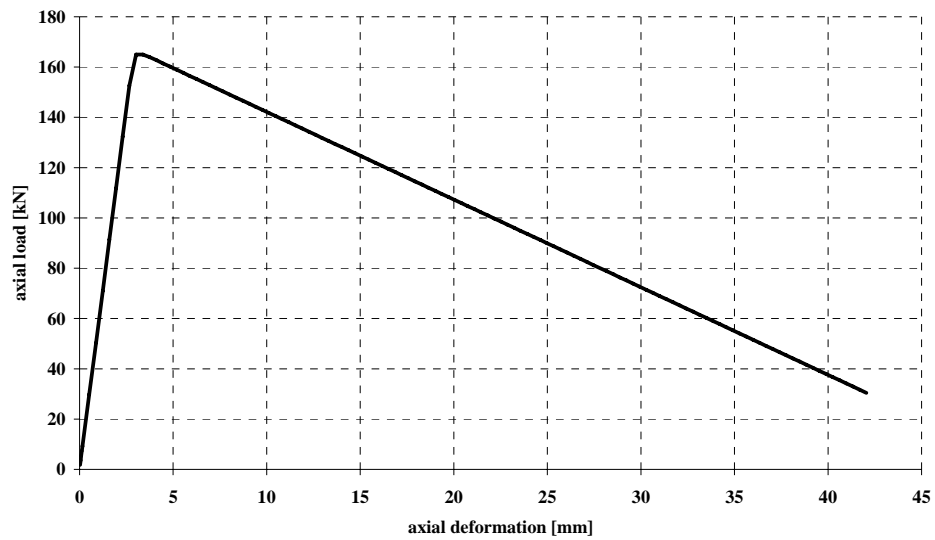


Figure 6.5: axial load-deformation of the calibrated single strut model

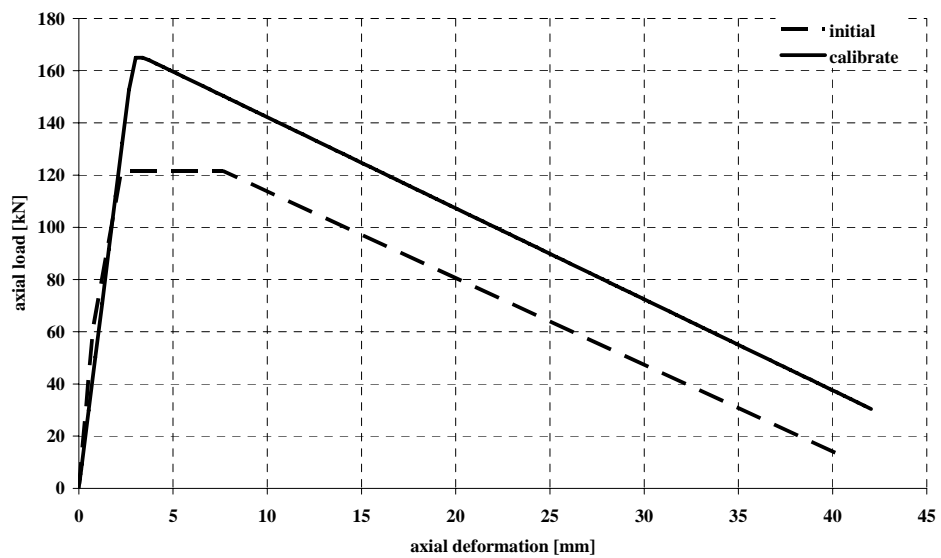


Figure 6.6: comparison between the model initially defined (initial) and the experimental one (calibrated)

In order to assess the global structural behaviour and to monitor the local response of the portal's structural elements, *pushover* analyses have been carried out.

It is important to remember that in order to perform the *pushover* analyses, an increasing horizontal displacement has been imposed at the top of the portals: the reaction of the structure is therefore determined through the *capacity curve* which represents *top displacement-base shear*. The results of the *pushover* analyses on the portal (Figure 6.7 refers to the portal with the *single strut* model) are presented and discussed: furthermore, the results achieved with the initial model are compared with those of the model calibrated on an experimental basis.

In Chapter 7, dedicated to the experimental tests on portal samples, results from numerical model have been compared with the experimental ones.

From Figure 6.8 it can be observed how the infill, in the equivalent strut model, increases strength and stiffness.

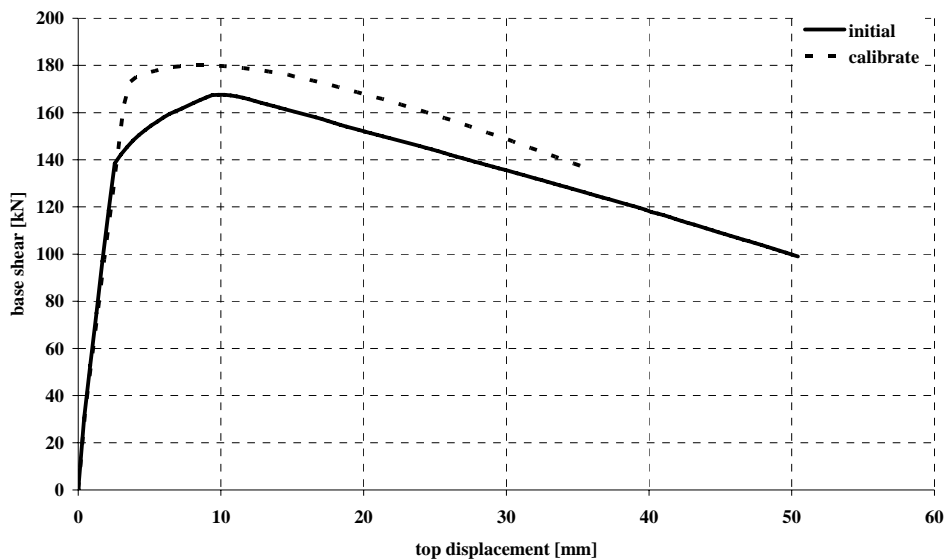


Figure 6.7: portal with the single strut: base shear – top displacement for the initial and the calibrated models

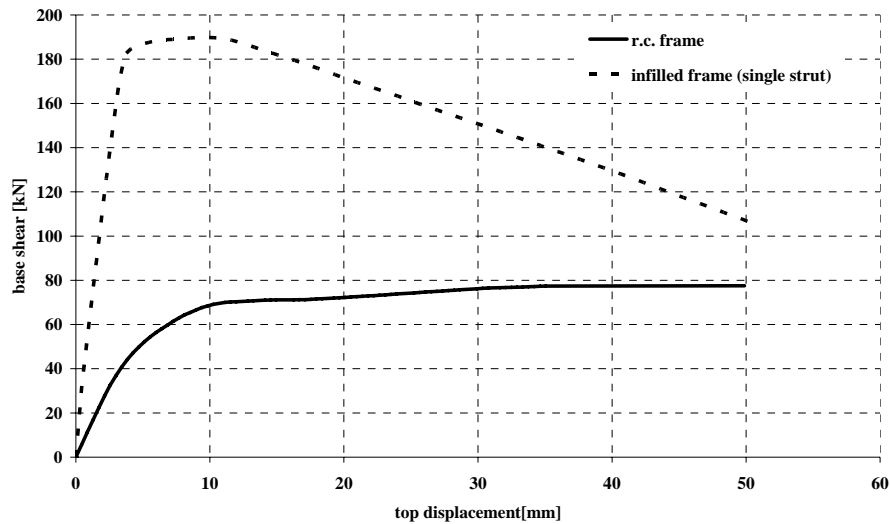


Figure 6.8: bare and infilled portal: base shear – top displacement

	F_{max} [kN]	K [kN/m]
<i>bare portal</i>	77.5	11924
<i>Infilled portal</i>	181.2	17038

Table 6.2: bare and infilled portal: maximum horizontal load and elastic stiffness

Once the global behaviour of the structure is known through the *capacity curves*, the state of strain and stress in the sections of columns and beam have been studied. This way has been determined the local state of all sections' fibres in order to identify arising and localisation of plastic hinges. Subsequently the numerical results achieved about the section state have been compared with the *capacity curve* with the objective of identifying the state of damage of the structure with an increase in displacement of the control node (as usually done has been selected one of the top nodes as control node). All of the operations described above have been performed for both the configurations of the portal, the results

are therefore compared in order to understand the effect of the infill, also on the structural sections. Some of the most important results achieved from the analysis described above for the portal (bare and infilled) are represented in the figures below.

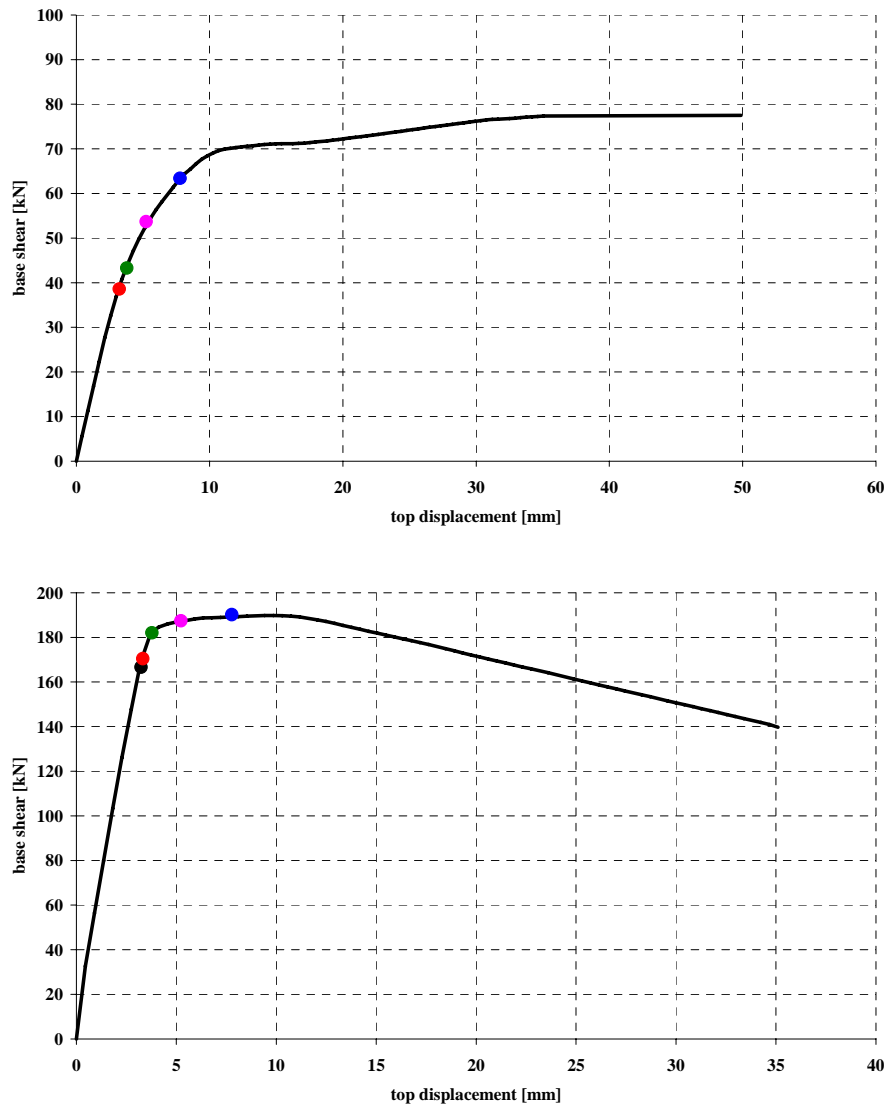


Figure 6.9: localization of plastic hinges on the capacity curve of the bare (top) and infilled portal with single strut model (bottom)

By observing Figure 6.9 and 6.10 we can see that the first plastic hinges are developed at the basis of the columns. In the infilled portal, even though the same plastic hinges are developed, strength of the strut governs the trend in the *capacity curve*: the elastic range appears to extend until reaching the maximum load of the equivalent strut.

The following figures compare the entity of the horizontal load absorbed by the strut and by the columns (Figure 6. 10).

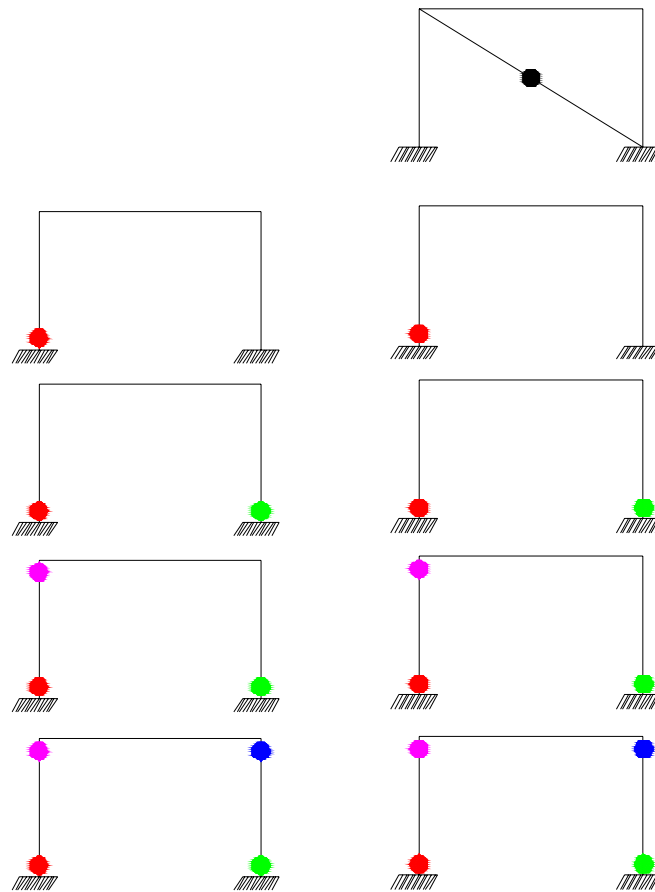


Figure 6.10: bare (left) and infilled (right) portal: localisation of plastic hinges

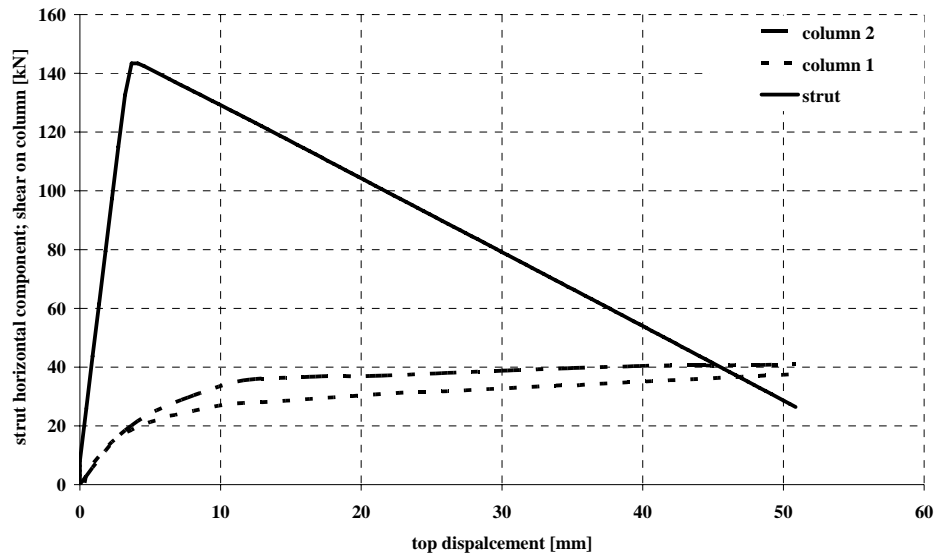


Figure 6.11: horizontal component of load on strut and shear on columns of the portal with single strut

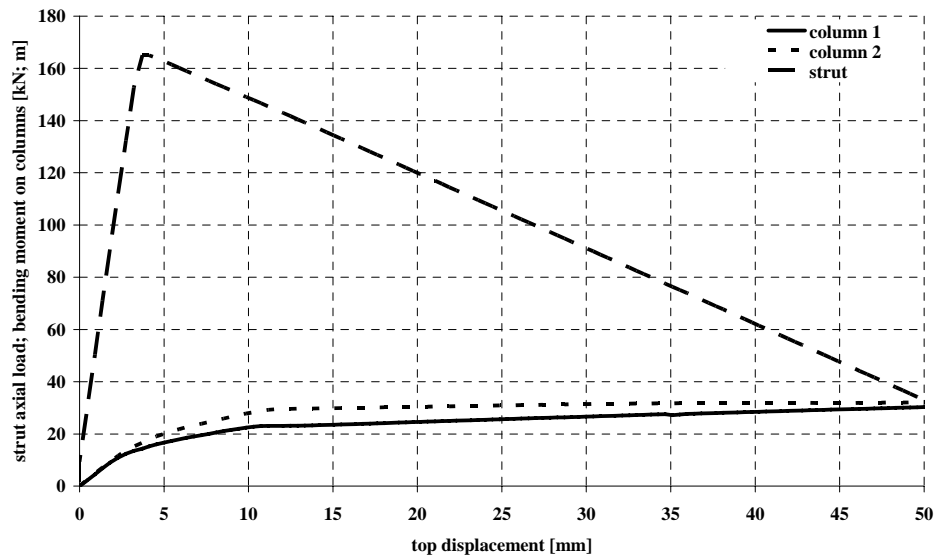


Figure 6.12: axial load on strut, bending moment on columns of the portal with single strut

It is interesting to observe how the contribution provided by the *single strut* does not affect neither plastic hinges formation sequence nor their localisation on the capacity curve (Figure 6.9). As can be seen with progressive deterioration of the resistance of the strut, the acting load is absorbed by the portal 's columns. The structure resists until it achieves a horizontal load equivalent to the total amount of the horizontal load sustained by the bare portal.

At collapse the following values are registered:

$$V_c \quad 75.7 \text{ kN}$$

$$V_s \quad 22.5 \text{ kN}$$

with:

$$V_c \quad \text{shear load absorbed by the columns upon collapsing}$$

$$V_s \quad \text{horizontal component of the axial load absorbed by the strut at the collapse}$$

We can see that the strut inserted in the portal increases the value of the maximum horizontal load that the structure resists to, it does not however affect the method of collapse and the maximum horizontal displacement achieved by the control node. The *capacity curve* of the portal with the *single strut* highlights, upon achievement of the maximum base shear load, a value of *interstorey drift* of 0.7% (the *interstorey drift* is the ratio between relative displacement of two consecutive levels and their vertical distance).

6.3 Analyses results for the portal with the triple strut model

In the same way as the procedure carried out for the *single strut* model, the principles described in the previous chapter have been applied in order to determine the characteristics of the *triple strut* model. The results achieved for the infilled portal are now discussed; Table 6.3 and Figure 6.13 illustrate the geometries of the model.

<i>Three strut model</i>		
β	0.03	<i>rad</i>
ζ	101.44	<i>mm</i>
b_{wo}	127.32	<i>mm</i>
b_{wl}	68.54	<i>mm</i>

Table 6.3: geometric parameters of the triple strut model

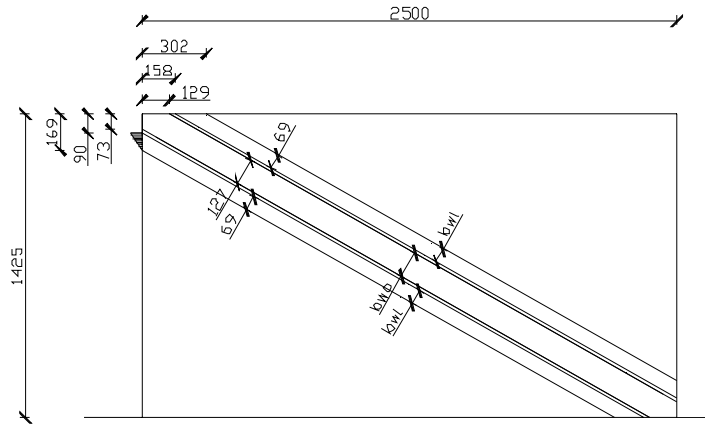


Figure 6.13: geometry of the triple strut

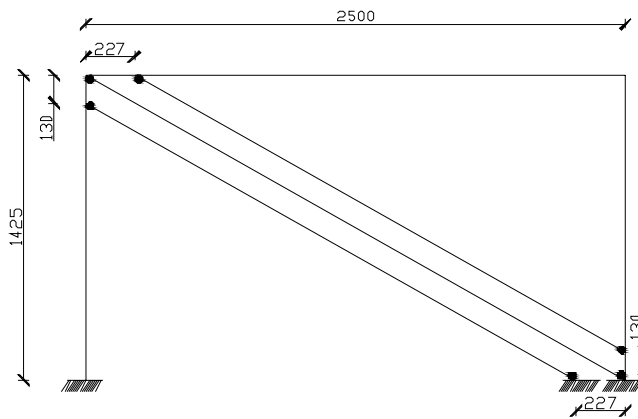


Figure 6.14: implemented triple strut model [mm]

Once the geometries are known, the *load-deformation* models are allocated to the struts (central strut and lateral struts) in the numerical model adopting the same method as the one previously described.

Figure 6.15 represents the relationship assigned to the struts of the numerical model. It is clear to point out that by adding together the maximum resistance of each one of the three struts, the maximum resistance of the single strut previously determined can be found.

The results achieved by performing a *pushover* analysis on the infilled portal with the *triple strut* model and comparison with the *single strut* model are presented.

From a comparison of the results discussed up until now between the *single strut* model and the *triple strut* model, they appear to be substantially equivalent.

But, as previously mentioned, the *triple strut* model has been developed with the objective to capture a variation in shear load acting on the columns; the value of the maximum shear along the length of the column is shown in Figure 6.20 and 6.21.

By observing Figure 6.20 and 6.21 it can be determined that the maximum shear load acting on the columns differs, for the two models adopted, by 33%.

It is important to point out that the graphics provided have been achieved considering the maximum shear condition: therefore they do not correspond to the same displacement state imposed to the control node.

In reality for the model with *single strut*, the shear on columns increases as the strut is damaged. On the contrary, with the *triple strut* model, shear on columns depends on the load transmitted by the side struts and reaches its maximum value in an intermediate condition.

Such considerations highlight how the *single strut* model, considering the results provided by the *triple strut* model as valid, not only underestimates the maximum shear but it is not able to define the real trend during the *pushover* analysis.

It is important to point out that if structural analysis methods are performed based on a non linear static analysis, it is extremely important to consider the above in order to provide a correct assessment of the *capacity curve* of the structure examined.

In reality if, following execution of the analysis, the structure has been found to reach and possibly exceed its own shear resistant capacity in any one of the sections, having adopted a *triple strut* model would not only allow to identify a much more valid value of acting load but also a correct localisation of the condition in which it is found.

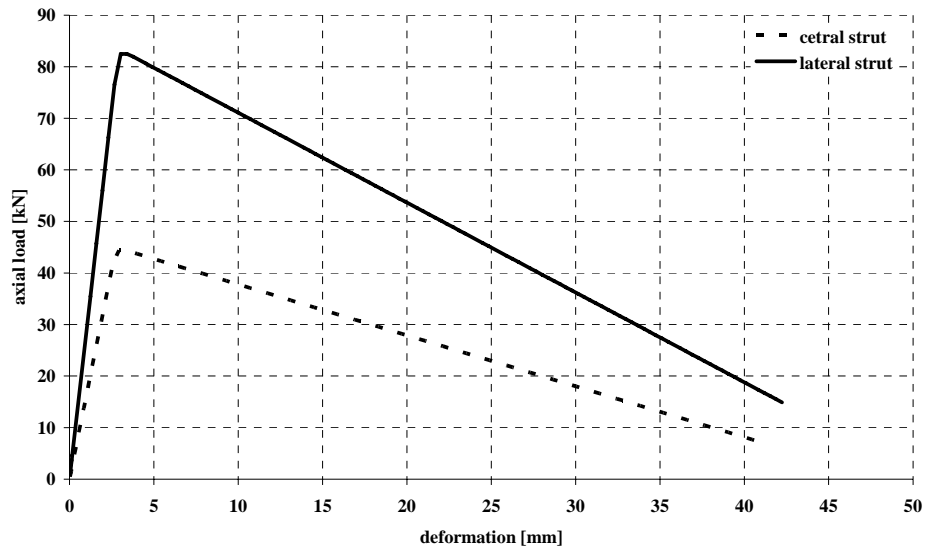


Figure 6.15: constitutive model of the triple strut

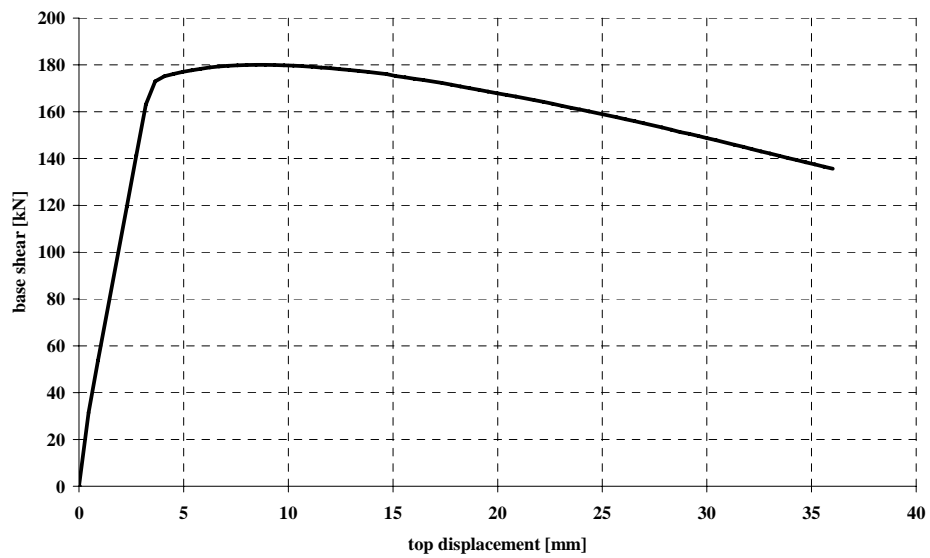


Figure 6.16: base shear-top displacement of the portal with triple strut

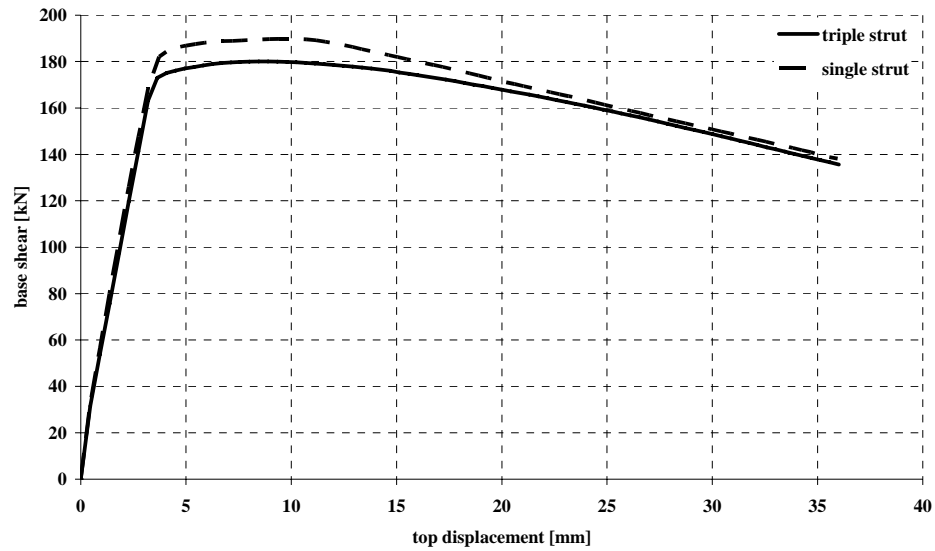


Figure 6.17: comparison between capacity curve of the infilled portal models

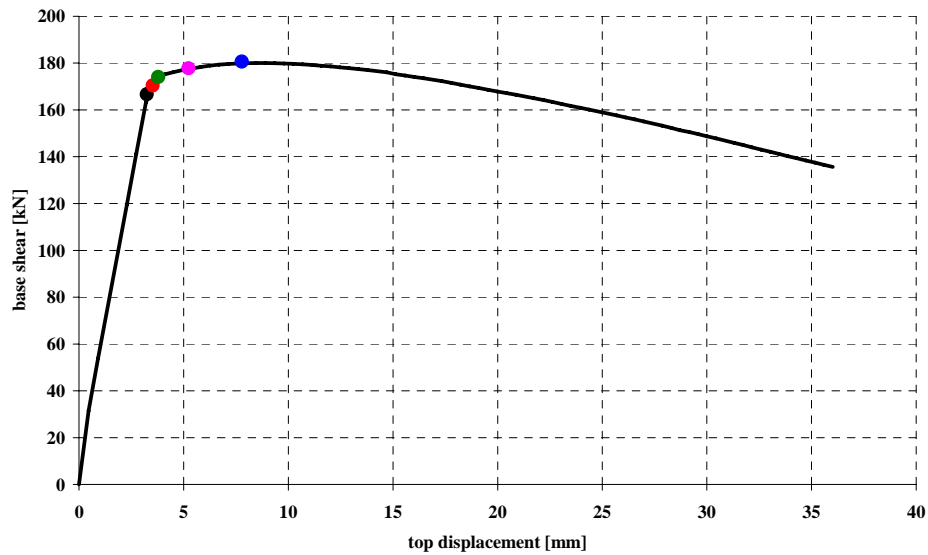


Figure 6.18: localization of plastic hinges on the capacity curve of the infilled portal with triple strut model

	F_{max} [kN]	K [kN/m]
<i>triple strut</i>	178.2	14950
<i>single strut</i>	181.2	17038

Table 6.4: bare and infilled portal: maximum horizontal load and elastic stiffness

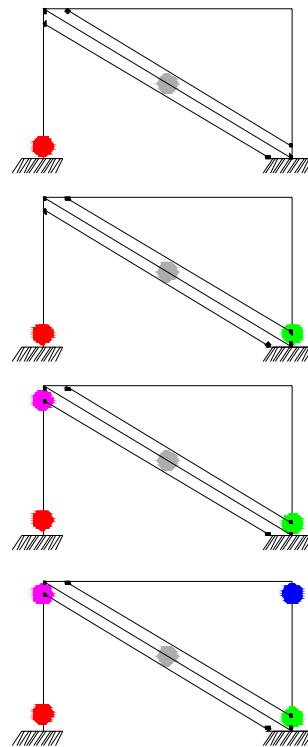


Figure 6.19: infilled portal with triple strut model, localisation of plastic hinges

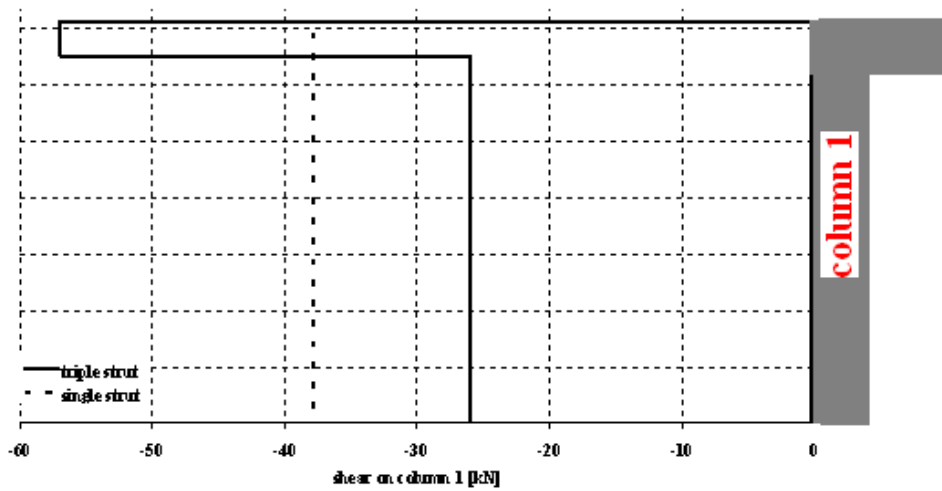


Figure 6.20: shear acting on column 1

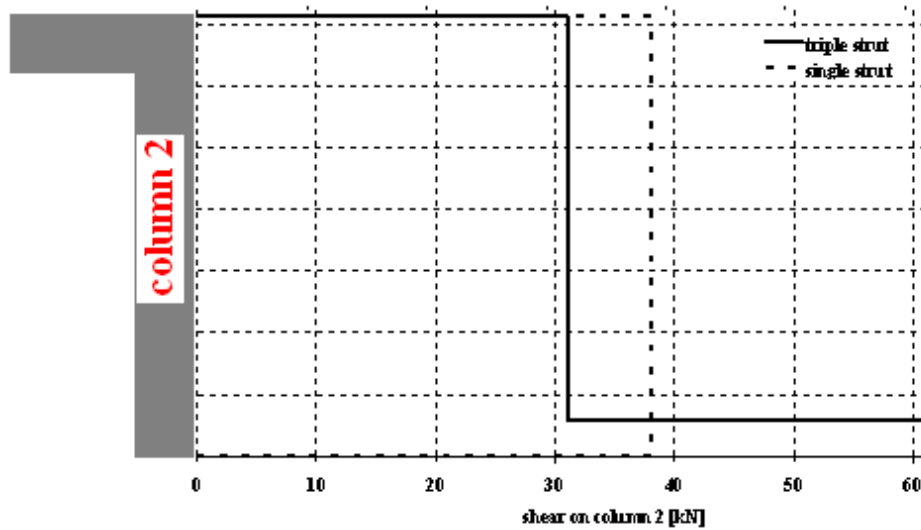


Figure 6.21: shear acting on column 2

7. Experimental tests on portals

7.1 Introduction

On the prototype portal described in Chapter 4, cyclic tests (in displacement control) have been performed until structural collapse. Three tests have been performed: the first on a bare portal (F_{nl}) and the other two on portals, identical to the previous one, both infilled with half-full bricks and mortar type 2 (F_{tl} , F_{t2}).

The three reinforced concrete portal used have been built with the same materials and they all have the same geometry.

The experimental tests performed and the results achieved are described in this chapter; the experimental results will be compared with the numerical analyses already described in detail in Chapter 6.

It is important to point out that for the portal F_{tl} partial results are provided as some data has been lost due to technical problems during execution of the experiment.

7.2 Experimental equipment

The prototype portal have been built in a 1:2 scale ratio and are fitted with some special details designed with the specific purpose of subjecting them to experimental tests in order to assess their reaction to horizontal stress.

These special details are: a basement, two metal plates on the columns top (where the gravity load has been applied) and a hole passing through the centre of the beam, where the structure has been connected trough a linking profile to the horizontal load actuator (in the following called jack M_h).

The experimental apparatus set up for execution of the cyclic tests consists of the following elements:

- hydraulic jack for horizontal load (M_h);
- hydraulic jack for gravity load (M_v);
- displacement transducers;
- loading cell;
- a system blocking vertical translation of the portal;
- a system blocking horizontal translation of the portal;
- a system to distribute the gravity load on columns top;

- a linking system between portal frame and jack M_h .

Figures 7.1 and 7.2 illustrate the test system developed and an image of the portal F_{nl} set up.

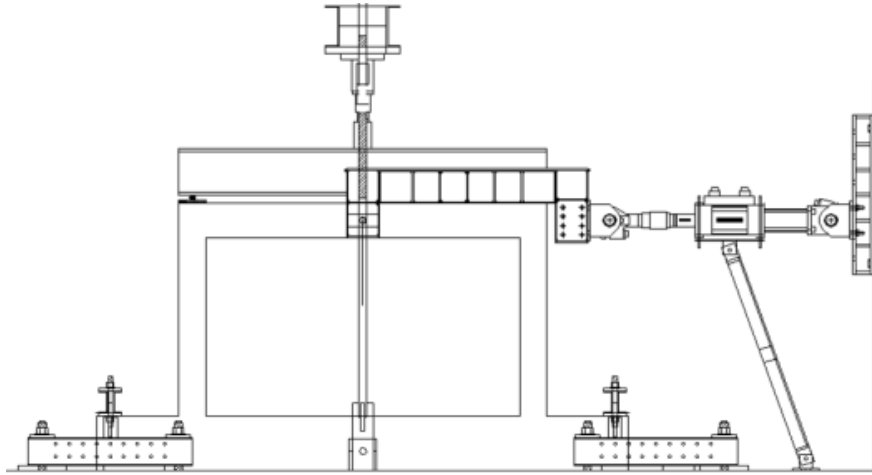


Figure 7.1: layout of the test system developed



Figure 7.2: the test system set-up on the portal F_{nl}

The hydraulic jack M_h , produced by MTS, can develop a maximum load of 1500 kN both in compression and traction, it has a maximum excursion of 500 mm and is controlled through a specific software.

As illustrated in Figure 7.3, the jack has been connected through a spherical articulation to a metal plate bolted to a contrasting wall.

The jack M_h has been connected to the portal using a linking element made of UPN220 profiles reinforced with metal plates. This element consists of two identical elements of “upside down U” shape, connected to the portal by a metal bar that crosses the hole of the beam and on the opposite end, through a profile HEB 220, on the edge of the jack M_h . With the objective of keeping the jack perfectly horizontal a metal strut fixed to the floor and to the jack itself was installed during the experimental tests.

Cyclic tests on the portal have been carried out with a gravity load of 159 kN acting on each node. In order to do so a steel beam fitted with two supports in correspondence with the centre of the column, has been positioned (Figure 7.4). In order to obtain a load of 159 kN on each column a vertical load of 318 kN was applied on the steel beam using a hydraulic jack M_v contrasted by a steel structure; a loading cell was positioned in between the hydraulic jack and the metal beam, allowing for control of the vertical loading during the experimental tests.



Figure 7.3: details of the jack M_h installed on the contrast wall (top) and on the portal (bottom)



Figure 7.4: structure designed to apply the gravity load on columns

In order to keep the portal fixed to the ground, and prevent any displacement of the structure during the experimental tests, a fixing systems have been realized (Figure 7.5).



Figure 7.5: basement fixing system

The portal tested have been instrumented with the objective to acquire every possible information useful for the structural analysis.

The portal F_{nl} , as illustrated in Figure 7.6, was fitted with the following instruments:

- 12 displacement transducers (stroke $\pm 12,5 \text{ mm}$) positioned on columns (transducer number: 2, 4, 6, 8, 16, 18, 20, 22) and on beams (transducer number: 25, 26, 29, 30). The instrumentation allowed for measuring strain and rotation of the sections of beam and columns in the plastic hinge areas;

- 12 displacement transducers (stroke $\pm 25,0 \text{ mm}$) positioned on the columns (transducer number: 1, 3, 5, 7, 17, 19, 21, 23) and on the beam (transducer number: 24, 27, 28, 31);
- 2 displacement transducers with stroke of $\pm 200,0 \text{ mm}$ (transducer number: 9, 10) and 3 with a stroke of $\pm 100,0 \text{ mm}$ (transducers 11, 12, 13), positioned between a column and a metal structure firmly connected to the basement. The instrumentation has allowed to control the horizontal displacement of the columns' sections;
- 1 transducer (stroke $\pm 12,5 \text{ mm}$) positioned between the edge of the jack and the portal itself (transducer number: 14). The instrument allows for measuring the relative displacement due to strains of the linking elements or imperfections
- 1 transducer (stroke $\pm 200,0 \text{ mm}$) applied on the jack M_h (transducer number: 15). The instrument allows to control the actual excursion of the piston using an external instrument.

On the infilled portal F_{t1} and F_{t2} , as illustrated in Figures 7.6 and 7.7, the following additional transducers have been installed, apart from the ones already positioned on the portal F_{n1} :

- 6 displacement transducers (stroke $\pm 25,0 \text{ mm}$) positioned on the interface between the wall and the columns (transducer number: 32, 34, 35, 36, 37, 38);
- 1 displacement transducer (stroke $\pm 25,0 \text{ mm}$) positioned on the interface between the wall and the centre of the beam (transducer number: 33);
- 8 transducers positioned along the two diagonal lines of the panel: 4 with a stroke of $\pm 25,0 \text{ mm}$ (transducer number: 39, 42, 43, 46) and 4 with a stroke of $\pm 50,0 \text{ mm}$ (transducer number: 40, 41, 44, 45);
- 2 transducers (stroke $\pm 100,0 \text{ mm}$) among the nodes of the portal frame, along the two diagonal (transducer number: 47, 48).

All the transducers fitted with rings with a spherical hinge, have been connected with bars fixed to the structure.

The control system of the jack M_h has, in an independent manner, allowed for registration of both the displacements imposed and the corresponding loads with a acquisition frequency of 0.1 Hz ; the data acquired in this way allows to find out, at any time of acquisition, of the horizontal load

applied. The displacement imposed by the jack corresponds to the effective excursion of the piston but does not coincide with the real horizontal displacement of the portal; in order to determine it reference is made to the measurements of the transducers fitted on the portal. Having acquired load and displacements with two different systems has been necessary to synchronise, once the test has been completed, all of the registered data. This operation has been possible through a comparison of the registrations achieved by the jack with those of the transducers: in particular, jack's excursion data controlled with the jack monitoring system have been synchronised with those of the transducer number 15 fitted on it and controlled by the data acquisition system.

The displacement history imposed during the cyclic tests has the following characteristics:

- magnitude of the first cycle imposed 1 mm ($\pm 0,5\text{ mm}$);
- 3 cycles for each step of magnitude;
- magnitude increases of $\pm 0.5\text{ mm}$ up to achievement of the maximum strength and subsequent increases of $\pm 1,0\text{ mm}$;
- cycles with a constant frequency of $0,05\text{ Hz}$.

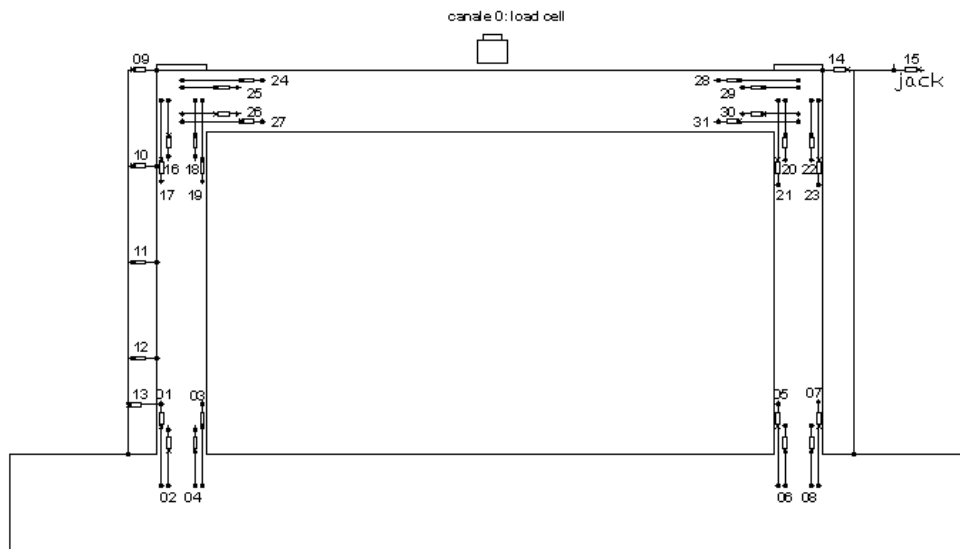


Figure 7.6: instrumentation of the bare portal

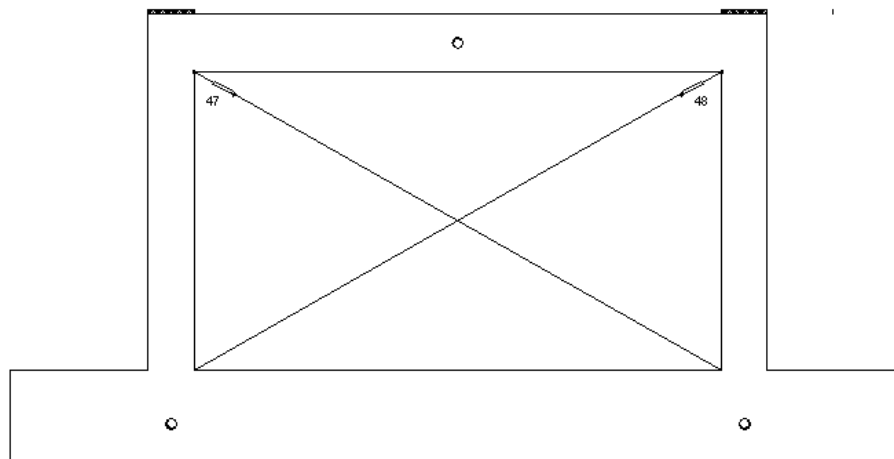
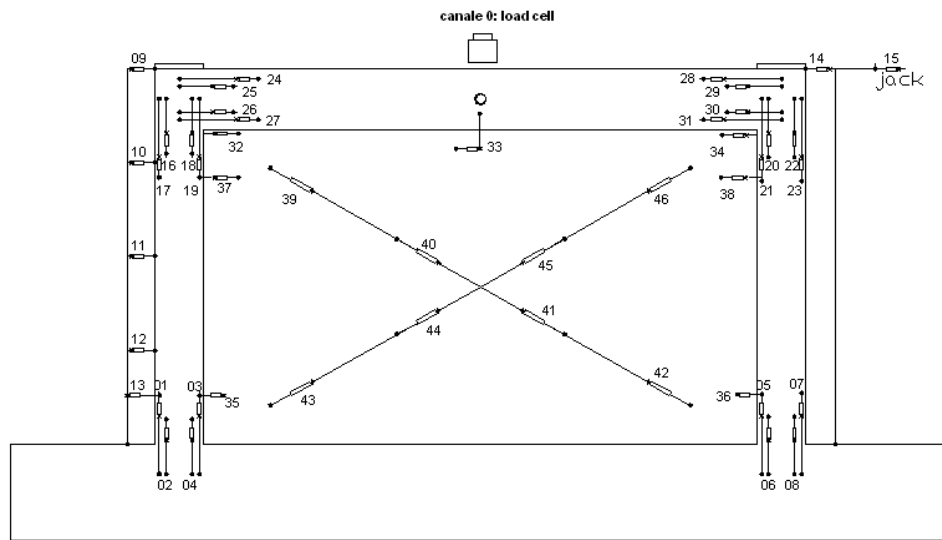


Figure 7.7: instrumentation of the infilled portal, side 1 and side 2.



Figure 7.8: set-up of the experimental test on the bare portal



Figure 7.9: the bare portal ready to be tested

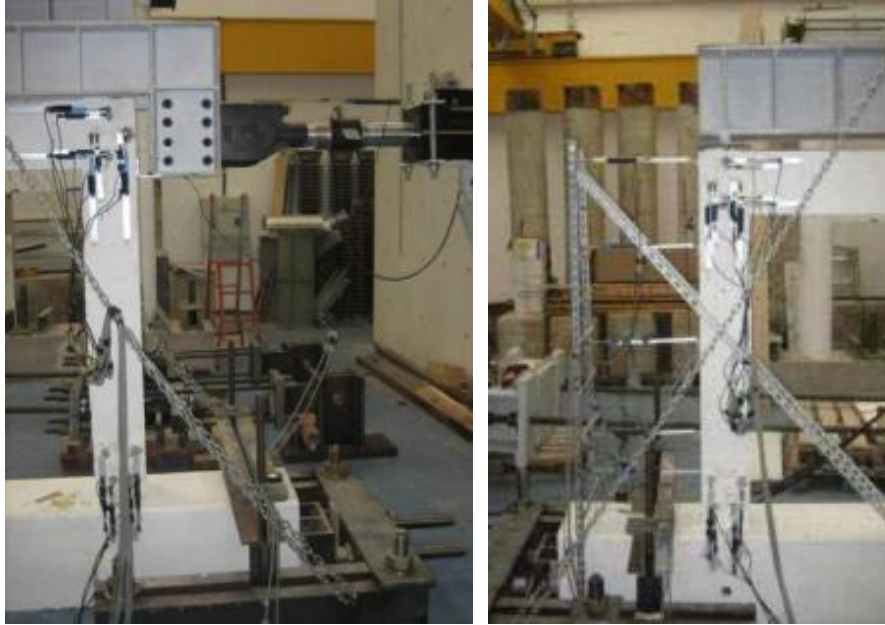


Figure 7.10: portal instrumentation's details



Figure 7.11: instrumentation of the infilled portal, side 1



Figure 7.12: instrumentation of the infilled portal, side 2



Figure 7.13: loading cell inserted under the hydraulic jack

During execution of each test, the thrust of the jack, at regular intervals, have been systematically suspended. This way it was possible to identify the developing of cracks on concrete and masonry. The cracks marking operations has been performed for both directions of deformation of the same cycle. The following paragraphs describe the observations made during execution of the experiments and the most interesting results. Subsequently the numerical models and experimental results will be compared.

7.3 Experimental tests on the bare portal F_{n1}

As this was the first of the experimental tests performed on the portal samples, some cyclic tests in elastic range leading up the final test allowing to control of all the equipment set up.

On the basis of the indications of the numerical models developed, the following characteristics were expected:

$$\begin{array}{ll} F_{max,n} & 77,5 \text{ kN} \\ K_n & 11924 \text{ kN/m} \end{array}$$

where:

$$\begin{array}{ll} F_{max,n} & \text{maximum horizontal load sustained by the bare portal} \\ & \text{model;} \\ K_n & \text{stiffness of the bare portal model} \end{array}$$

It was immediately observed that the initial cracks, to the contrary of indications provided, were found on the beam: it was subsequently found that this depended on the methods with which the thrust had been applied to the portal. In reality, as the jack was connected to the portal trough the hole inside the beam, cracks were found on it due to traction on the half part of the beam that was alternatively taut. For this reason part of the cracks on the beam should not be considered relevant for the experimental aims.

The first plastic hinges were developed at the base of the columns in correspondence with an applied top displacement of 4.33 mm, corresponding to an *interstorey drift* of 0.17% measured with the transducer 9 (Figure 7.9); it is important to point out that during this thesis, unless specifically declared, reference is made to the transducer 9 in order to establish horizontal displacement at the portal top.

The following figures illustrate the sequence of damages registered together with an increase in the displacement imposed. As the

deformation increased, the cracks on the base of the columns became more relevant and they also appeared in correspondence with the upper end of the columns for a top displacement of 8.63 mm corresponding to an *interstorey drift* of 0.34% .

At this stage traction cracks were very clear along the beam at a regular distance of approximately 220 mm (stress transferring length). Once a top displacement exceeding 15 mm have been achieved (*interstorey drift* of 0.6%) the lower sections of the columns were very much compromised and the concrete cover started to be expelled from the compressed reinforcement.

Once a displacements of approximately 30 mm was achieved, the structure maintained a plastic behaviour (increasing displacement under constant load) up to the maximum displacement impressed of 40 mm .

When the test was interrupted, both the extremities of the columns were all extremely damaged; no relevant mechanisms were highlighted on the beam.

The images illustrate how also in the upper sections of the columns the concrete cover has also been expelled on the internal side of the portal. In the bottom sections, in correspondence with the overlapping with the basement rebar and symmetrically on two sides of each column, bars buckled and the associated concrete cover have been spalled (Figure 7.14,7.15)

Images in Figure 7.15 also refer to the condition of the columns upper ends, at the end of the test, and highlight a high level of degradation as well as longitudinal bars buckling.



Figure 7.14: portal F_{n1} , damage to the base of the columns (top displacement of 30 mm)



Figure 7.15: portal F_{n1} , damage to the top of the columns (collapse)

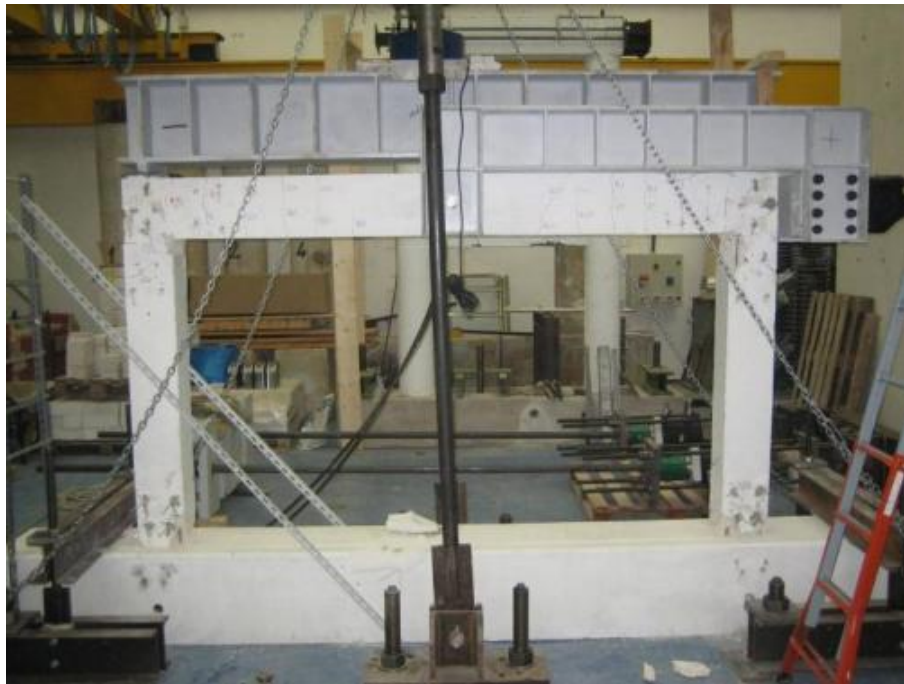


Figure 7.16: portal F_{n1} , cracks map

In the following the experimental results achieved are illustrated in terms of top displacement and the load imposed by the jack M_h .

As we can see from a comparison between Figure 7.18 and Figure 7.19, the diagram related to the history of *load–displacement* determined directly from the jack is corrupted by the effects of strains and imperfections of the linking system between the jack and the portal. The diagram in Figure 7.19 has been elaborated by synchronising the data acquired by the jack control system with that acquired from the transducers installed: this has been achieved by using the transducer positioned on the jack as a reference (for each cycle the maximum displacement registered from transducer 15 must correspond with the maximum extension of the jack) and the transducer 9 positioned in correspondence with the top of one column, as an indicator of real displacement of the portal.

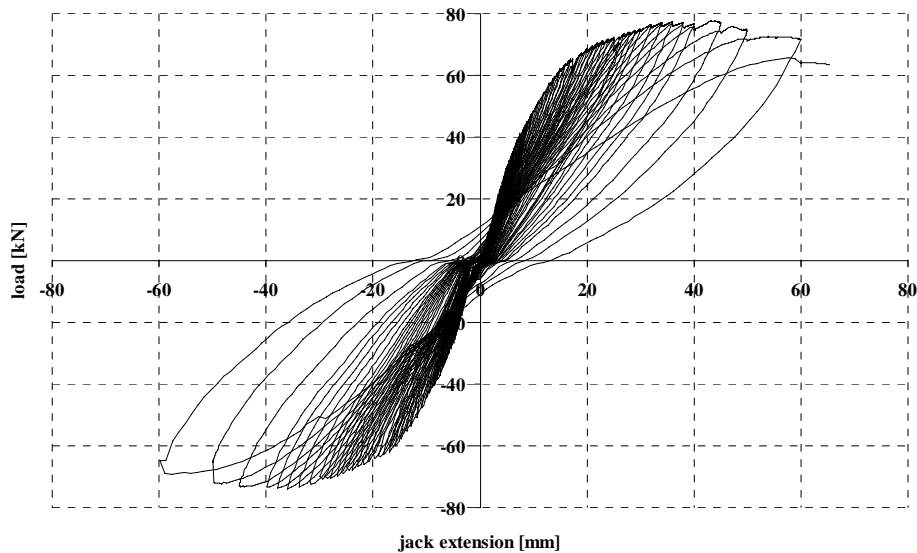


Figure 7.17: portal F_{nl} , excursion of the jack M_h – load applied by the jack M_h

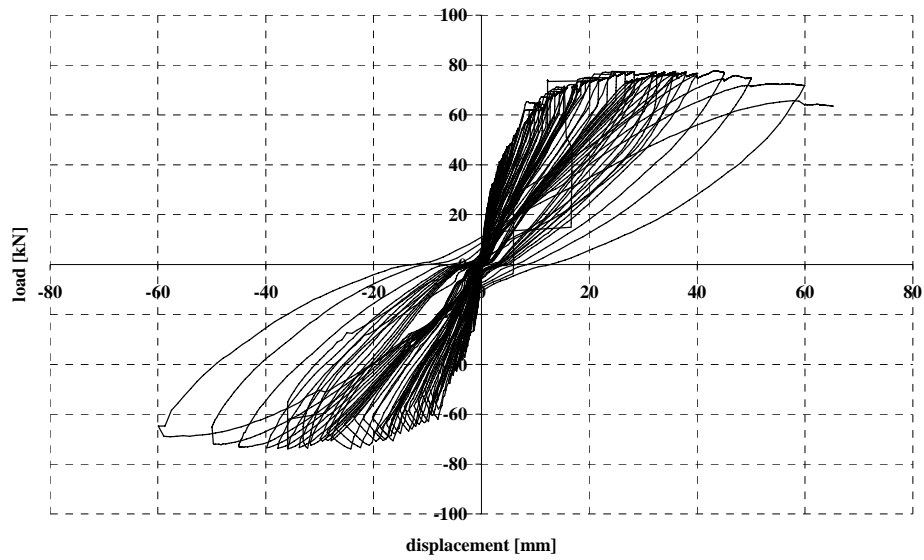


Figure 7.18: portal F_{nl} , top displacement–horizontal load

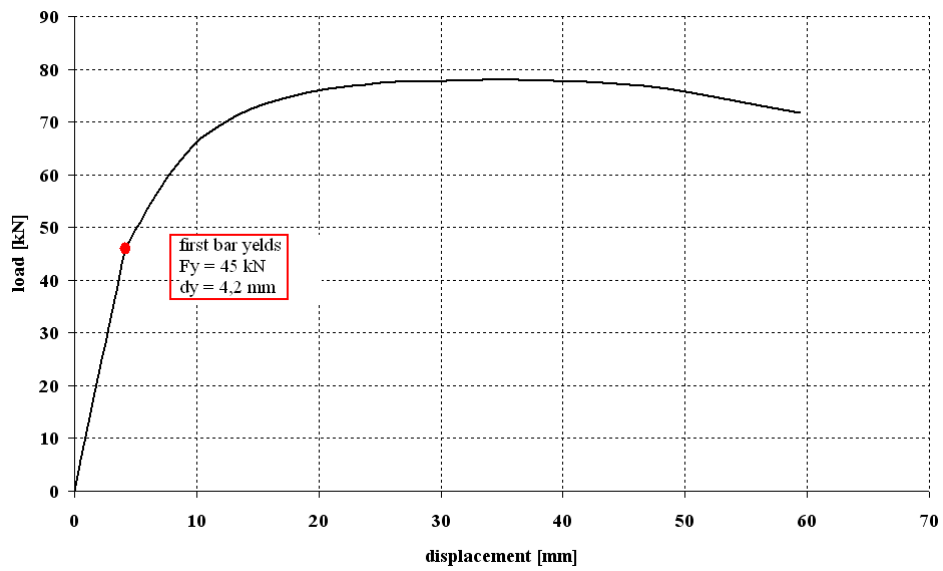


Figure 7.19: portal F_{nl} , envelope of the test performed

The parameters estimated by the experimental tests are illustrated below:

$K_{1,n1}$	12300	kN/m
$K_{2,n1}$	2230	kN/m
$F_{max,n1}$	77.3	kN
$F_{y,n1}$	45.0	kN
$\delta_{y,n1}$	4.2	mm
$\delta_{u,n1}$	40	mm

with:

$K_{1,n1}$	stiffness of the portal F_{n1} in an elastic range
$K_{2,n1}$	post-elastic stiffness of the portal F_{n1}
$F_{max,n1}$	maximum horizontal load supported by the portal F_{n1}
$F_{y,n1}$	horizontal load to yielding of the portal F_{n1}
$\delta_{y,n1}$	horizontal displacement to yielding of the portal F_{n1}
$\delta_{u,n1}$	horizontal displacement upon collapsing of the portal F_{n1}

In Figure 7.20 and 7.21 is presented the curvature achieved from the column's extremity sections during the test.

From a comparison between Figure 7.20 and 7.21 can be observed that the first plastic hinge rises at the bottom of the column, for a larger horizontal load also the sections at the upper side enter into the plastic field: the main parameters measured are summarised below:

$F_{y,n1}$	45.0	kN
$\theta_{yinf,n1}$	0.00538	1/m
$\theta_{ysup,n1}$	0.00440	1/m

with:

$\theta_{yinf,n1}$	lower section, curvature in correspondence with $F_{y,n1}$
$\theta_{ysup,n1}$	upper section, curvature in correspondence with $F_{y,n1}$

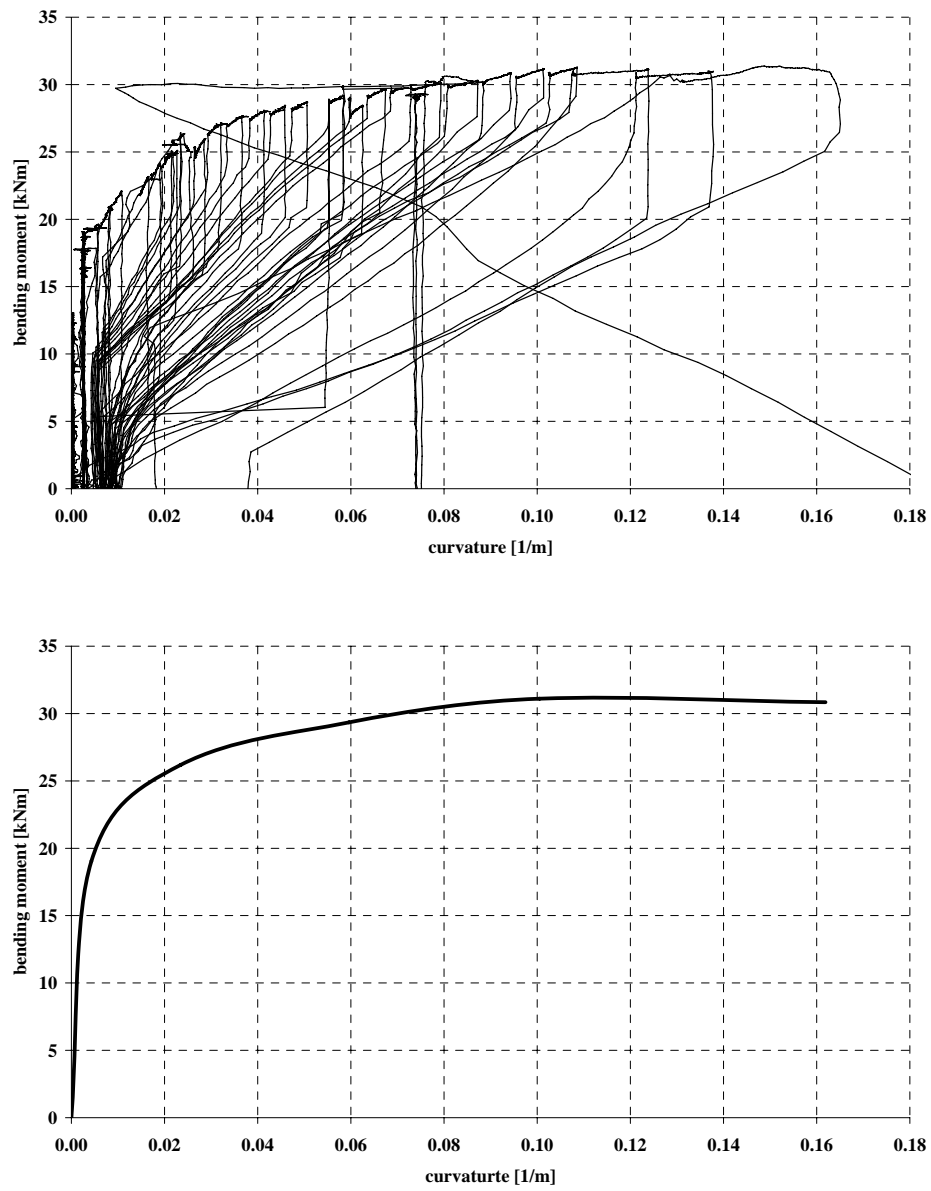


Figure 7.20: column lower section, curvature-moment

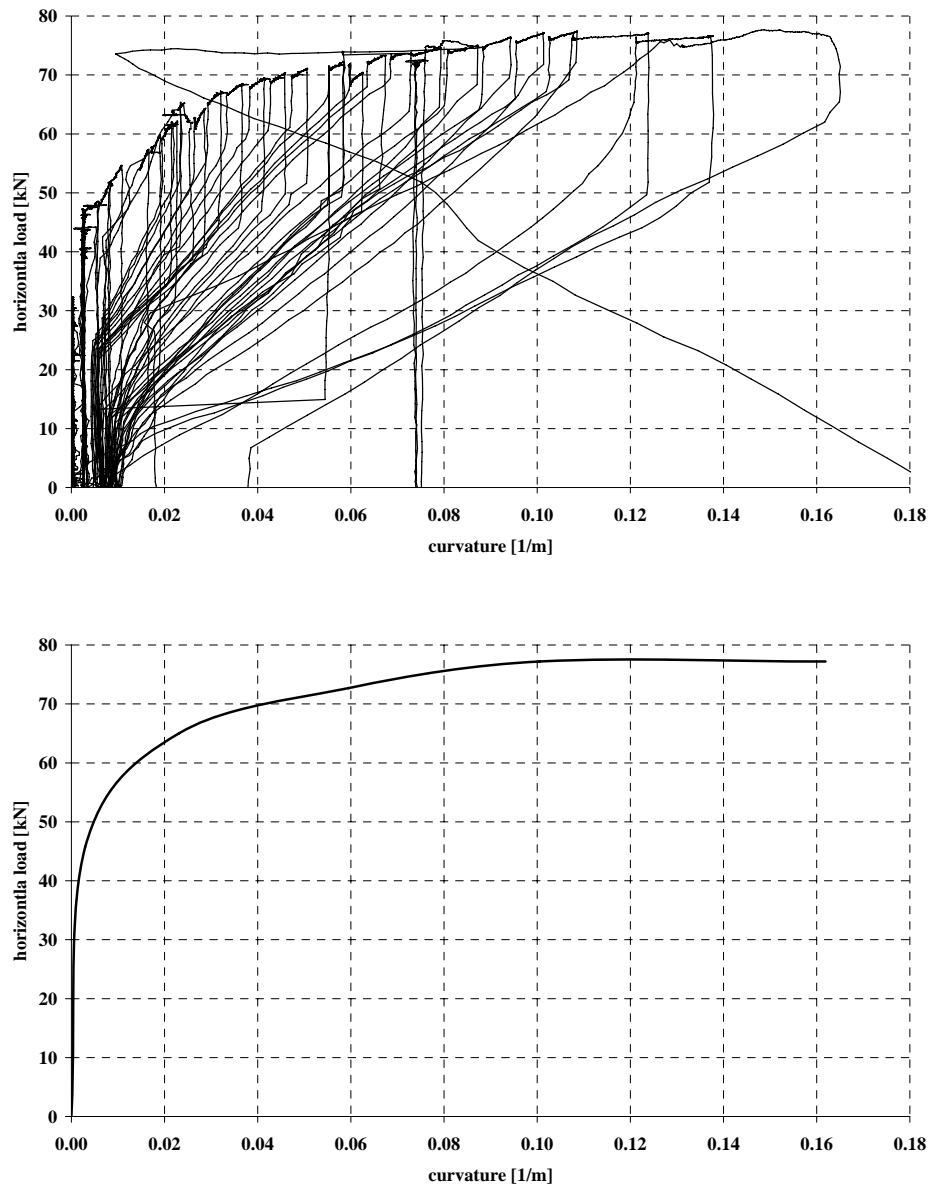


Figure 7.21: column lower section, curvature-horizontal load

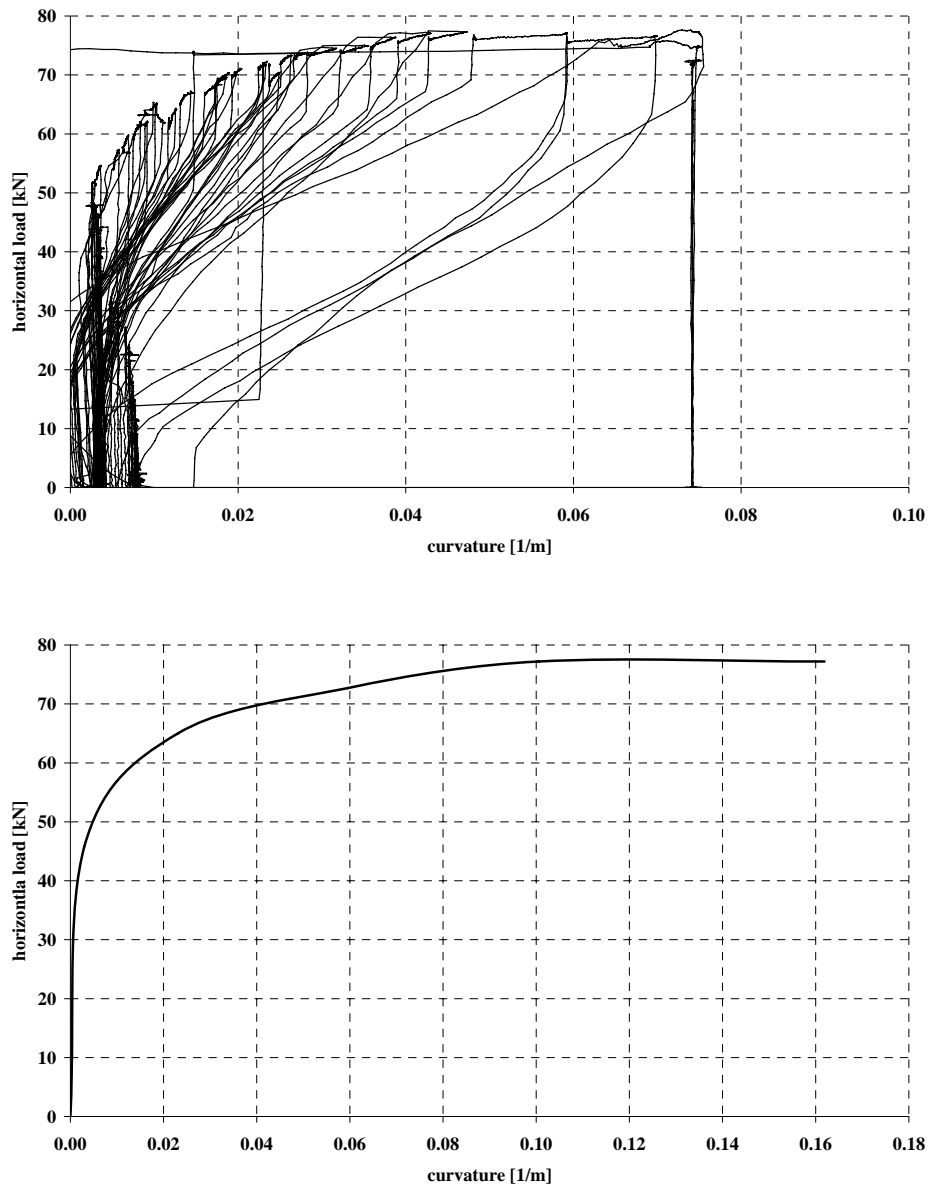


Figure 7.22: column upper section, curvature-horizontal load

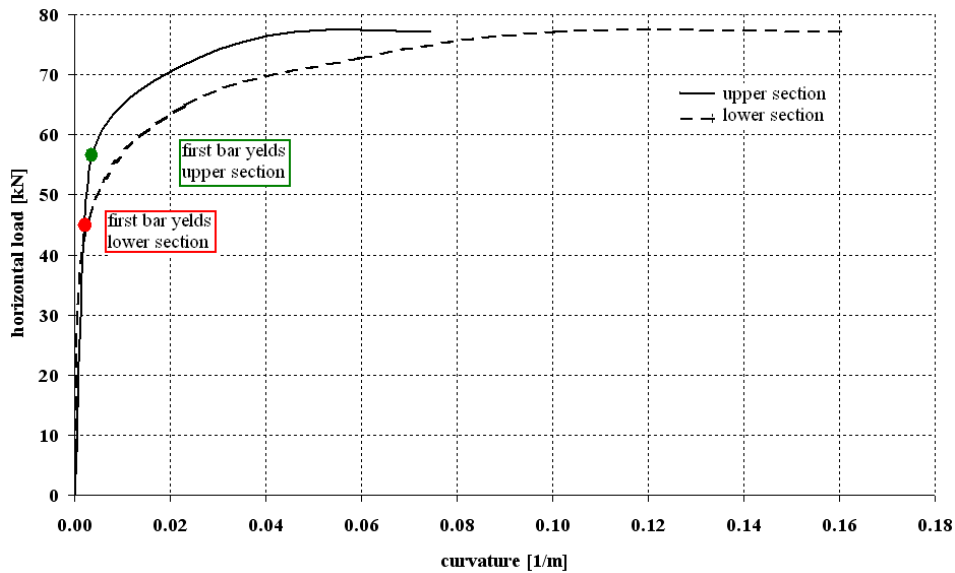


Figure 7.23: column sections, curvature-horizontal load

7.4 Experimental tests on the infilled portal F_{t1} and F_{t2}

As previously performed on the bare portal, cyclic tests have been performed on two portals, both filled with half-full bricks and type 2 mortar.

The objectives of the test were to verify correspondence between the modelling performed and the experimental results and also to investigate the efficiency of the strut models discussed in the previous chapters: direct observation of the tests and comparison with the one performed on the bare portal has allowed for an empirical determination on how the infill affects structural response.

7.4.1 Experimental test on the portal F_{t1}

As identified for the portal F_{n1} the first cracks at the bottom of the columns have appeared in correspondence with a horizontal displacement of approximately 4 mm, corresponding to an *interstorey drift* of 0,16%.

As the top displacement increases the cracks at the bottom of the columns, decisively smaller than the ones found on the bare portal F_{n1} at the same deformation level, have extended along the column up to approximately half of its height; the cracks, existing only on the concrete surface, have not been related with any relevant plastic mechanism.

With an increase in the magnitude of the cycles, detachment of the infill panel from the surfaces of the columns has also appeared and a resistant mechanism of the wall, as a diagonal compressed strut, has become evident.

The dimension of the contact area between the wall and the column has been measured progressively and a value of approximately 250 mm has been registered (in correspondence with the strut completely developed and the masonry still integral), in accordance with the values obtained from the *Mainstone* formulation previously adopted to determine of the contact surface and consequently to calibrate of the *single strut* model.

Having achieved a top displacement of 10 mm, the cracks on the wall have become very important, and apart from the cracks diffused along the entire wall, consistent parts of the bricks in correspondence with the corners of the walls have started to break and fell down.

Achieved the maximum load applied, corresponding to a top displacement of 18.7 mm, many of the bricks showed a high level of damage that has been concentrated at the two higher corners of the portal.

Parallel to the typical failure due to crashing of the corners, horizontal sliding of the panel in correspondence with the third mortar layer from the top was noticed.

As soon as the contribution of the first three rows (counting from the top) of bricks lost their resistance to horizontal sliding, the load has been absorbed by the concrete columns; the first plastic hinges developed immediately after that the masonry crushed and the structure collapsed.



Figure 7.24: portal F_{tl} , superficial cracks along columns height

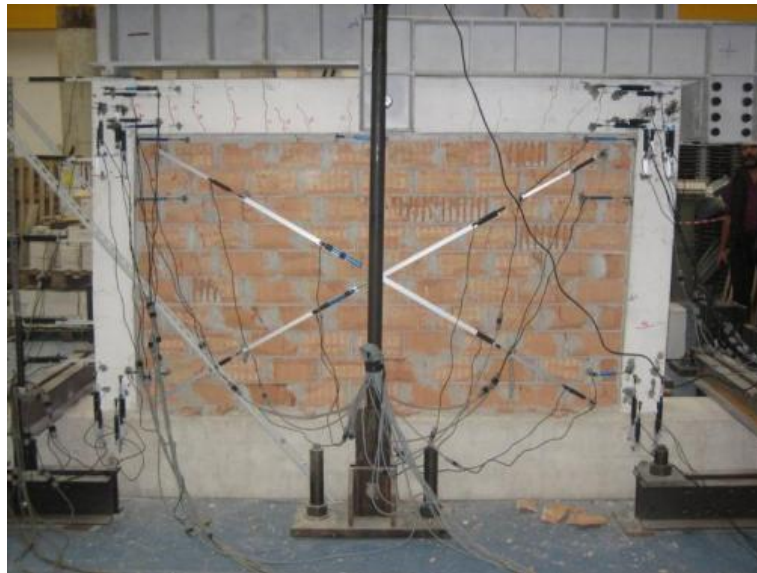


Figure 7.25: portal F_{tl} , infill damages during the experimental test (close to maximum load)

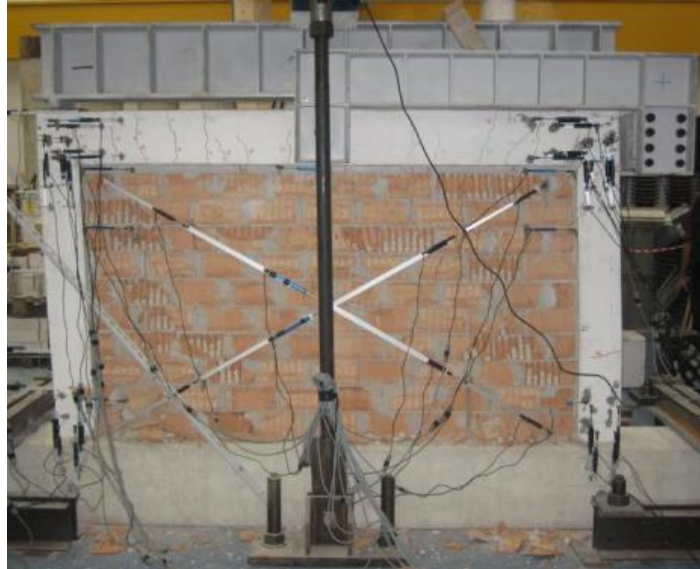


Figure 7.25: portal F_{11} , infill damages during the experimental test (in correspondence with the maximum load)



Figure 7.27: portal F_{11} , infill damages during the experimental test (after having achieved maximum load)



Figure 7.28: portal frame F_{t1} , detail of the structure following collapse

As previously mentioned, the experimental data acquired by the transducers has been lost due to technical problems; the results presented have been taken from the information acquired from the jack; the deformations of the test equipment has been calculated through a theoretical evaluation of strain of the linking system and may therefore contain some inaccuracies. For this purpose, all of the analyses described in this thesis refer to the results achieved by the test performed on the portal F_{n1} and F_{t2} of which all information has been preserved. The results are presented in accordance with the methods used for the previous tests on the portal F_{n1} .

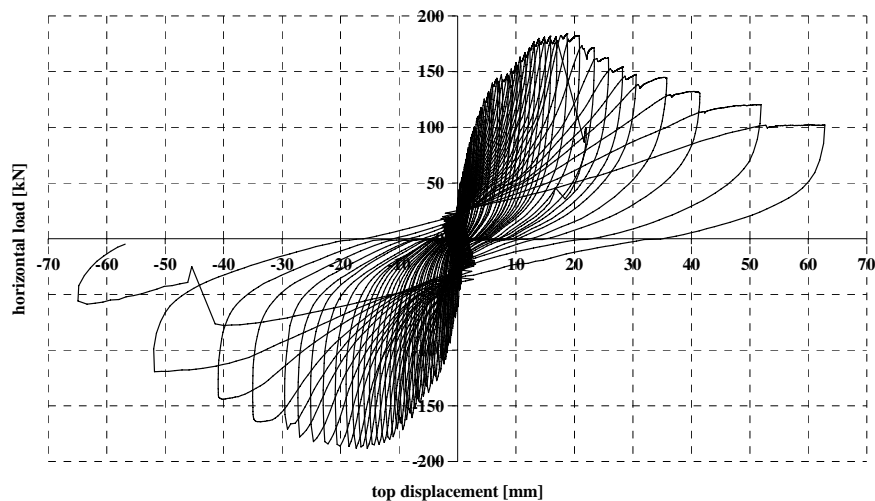


Figure 7.29: portal F_{t1} , top displacement–horizontal load

7.4.2 Experimental test on the portal F_{t2}

The results of the experimental test on the portal F_{t2} have shown a behaviour that, on a global level, leads to values of strength and stiffness that can be compared with the ones of the portal F_{t1} even though some differences have been observed while carrying out the experiment.

In this case the very first cracks on the concrete have arisen in correspondence with the upper half of the columns even though, as in the previous case, not completely extended to the entire height of the column.

The cracks in the panel have highlighted a well outlined compressed diagonal strut behaviour and, as can be noted from the images shown, also in this case a dimension of the strut of approximately 250 mm has been measured. Unlike the previous case, failure due to crashing of the bricks has been concentrated not exactly in correspondence with the corners: this may be justified by observing that the bed-joint sliding, occurred before achievement of the maximum strength of the compressed masonry, interrupted the “corner to corner” strut initially developed.

The diagonal struts, interrupted in correspondence with the sliding surface, have exercised their thrust between the lower corners of the portal and the section of the columns corresponding with the sliding surface. As soon as the compressed diagonal strut crashed, the columns collapsed in correspondence with the upper sections of the columns where the sliding bricks didn't collaborate anymore, in the same way as the portal F_{t1} did.

The following figures illustrate the trend of the curvature of the sections at the columns bottom and top related to variations of horizontal load.

By analyzing the curvature of column lower sections, as highlighted during direct observation of the experiment, has been determined how those remains within an elastic range. Unlike in the upper sections the instruments have registered important curvatures before achieving $F_{max,t2}$, subsequently the first plastic hinge arises.

As can be seen, until the wall remains integral, rotations were concentrated on the top of the columns where collapse occurred once the infill has lost resistant capacity.



Figure 7.30: portal frame F_{11} , infill damages during the experimental test (after having achieved maximum load)

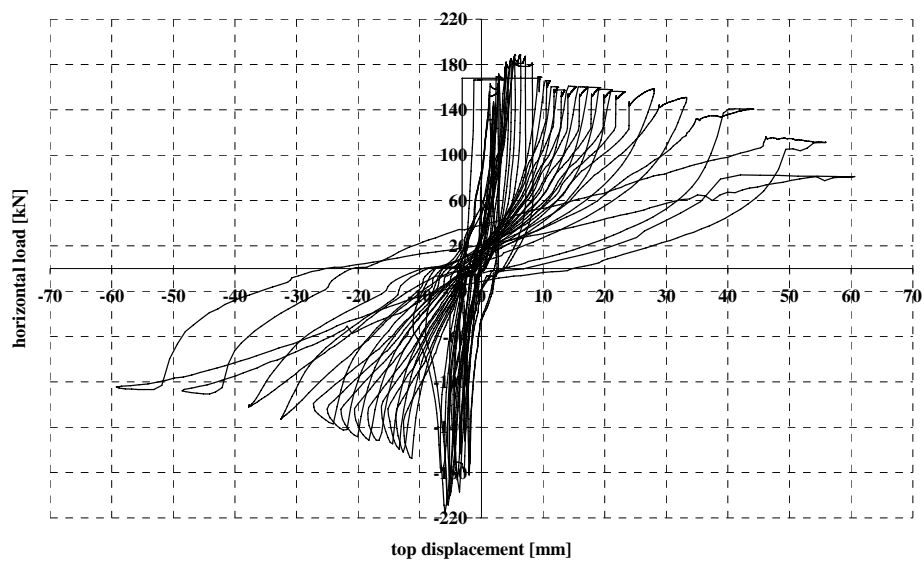


Figure 7.31: portal F_{12} , top displacement–horizontal load

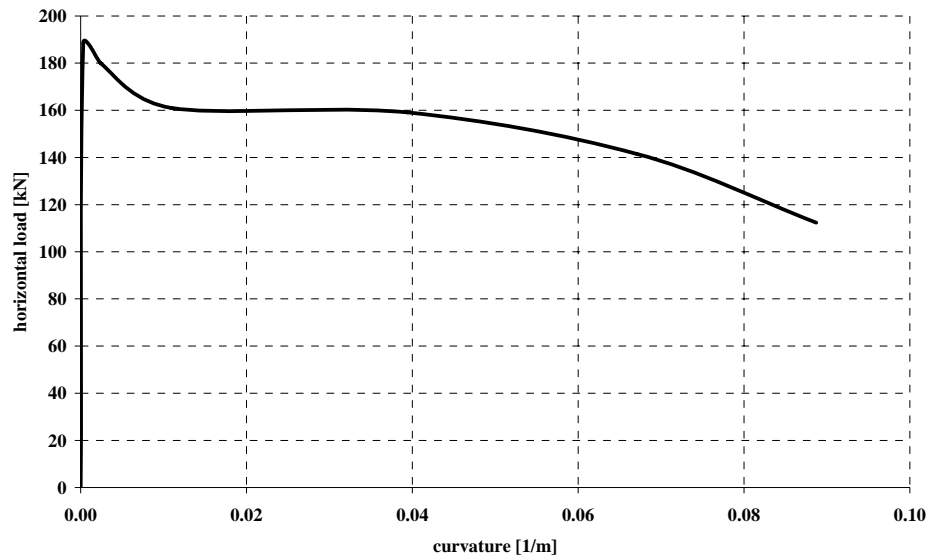


Figure 7.31: column lower section, curvature-horizontal load

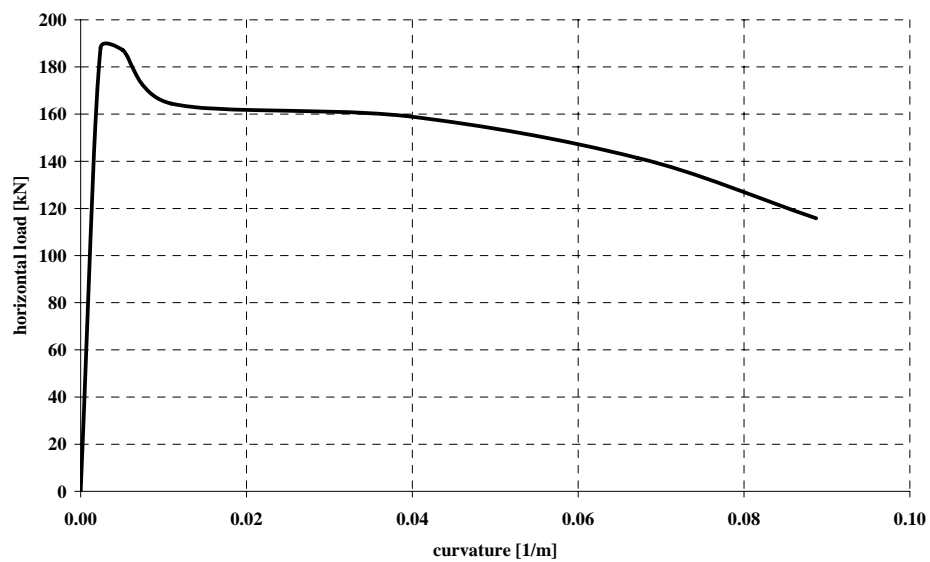


Figure 7.32: column upper section, curvature-horizontal load

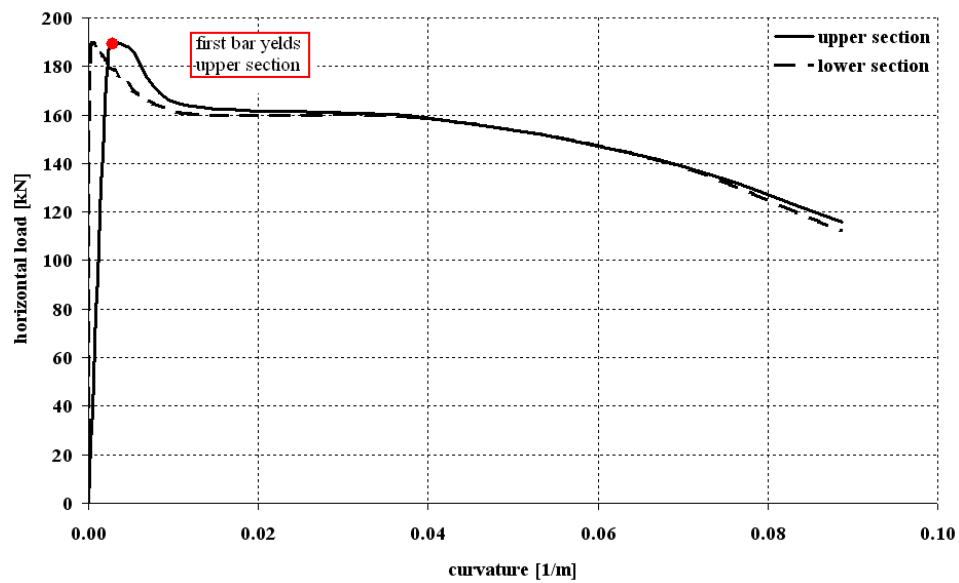


Figure 7.33: column upper and lower sections, curvature-horizontal load

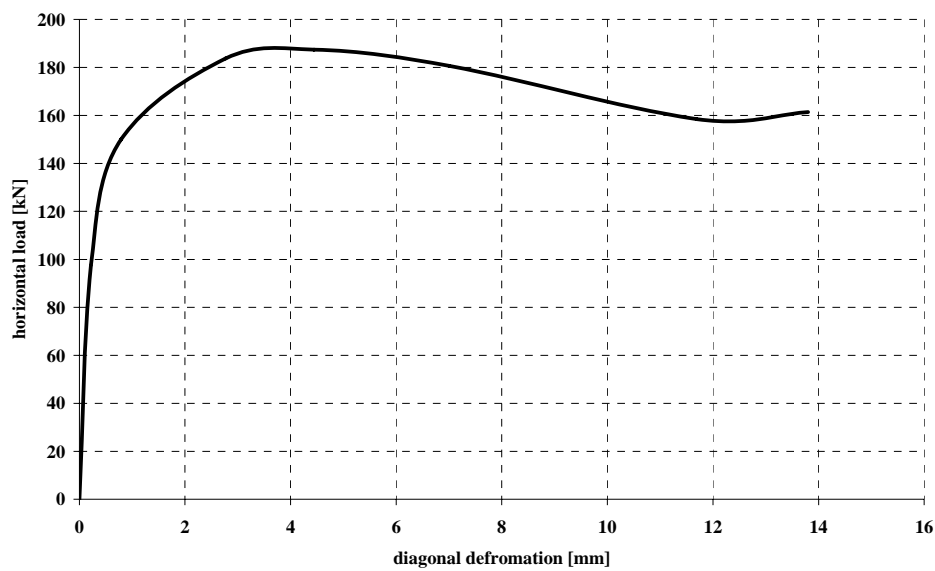


Figure 7.34: diagonal deformation, deformation-horizontal load
(transducer 41)

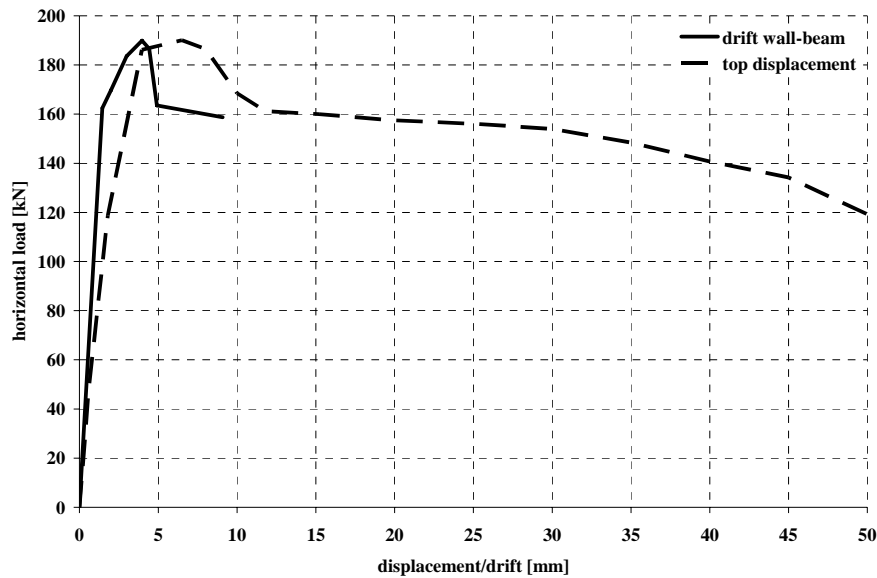


Figure 7.34: -drift between the panel and the beam-load
(transducer 33)

7.4.3 Behaviour mode observed

During the test performed on the infilled portals the following damages has been observed, in the same order as are now presented, on the infill panel and on the frame itself:

Diagonal cracking: when the tensile strain and stresses, transverse to the principal compression stresses formed across the diagonal of the infill, exceed the cracking strain of the infill panel material, diagonal cracking occurred starting from the center of the infill, as the interstorey drift increased they extended diagonally from one corner to the opposite one.

Bed-joint sliding: this behavior mode occurred in conjunction with the *corner compression* of failure. This behavior should be predicted because of the mortar beds were relatively weak compared to the adjacent masonry, the plane of weakness formed near the higer part of the infill panel.

Corner compression: as inevitable for this type of masonry, characterized by strong bricks, corner compression occurred. This is because of the high

stress concentrations at each corner of the compression diagonal. Corner crushing was located over a region limited to 2-3 bricks' layers; the damage extended into the concrete frame itself.

Shear yielding: when corner crushing occurred, the diagonal compression strut moves downward into the column and provided a large shear force at the end-region of the column. This has led to a large localized shear deformations in the columns' top.

Has widely discussed in literature the behavior modes previously described are ductile, in particular *bed-joint sliding* is associated with high level of ductility while *diagonal cracking* and *corner compression* to a moderate level of ductility (*ref. FEMA 306*).

7.5 Experimental determination of the equivalent strut

From a comparison of the results of the experimental tests performed on the bare portal and on the infilled portal, it is possible to establish geometry and characteristics to be assigned to an equivalent single strut. It is important to remember that the description provided herein has been used with the objective to calibrate the numerical model initially generated on a theoretical basis (model proposed by *Camberscuc 1996*). The experimental results achieved have been used to establish the *capacity curves* of the bare and infilled portal; subsequently by subtracting the *capacity curve* of F_{n1} from the one corresponding to F_{12} the trend of the horizontal component of the load absorbed by the infill has been defined. This procedure previously described should be considered valid if we believe that the r.c. structure offers an equivalent reaction expressed in terms of *capacity curve*, in both the two configurations (bare or infilled): Figure 7.34 represents the *capacity curves* and their arithmetical difference. During the experimental tests on the infilled portal, it has been possible to provide an empirical determination of the dimension of the contact surface, the layout of cracks developed in the wall, highlights a contact length, between wall and column, of 250 mm. Once has been determined the load absorbed by the infill and having established an empirical dimension of the contact

length, it has been possible to reconstruct an experimentally calibrated model, to be allocated to the numerical model.

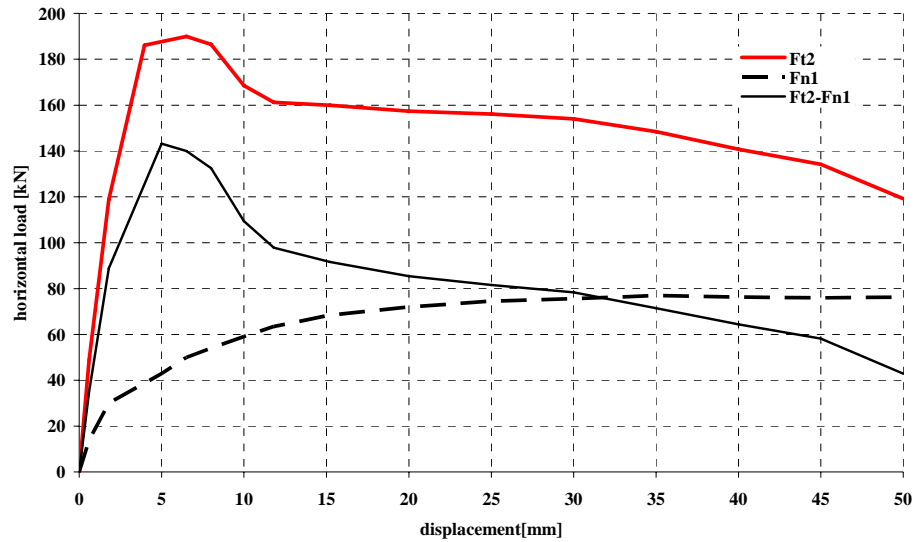


Figure 7.34: characteristics of the equivalent strut determined as the difference between the capacity curves of the portal F_{n1} and F_{t2}

Top displacement [mm]	Horizontal load [kN]	Infill condition
1.8	118.8	Cracking
3.96	186.1	Plastic range
8.0	186.5	Collapse

Strut (horizontal load component) [kN]	Strut (axial load) [kN]	Infill condition
88.8	102.2	Cracking
143.2	165.8	Plastic range
132.5	152.5	Collapse

Infill shear strength 0.67 MPa (horizontal load/shear area)		
--	--	--

Table 7.1: summary of data from test on the infilled portal F_{t2}

<i>Experitmental data</i>	<i>Dimension [mm]</i>
<i>contact surface observed</i>	250.0 mm
<i>average dimension of the strut (orthogonal to the diagonal axis)</i>	247.6 mm

Table 7.2: experitmental dimension of the strut

<i>Load-deformation curve of the theoretical strut</i>			
<i>Deformation [mm]</i>		<i>Axial load [kN]</i>	
-	0	-	0
$d_{e\theta}$	0.75	$F_{e\theta}$	60.82
$d_{w\theta}$	2.26	$F_{w\theta}$	121.64
$d_{wu\theta}$	7.63	$F_{u\theta}$	121.64
$d_{u\theta}$	40.61	$F_{residual}$	12.16

Table 7.3: load-deformation curve of the theoretical strut model

<i>Load-deformation curve of the experimental strut</i>			
<i>Deformation [mm]</i>		<i>Axial load [kN]</i>	
-	0	-	0
$d_{e\theta}$	1.680	$F_{e\theta}$	99.40
$d_{w\theta}$	4.870	$F_{w\theta}$	165.00
$d_{wu\theta}$	5.70	$F_{u\theta}$	164.30
$d_{u\theta}$	-	$F_{residual}$	-

Table 7.4: load-deformation curve of the experimental strut model

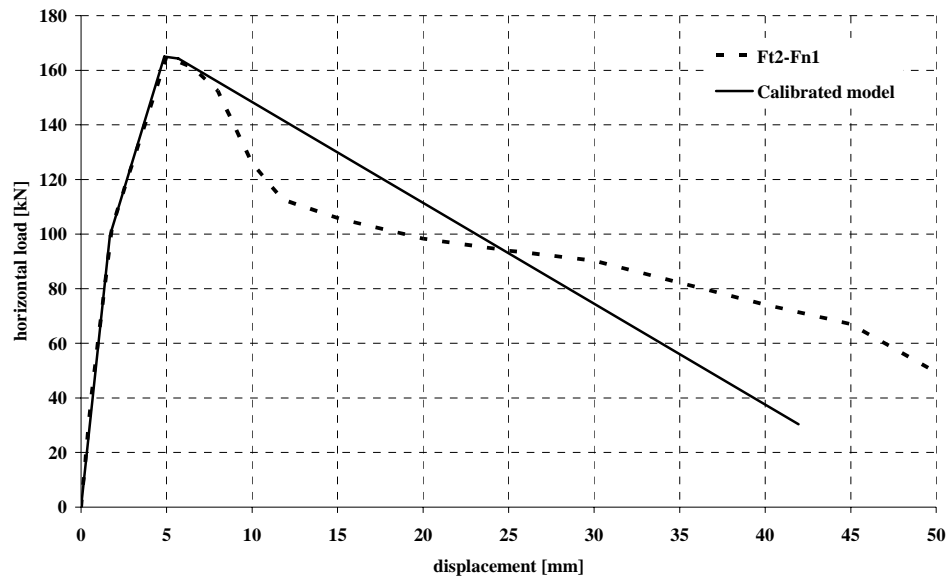


Figure 7.35: experimental results Vs calibrated model (implemented in the numerical model) of the diagonal strut, axial load –deformation

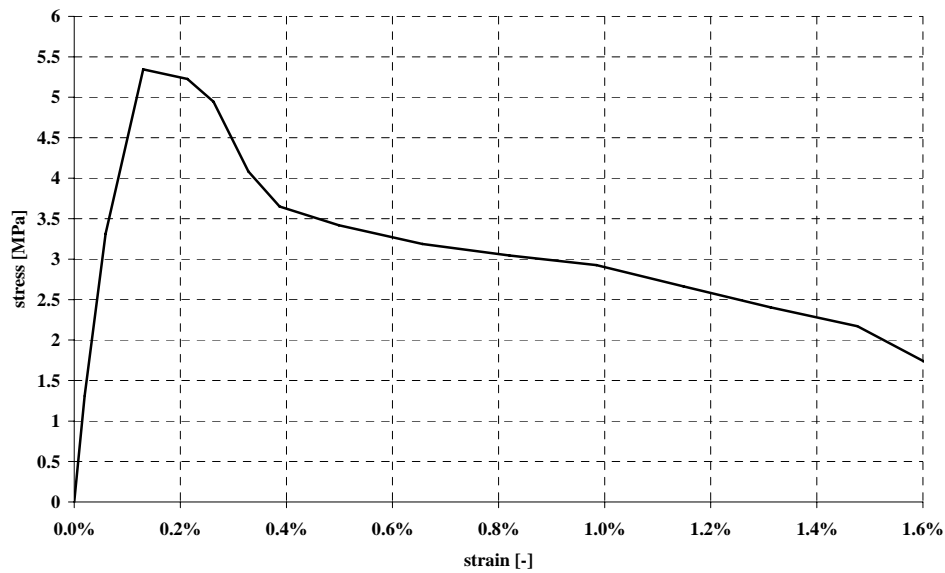


Figure 7.36: experimental stress strain relationship of the strut

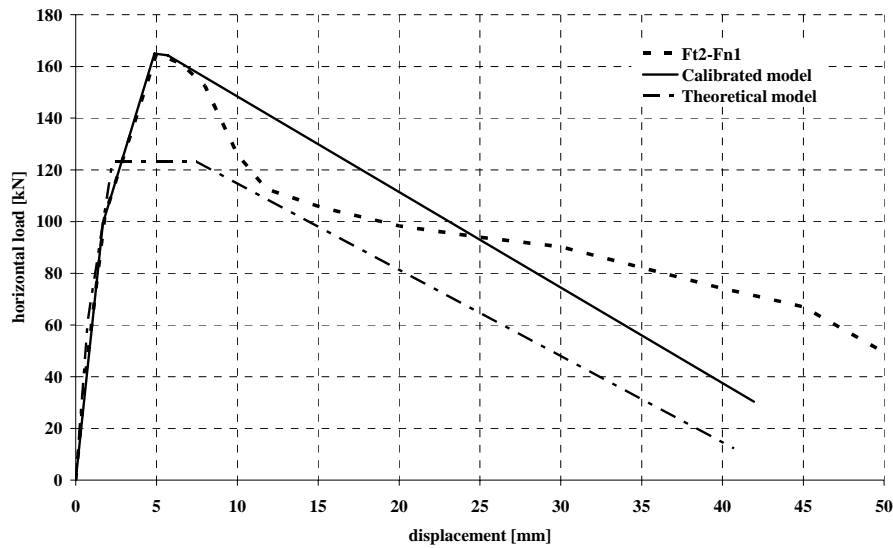


Figure 7.37: theoretical Vs calibrated models of the diagonal strut, axial load-deformation

The characteristics of the constitutive model of the masonry allocated to the struts in the global models are summarised in Table 7.5 and 7.6.

Stress-strain curve of the calibrated strut model		
ε [mm]	σ [kN]	
0.06%	3.34	Crack
0.11%	5.41	Max
0.13%	5.40	Failure

Table 7.5: stress-strain curve of the calibrated strut model

E_i	5824 MPa	Infill elastic modulus calculated on the first branch
E_c	2973 MPa	Infill cracked modulus calculated on the second branch
E_θ	4161 MPa	Infill elastic modulus of the infill (θ inclined direction) calculated on the bilinear equivalent model
K_s	47910 kN/mm	strut axial stiffness

Table 7.6: summary of parameters of the calibrated infill model

As previously mentioned, the differences found between the theoretical infill model initially assumed and the one subsequently calibrated on an experimental basis depend on two uncertainties.

The first uncertainty consists in the inability to determine the strength to be allocated to the masonry compressed with an angle of θ and confined by both the surrounding masonry (the real wall is bigger than the samples) and the frame. In reality, we can see that the strength to be allocated to the diagonal strut, considering it of a constant dimension, is equivalent to 5.4 MPa which is more or less equivalent to the compression strength parallel to the holes determined on wall samples.

The second uncertainty is the shear strength of the wall along the bed-joint; in reality sliding between bricks along bed-joints influenced the resistance of both of the portals F_{t1} and F_{t2} .

As no experimental tests have been performed on walls to determine this parameter, it has not been possible to forecast how this could have affected the results achieved. Once the tests have been completed, it is possible to observe that infill sliding generates a substantial reduction of the plastic branch that have been theoretically forecast; it is in the plastic branch that the main inaccuracy of the theoretical model can be identified. The experimental observations confirmed the theoretical prevision of the contact length. In the same way also the constitutive model hypothesised could be close to reality if an appropriate compressive strength is chosen. Consequently for this type of masonry (half-full bricks) once the dimension of the equivalent strut has been defined, it should be a good approximation to assign it a material whose strength is equivalent to the one determined through compression tests on walls along their strong direction; the results currently available are limited to just one typology of infill and therefore they do not allow for conferring to the previous statements a general value.

Furthermore, it would be useful to assess if the shear strength along bed-joint experimentally found by testing the infilled portal is coherent with what could be calculated from shear tests on wall samples.

In this case, having used only global models consisting of diagonal struts and without any additional elements that may result in the collapse of the wall due to shear, the softening branch of the model has been calibrated with the objective of catching both of the strength decay due to bed-joint sliding and the following masonry deterioration.

7.6 Comparison of the experimental and numerical results

The results of the experimental tests have been compared with the analyses performed on the numerical models already presented and discussed in the previous chapters.

This way it has been possible to validate the numerical models of both types of portal.

This process allows to confirm the feasibility of the numerical models that may represent a starting point for a new study campaign on this topic.

The following figures compare the results from numerical analyses with the experimental results achieved for the bare portal and subsequently for the infilled one.

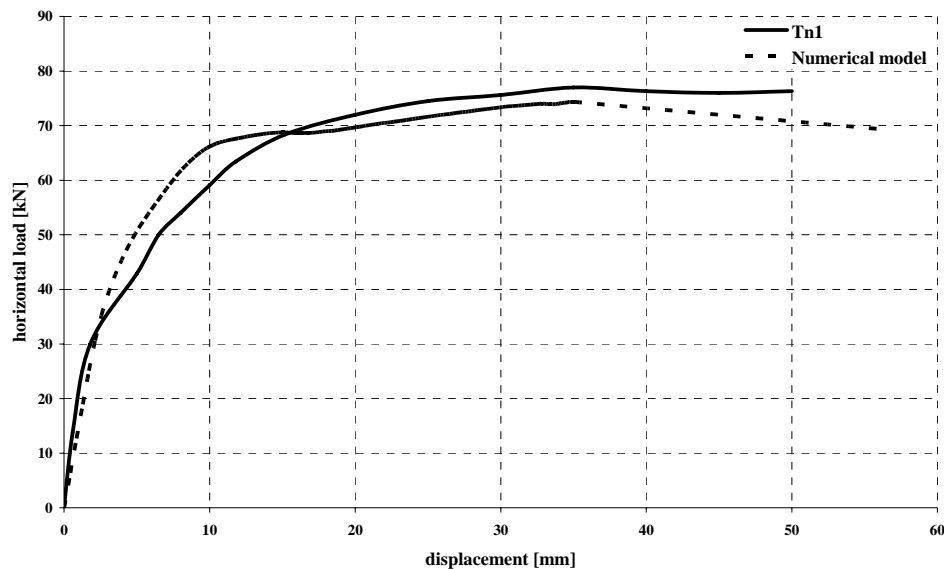


Figure 7.38: experimental and numerical capacity curves of the bare portal

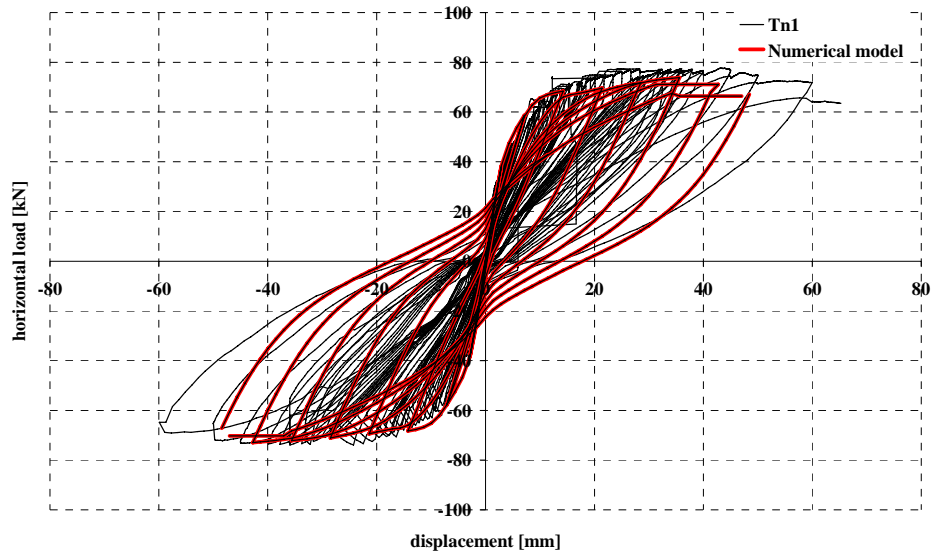


Figure 7.39: experimental and numerical cyclic analysis of the bare portal

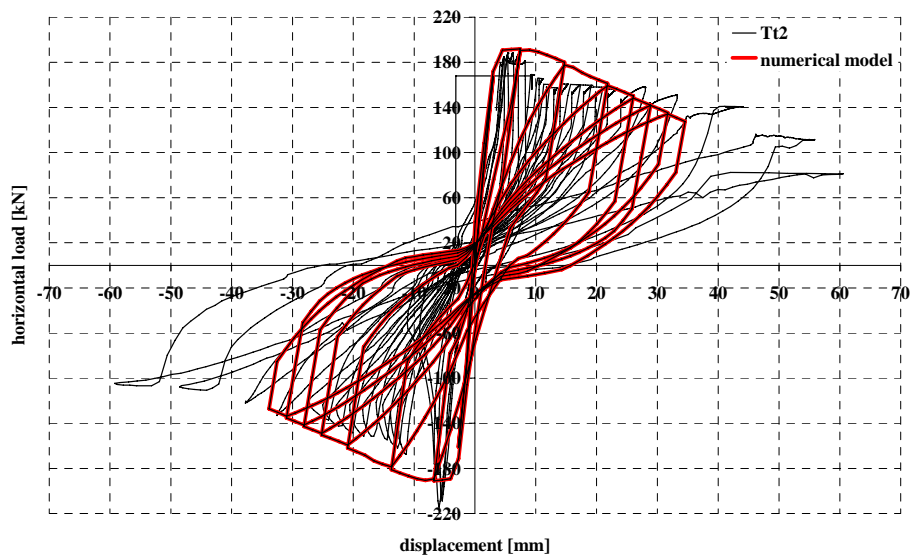


Figure 7.40: experimental and numerical cyclic analysis of the infilled portal

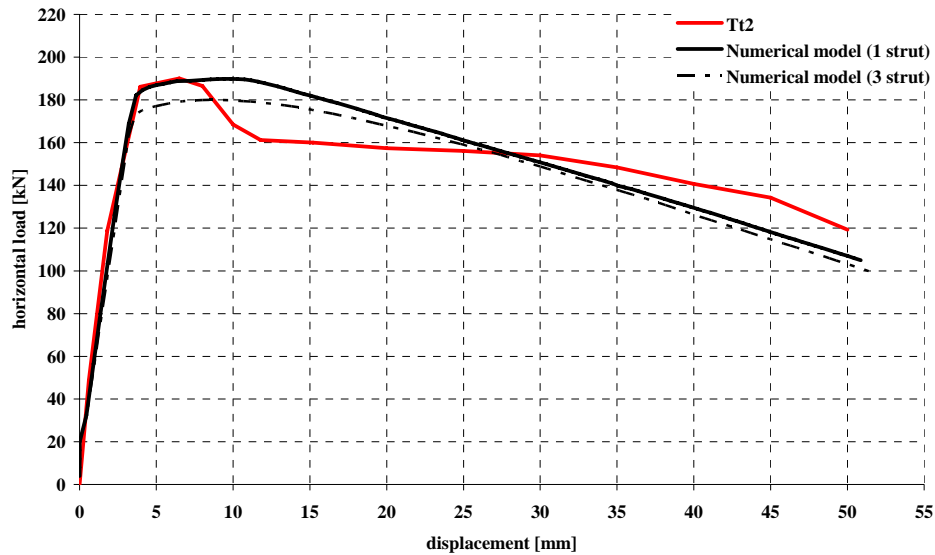


Figure 7.41: experimental and numerical capacity curves of the infilled portal

As it can be seen, the numerical model of the bare and infilled portal appears to be well calibrated, the stiffness estimated coincides with the experimental one as well as the value of maximum horizontal load. The experimental results highlight a dissymmetry, the positive load developed are slightly higher than the ones measured in the opposite thrust direction. Obviously the numerical model has perfect symmetry and a trend that moves closer to the experimental measurements corresponding to negative load values (contraction of the jack). This has been justified by observing that the portal prototype did not have an ideal geometry as well as the linking structure between the jack and the portal. The structure has therefore felt the effects of a load eccentricity: in the jack extension phase a slight strain of the compressed linking profile has increased the existing eccentricity by affecting the final result. Therefore it is correct to consider more reliable the load measured during contraction of the jack and therefore traction of the linking element. However, with regards to the activities carried out on the infilled portal, as in the case of the bare one, the experimental results as well as the numerical ones are presented.

As illustrated in Figure 7.41 both of the models performed, with the *triple strut* or with the *single strut*, generate results that are similar in terms of global structural response. Both of them catch perfectly the initial stiffness of the structure up to the peak of strength. However, it is important to point out the different maximum load even though it develops for the same displacement value. From a general assessment in terms of *capacity curve*, it would appear that the *single strut* model is better calibrated: the imprecision of the *triple strut* model in the estimation of the maximum strength derives from the hypothesis made determining the dimensions of the three struts: in fact the geometry has been defined starting from the dimension of the equivalent single strut even though the position of the three struts is different. In reality due to the different lengths of the side struts compared with the central one, they reach the maximum strength for a slightly lower displacement than the correspondent for the central one; therefore it is clear how the strength determined with the *triple strut* model is slightly lower than what can be obtained with the *single strut* model.

For further information on the analyses performed on the numerical models refer to Chapter 6.

8. Analyses results for the 1:1 scaled frames

8.1 Introduction

One of the objectives of the study carried out on scale portals is to extend the numerical model developed, experimentally tested, to various structures in a real scale with the objective of using them as numerical samples on which further studies should be carried out. This chapter presents, as a starting point for future development, the first numerical models implemented and the first analyses carried out. It is important to remember that the prototype portal used for the experimental tests have been created taking inspiration from the real scale frame now adopted. Consequently the numerical models now presented have the same geometry of the plane frame from which the prototype portal has been extracted.

The extension of the models previously described to structures in a real scale establish the starting point for a detailed analysis of the effects that the infill may have on structural response of a building with several floors and several bays. In order to do so, starting with the standard geometry of the r.c. frame, different planar configurations of the infill have been hypothesised.

The models made have therefore been compared and discussed; as far as the infill is concerned, both the *single strut* and the *triple strut* models have been adopted, as already done for the portals in the previous chapters.

8.2 Numerical models and analyses results

The hypotheses adopted to define the infill model are the same as the ones adopted for the portal, the characteristics of the global models have only changed according to the new geometry.

It is important to remember that the characteristics of geometry and materials of the structures now discussed have been described in detail in Chapter 4: the infill constitutive model adopted is the one calibrated on an experimental basis. The geometric characteristics of the *single strut* are indicated in Table 8.1 and Figure 8.1 and 8.2.

In accordance with the hypothesis of considering the same type of infill for the entire plane frame (half-full bricks and type 2 mortar), all of the elementary portals that form the frames are characterised by struts with the same geometry and constitutive model.

Infill Parameters

l_w	4800	mm	Length of the wall
h_w	2750	mm	Height of the wall
d_w	5531.95	mm	Length of the diagonal strut
θ	0.52	rad	Inclination of the strut
t_w	120	mm	Thickness of the wall (or width of the strut)
$E_{w\theta}$	4161.0	MPa	Elastic modulus in the diagonal direction
$\nu_{v\theta}$	0.091		Poisson horizontal module
$K_{w\theta}$	35487.12	kN/m	Fictitious stiffness of the infill (elastic range)
b_w	462.85	mm	Height of the equivalent strut according (rfr. Mainstone)

*Table 8.1: geometry and mechanical parameters of the infill panel
(1:1 scale ratio)*

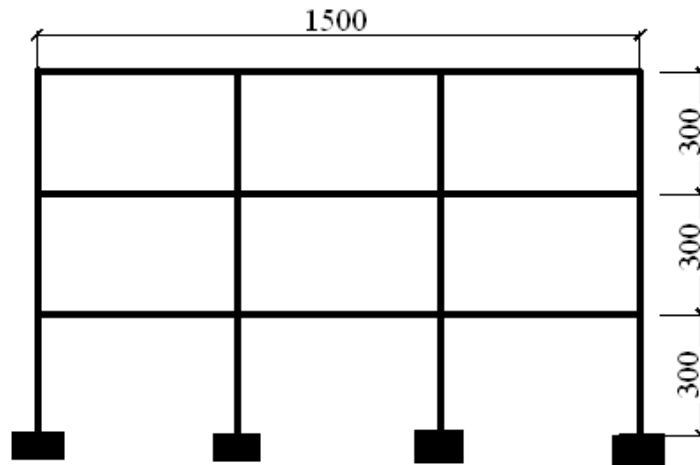


Figure 8.1: geometry of the r.c. frame, scale ratio 1:1 [cm]

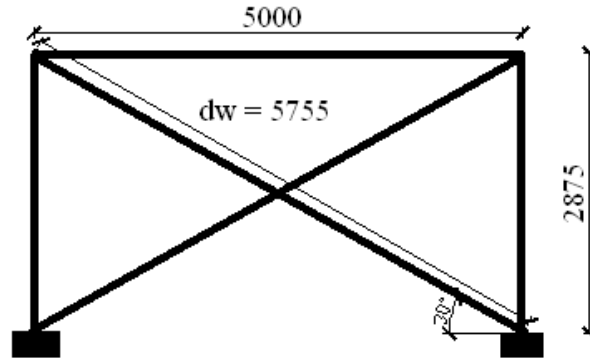


Figure 8.2: details of one single infilled portal of the frame, scale ratio 1:1 [mm]

<i>Stress-strain curve of the experimental strut model</i>		
ε [mm]	σ [kN]	
0.06%	3.34	Crack
0.11%	5.41	Max
0.13%	5.40	Failure

Table 8.2: stress-strain curve of the infill, experimentally determined

<i>Load-deformation curve of the experimental strut model</i>			
<i>Deformation [mm]</i>		<i>Axial load [kN]</i>	
-	0	-	0
$d_{e\theta}$	3,453	$F_{e\theta}$	181,31
$d_{w\theta}$	6,330	$F_{w\theta}$	300,67
$d_{wu\theta}$	7,481	$F_{u\theta}$	299,39
$d_{u\theta}$	-	$F_{residual}$	-

Table 8.3: parameters of the constitutive model of the strut determined for the frame (1:1 scale ratio)

The analyses have been carried out for the following types of plane frames (Figure 8.3, 8.4):

F_b bare frame;
 $F_{i,1}$ first floor partially infilled;

$F_{i,2}$ frame completely infilled;
 $F_{i,3}$ first floor bare.

In all four types, the global reaction has been determined from numerical models and discussed, all the analysis discussed are the first step of future studies. In the same way as performed for the portal, the *pushover* analyses have also been performed for the frames; therefore the results achieved in terms of the *capacity curve*, adopting the top of the building as displacement control element, will be presented and discussed.

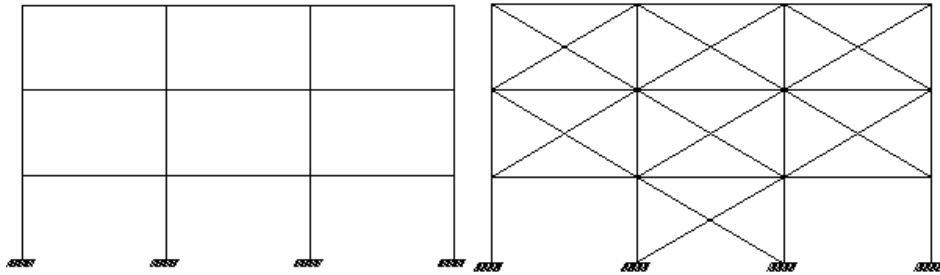


Figure 8.3: frame F_b (left) and $F_{i,1}$ (right)

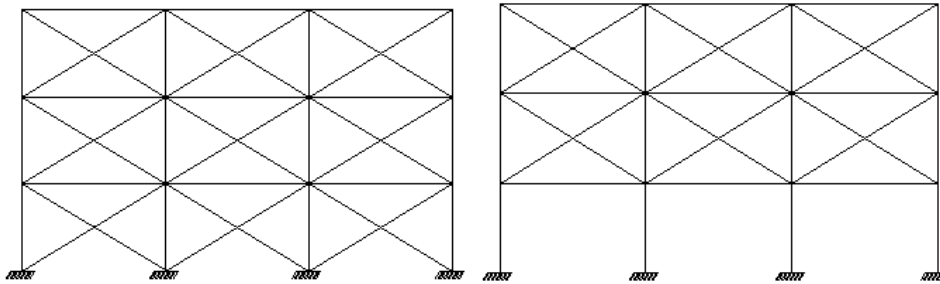


Figure 8.4: frame $F_{i,2}$ (left) and $F_{i,3}$ (right)

The *pushover* analyses described in this chapter refer to a distribution of horizontal load imposed, proportional to the first modal form.

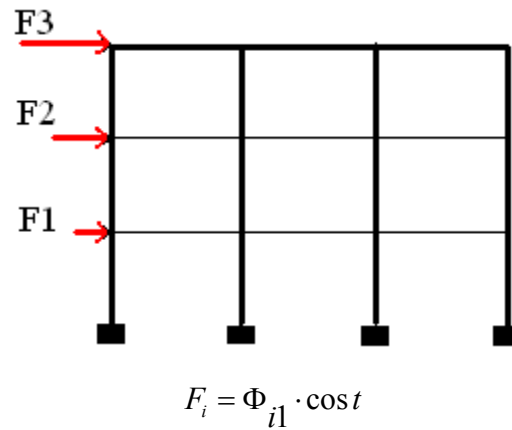


Figure 8.5: distribution of the horizontal loads adopted (proportional to the first modal form)

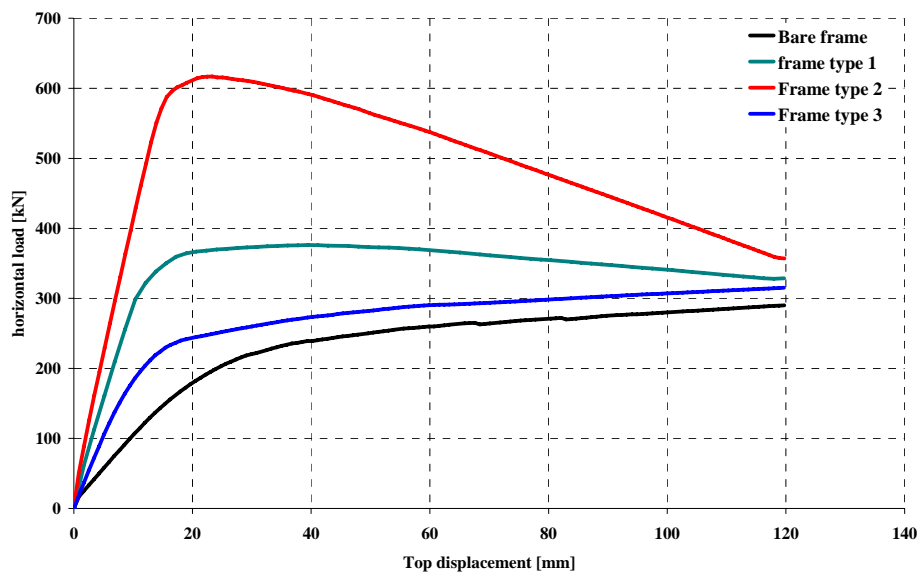


Figure 8.6: capacity curves of the frames analysed

Table 8.4 describes the results of the modal analyses performed on the frames, Table 8.5 presents the results achieved.

<i>Type</i>	<i>T [sec]</i>	Φ_{11}	Φ_{21}	Φ_{31}
<i>Bare frame</i>	0.593	0.355	0.761	1.0
<i>Type 1</i>	0.448	0.482	0.822	1.0
<i>Type 2</i>	0.404	0.393	0.782	1.0
<i>Type 3</i>	0.485	0.538	0.848	1.0

Table 8.4: modal analysis results, parameter of the horizontal load distribution

<i>Type</i>	<i>F_{max}</i> [kN]	<i>K_i</i> [kN/m]
<i>Bare frame</i>	290	11409
<i>Type 1</i>	376	31206
<i>Type 2</i>	617	44053
<i>Type 3</i>	315	20393

Table 8.5: summary of results of the pushover analyses

As known to determine the state of damage of the infills in the structures with more than one floor, it is possible to refer to an assessment of the *interstorey drift*; in this regard the results achieved are explained below.

It is important to point out that the frames $F_{i,2}$ and $F_{i,3}$ are subject to the developing of *soft storey* mechanisms due to a high difference in stiffness between the lower storey and the upper stories (soft storey is a mechanism in which the upper storeys of open first storey buildings move together as a single block: such buildings are like inverted pendulums Figure 8.7).

Furthermore, it is also important to point out that this mechanism of collapse can only be truly appreciated if design criteria that take into consideration the effective presence of infills are adopted because, as it can be observed from Figures 8.7-8.10, the *interstorey drift* found by analysing the bare frame differs drastically from the one found in the infilled frames.

This proves how an analysis that does not take into consideration the presence of the infills provides dissimilar results to the real behaviour of the structure.

As the analyses performed confirm, the presence of walls in upper storeys makes them much stiffer than the open first storey.

Thus, the upper storeys move almost together as a single block, and most of the horizontal displacement of the building occurs in the soft first storey itself.

Thus, such buildings swing *back-and-forth* like inverted pendulums during earthquake shaking, and the columns in the open first storey are severely stressed.

If the columns are weak (do not have the required strength to resist these high stresses) or if they do not have adequate ductility, they may be severely damaged which may even lead to collapse of the building.

An open first storey building, having only columns in the first storey (or the first storey mostly bare) and both infills and columns in the upper storeys, have two distinct characteristics.

It is relatively flexible in the first storey (the relative horizontal displacement in the first storey is much larger than each one of the storeys above).

Furthermore it is relatively weak in first storey (the total horizontal earthquake force that can be supported in the first storey is significantly smaller than what each of the storeys above can support).

Thus, the open first storey may also be a weak storey. Often, open first storey buildings are called soft storey buildings, even though their first storey may be soft and weak.

Generally, the soft or weak storey usually exists at the first storey level as in the case of F_{i1} and F_{i3} , but it could be at any other storey level too.

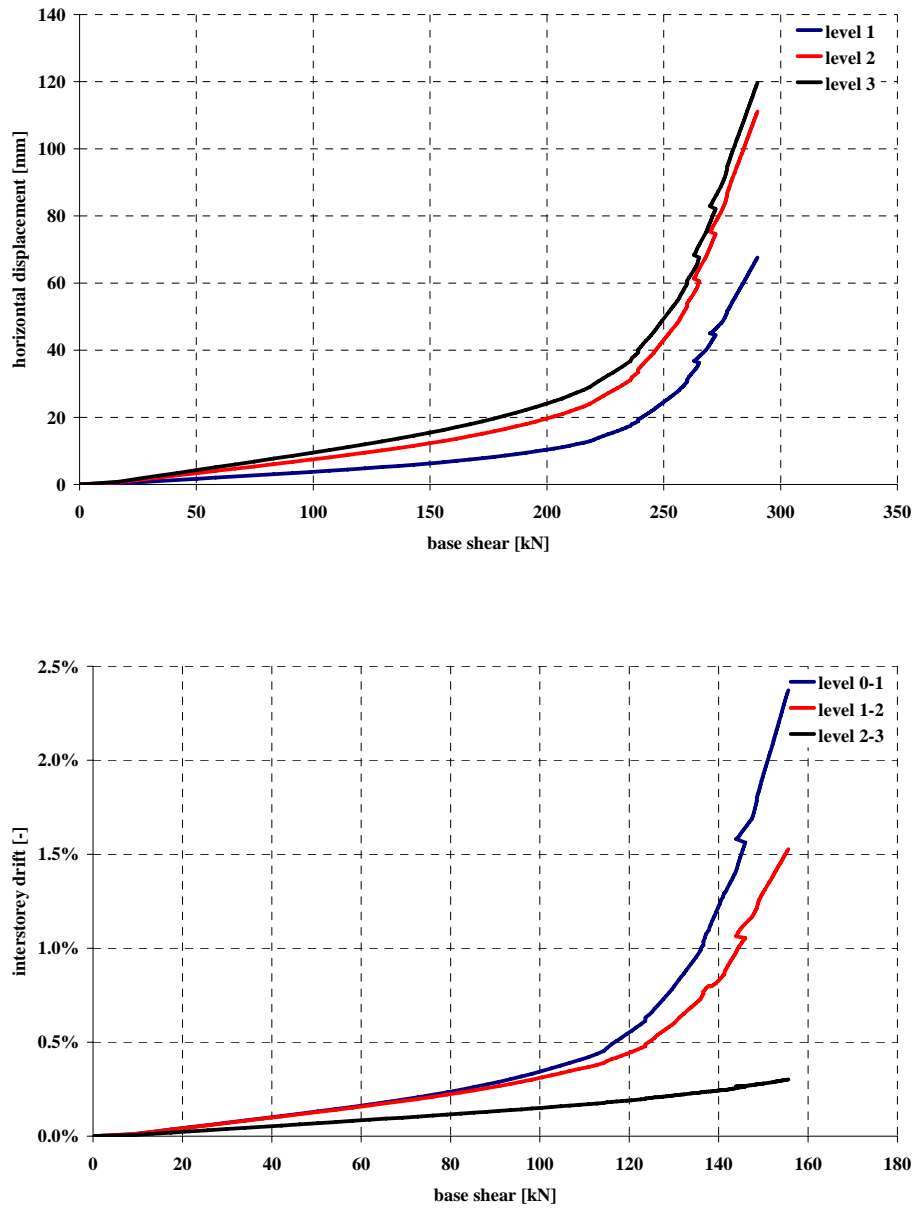


Figure 8.7: horizontal displacements of each level (up) interstorey drift of the bare frame (down)

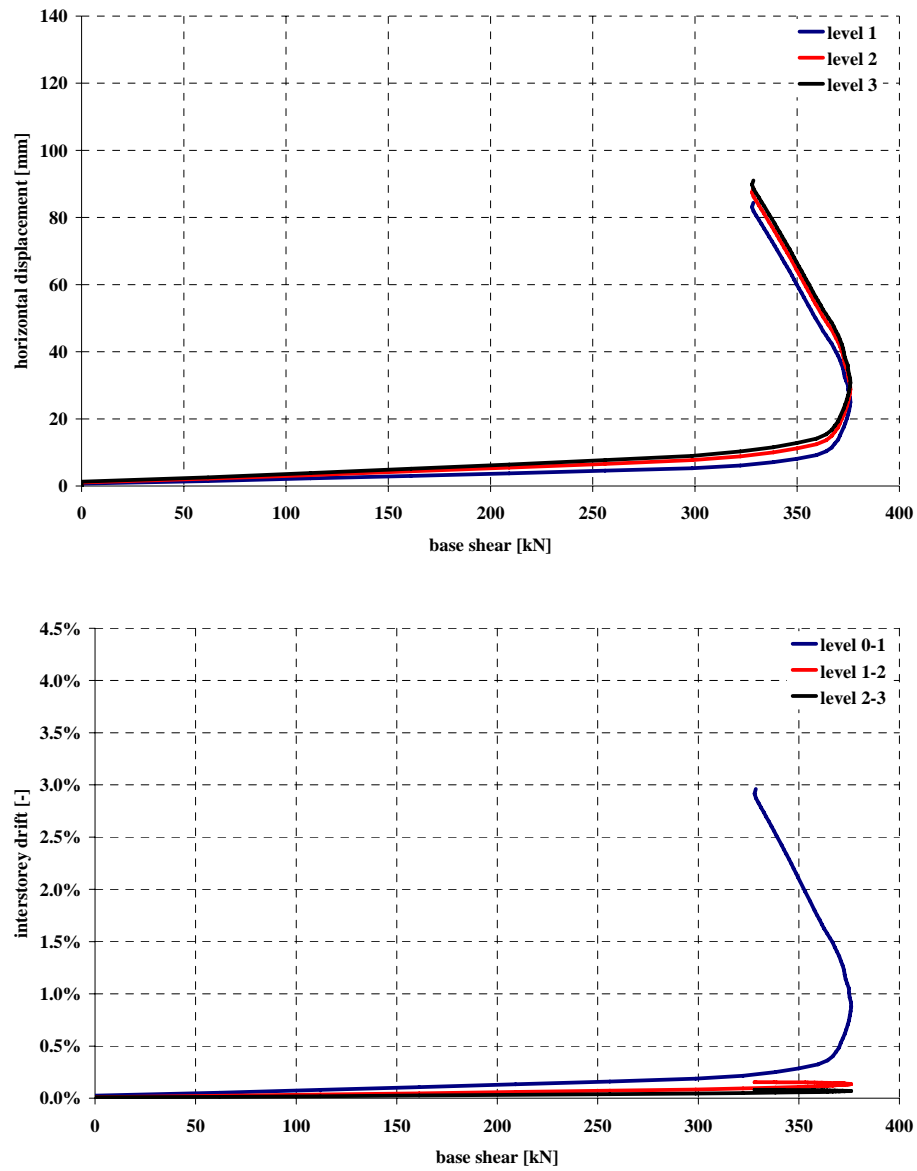


Figure 8.8: horizontal displacements of each level (up) interstorey drift of the frame type 1(down)

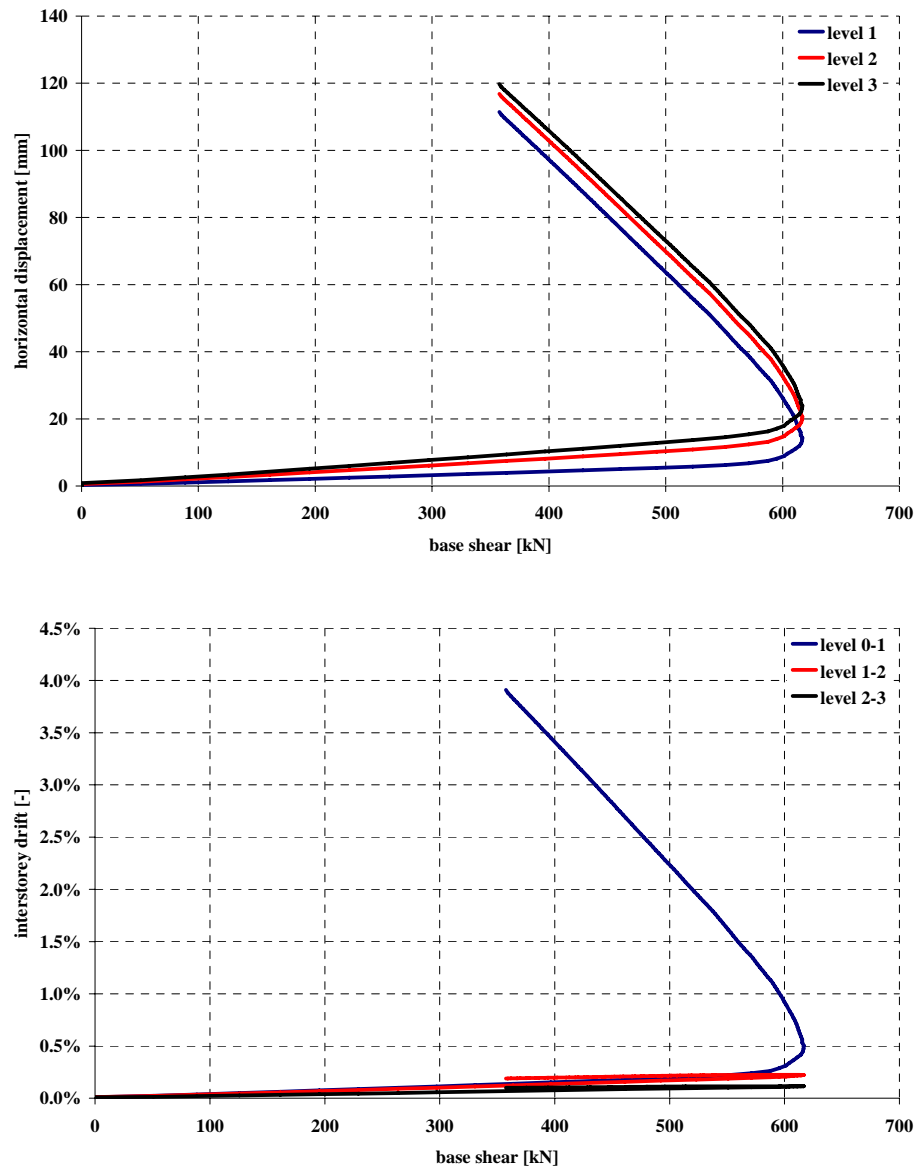


Figure 8.9: horizontal displacements of each level (up) interstorey drift of the frame type 2 (down)

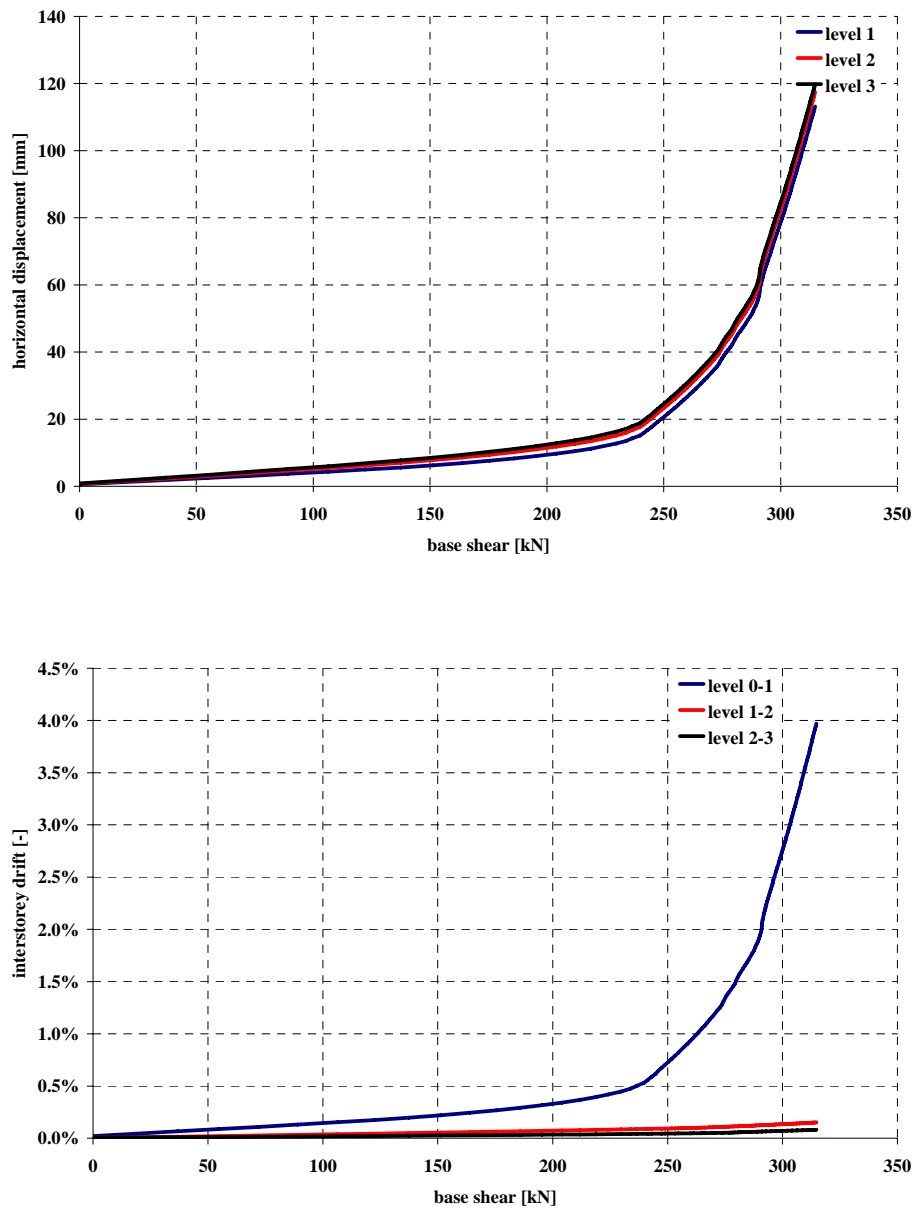


Figure 8.10: horizontal displacements of each level (up) interstorey drift of the frame type 3 (down)

As in the case of the portal, after having assessed the global behaviour of the structures, the stress state of the r.c sections was investigated; of the four types described, the results achieved on the frame F_b and $F_{i,l}$ have been discussed.

By analyzing the stress state of the section of the frames F_b and $F_{i,l}$ the distribution of plastic hinges has been determined, in the following figures each plastic hinge has been indicated on the *capacity curve*.

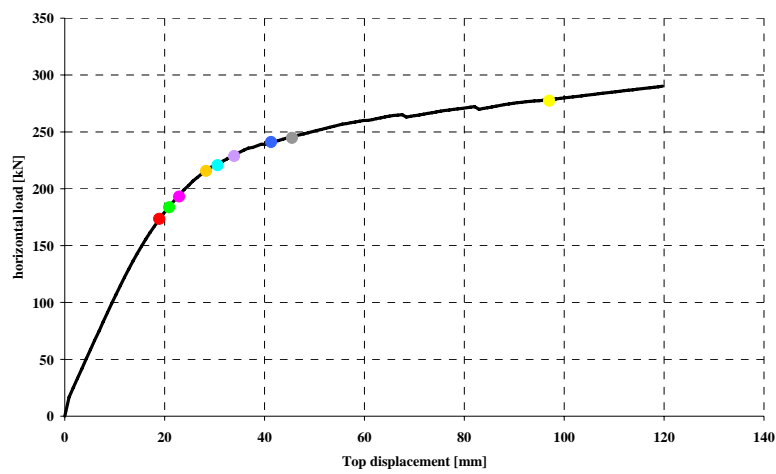


Figure 8.11: capacity curve and plastic hinges of the bare frame

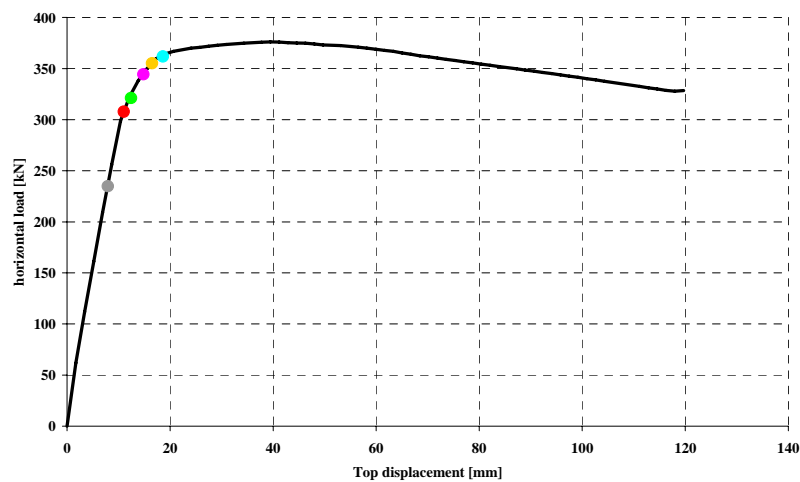


Figure 8.12: capacity curve and plastic hinges of the frame type 2

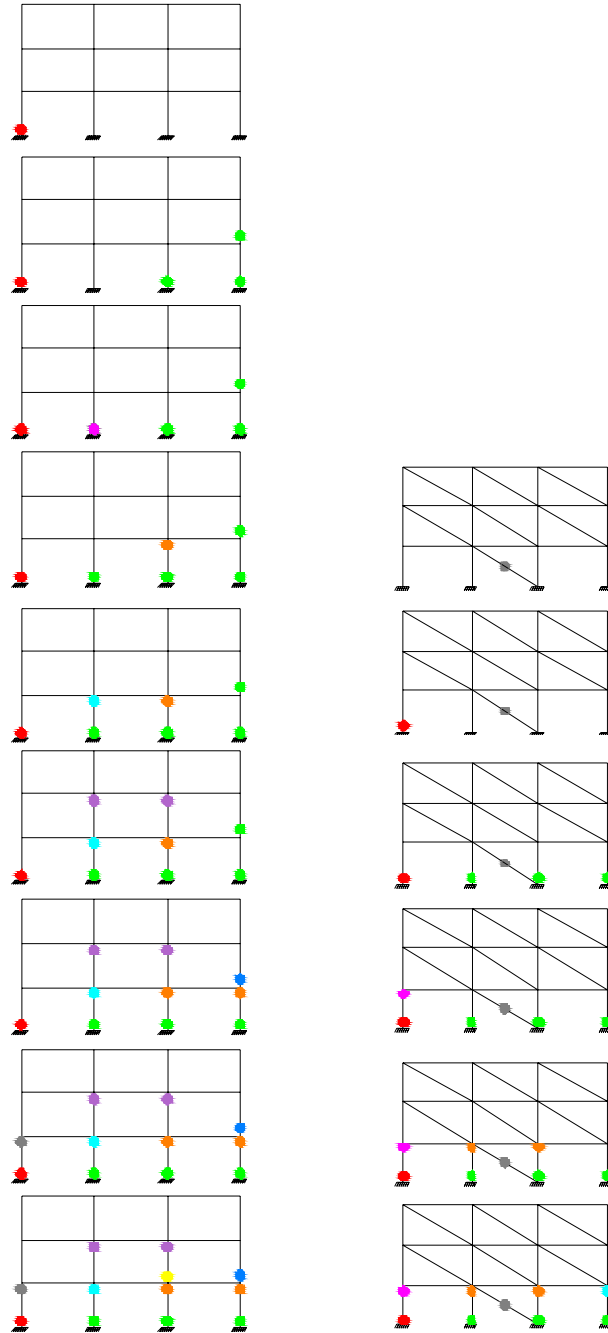


Figure 8.13: plastic hinges on the bare (left) and type 1(right) frame

From figures 8.11-8.13 it is possible to appreciate how distribution in elevation of the infill causes a different stiffness distribution between the various stories, this results in a concentration of ductility requested on the less stiff floor with the subsequent creation of a *first soft storey*.

By analysing the state of the sections of the elements present in the upper levels, has been observed that the yielding stress has never been achieved, not even the infill reaches the failure stress.

We can see that this mechanism of collapse, relevant for this kind of structure, has been appreciated by extending the analysis to a real structure of several levels; in this way the models described as an extension of the portal models can develop the studies performed to a wider range of real structures.

The geometry of the *triple strut* model has also been determined for the frames with the objective of comparing it with the *single strut* model even in the case of a much more complex frame.

The characteristics of the model are described below together with comparison between the results previously achieved and the *pushover* analysis.

From Figure 8.17 can be observed that the *triple strut* model, also in the case of plane multi-storey frame, concordantly with what has been observed for the portal, leads to identical results if the two *capacity curves* are compared.

From this comparison results that the *triple strut* model adopted is concordant with the simpler *single strut* model.

However the *triple strut* model is simple to be adopted also for professional aims, moreover it is more complete: as already said in the previous chapters it can determine a more realistic distribution of shear load on columns helping the designer to check shear resistance to avoid a brittle collapse.

<i>Triple strut model</i>		
β	0.03	<i>rad</i>
ζ	183.70	<i>mm</i>
b_{wo}	231.42	<i>mm</i>
b_{wl}	123.68	<i>mm</i>

Table 8.6: geometry of the triple strut model

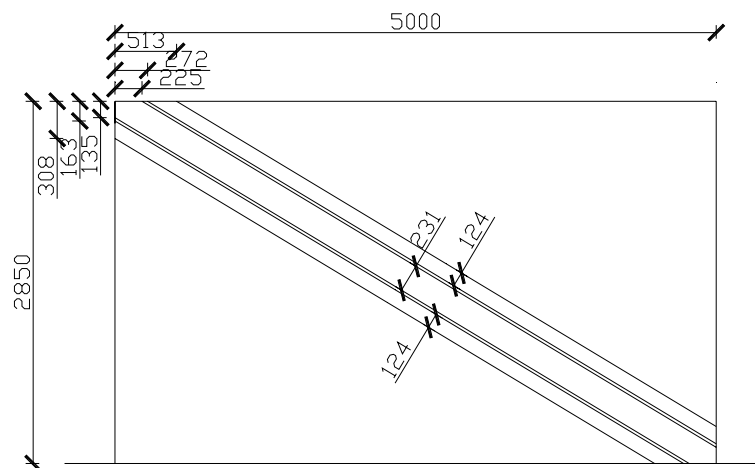


Figure 8.15: triple strut model (frame scale ratio 1:1)

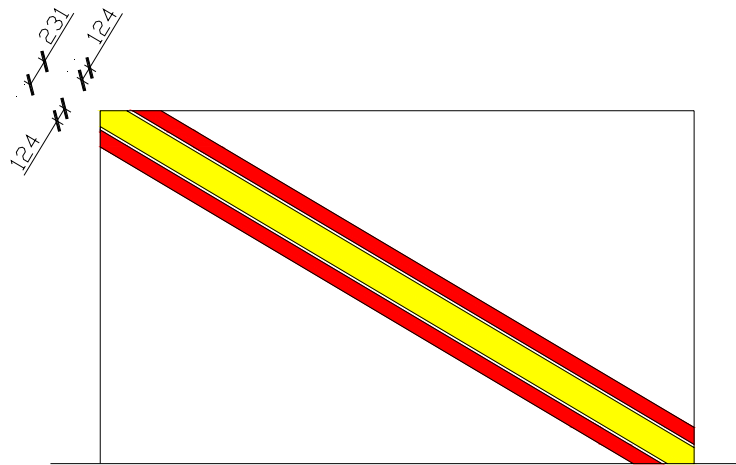


Figure 8.16: geometry of the triple strut model (frame scale ratio 1:1)

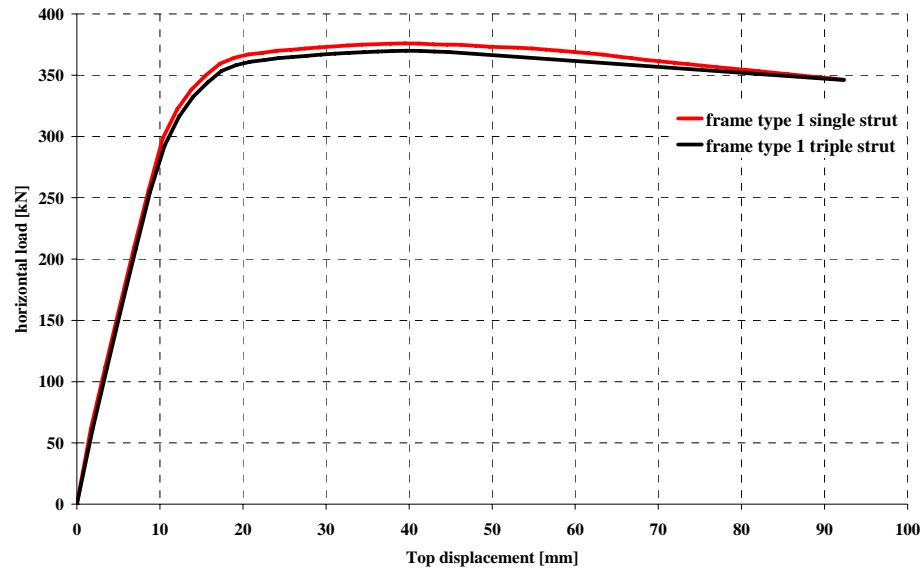


Figure 8.17: comparison between the capacity curves determined with the triple strut and the single strut models for the frame type 1

9. Conclusions

The main aim of the study described in this thesis is to investigate the mechanism of interaction between reinforced concrete frames and infills commonly used in Italy through numerical models and experimental research. As proved in many scientific studies, the structure cannot be considered as consisting of a reinforced concrete frame only as the infill affects its resistance, stiffness and ductility. The problem faced is extremely complex if we consider the numerous existing variables. In particular, the infill consists of materials with uncertain mechanical properties and its behaviour is also influenced by the quality of labour.

In order to conceive a procedure to achieve reliable results, an in-depth experimental activity was carried out on different types of materials (bricks and mortars) and walls, ending up with the calibration of numerical models based on experimental tests on 1:2 scaled frames. Thus, the mechanical characteristics of the constitutive materials of the infill have been determined and compared with the strength of infill walls made of the same components. Cyclic tests on bare and infilled r.c. portals highlighted the effects of infill panels on the structural behaviour; these effects were compared with the response of infill panels from compression tests in horizontal, vertical and diagonal directions.

Each step of the experimental research described above have highlighted the complexity of correlating the characteristics of tested specimens, regardless of whether they are constitutive elements or infill panels, to those of a real structure. In this regard, this study aims to provide a concrete contribution towards the identification of the most relevant materials properties and consequently to provide some useful references in order to repeat the same process even in the absence of such a broad experimental campaign.

From the qualification results of the walls and their comparison with the theoretical forecasts, the need to identify the mechanical characteristics of the infills can be found specific experiments. Corformula formula, found in Codes, line guides and specific scientific literature, to evaluate infill panel strength from its components strengths turned out to be not very reliable when compared with the experimental data. This problem is made even more complicated by the large dispersion of the mechanical properties: this is mainly due to a non controlled production of bricks

traditionally used for non structural elements. Furthermore external factors exist, such as workers skill, which add uncertainties that are difficult to be controlled.

Minor difficulties have been encountered in calibrating the *axial load-deformation* relationship to model the infill behaviour. In reality experimental calibration of the infill model, initially hypothesised on the basis of the indications discussed in literature, has substantially modified the maximum compression strength of masonry; if it was possible to learn of this in advance, decisively satisfactory numerical results would have been achieved; the other parameters recalibrated have provided a greater level of refinement to modelling without substantially changing the results. From the aforementioned it follows that a reliable evaluation of infill panels strength (diagonally loaded) is the main problem to be solved since it affects the subsequent steps of modelling. Therefore, the execution of an in-depth study for a much more correct assessment of the compression strength of the brickwork in any loading direction, also including the confinement effect of the surrounding frame, is needed.

Tests carried out on the portal frames showed that the contribution provided by the infill to the horizontal strength of the structure is very important and should not be neglected: the portal strength has been increased by the infill by a factor of 1.8, while the initial stiffness has been increased by a factor of 9.4.

Tests performed on the portal have also highlighted how the collapse mechanism of the structure has been substantially modified. The bare portal suffered diffused plastic hinges, initially at the base of the columns and subsequently at the top of them, while a lower damage level in r.c. elements was detected in the infilled frame up to achievement of the infill peak strength: after infill was heavily damaged, the portal supported most of the horizontal load and quickly cracked until collapse. Furthermore, it is also important to point out that concrete cover expulsion and buckling of compressed bars, which typically occur in frames subjected to horizontal load, have gradually emerged in the cyclic test on the bare portal and in a much faster and less diffused manner in the infilled portal where the deterioration of the brickwork seemed to be the prevalent phenomenon. The presence of infills introduces another risk factor into the structure that is the fall of many parts of the heavily cracked infill which, once its maximum capacity has reached.

At the current state, the experimental tests on infilled frame have been performed using only one kind of the analysed walls; collected

experimental data form a valid and useful database for subsequent studies which can be performed to extend the range of validity of the achieved results.

Experimental activities were supported by numerical analyses of the studied structures which aimed to create reliable numerical models to match the experimental results and to critically review some simple infill mathematical models.

Mathematical models, selected among the most suitable for professional applications, yielded satisfactory results compared with experimental ones, mostly in terms of *capacity curves*, i.e. monotonic responses from *pushover* analyses. Therefore, such models should be much more widely used in earthquake engineering to gain accurate and reliable evaluations of the seismic response of this kind of infilled r.c. frames which are very common in Italy. Codes recommendations should be revised in order to make engineers aware of the importance of including also actually considered non structural infill in design and assessment procedures: in fact such elements effects are too often underestimated or even neglected. It is also needed to provide engineer with feasible infill models and much more detailed and specific indications on mechanical properties of constitutive materials, i.e. brick and mortar.

9.1 Future developments

Future developments include extensions of the case studies including tests on the portal infilled with both bricks (half-full and hollow) and both masonry (type 1 and 2). So it will be possible to observe whether or not the observations drawn for infills of half-full bricks could be generalized and therefore if they could be extended to the case of very slender infill panels. At the same time, as the numerical models discussed here have been approved, it will also be possible to extend the study, briefly mentioned herein, to numerical models of real 1:1 structures with different infill layout. Also notice that further experimental investigations should be aimed to study sliding strength along bed-joints; these results will allow to define further numerical models to capture shear collapse too. Therefore we believe that all of the themes discussed in this thesis can form reason for investigation for the individuals that have elaborated it but also an experimental reference for those who intend to develop further personal studies on this topic.

Bibliography

ACI Committee 318. *Building code requirements for reinforced concrete (ACI318-02)*. Detroit: American Concrete Institute., 2002.

Albanesi T., Bergami A. V., Nuti C., Biondi S., Candigliota E.. *Caratterizzazione teorico-sperimentale di tamponature in laterizio per telai in cemento armato*, Atti del Convegno Nazionale ANIDIS 2007, XII, Pisa, Italy

Albanesi, T., Bergami, A.V., Nuti, C., 2006. *Comportamento sperimentale di tamponature leggere*. Atti del Convegno Nazionale “Sperimentazione su materiali e strutture”, pp. 821-830, 6-7 Dicembre 2006, Venezia, Italy.

Ameny, P., Loov, R.E.and Shrive, N.G. [1983] *Prediction of Elastic Behaviour of Masonry*, International journal of Masonry Construction, Vol. 3, No. 1, pp. 1-9

Applied Technology Council a nonprofit corporation advancing engineering applications for hazard mitigation California - Washington, DC Area–ATC-40 *Seismic Evaluation and Retrofit of Concrete Buildings*.

Asteris, P.G. [1996] *A Method for the Modeling of Infilled Frames (Method of Contact Points)*, Proceedings of the 11th World Conference on Earthquake Engineering, Acapulco, Mexico.

Asteris, P.G. [2003] *Lateral Stiffness of Brick Masonry Infilled Plane Frames*, ASCE Journal of Structural Engineering, Vol 129, No. 8, pp. 1071-1079

Bertoldi S. H., Decanini, L. D., Santini S. and Via G. [1994] *Analytical models in infilled frames*, Proceedings of the 10th European Conference on Earthquake Engineering, Vienna, Austria.

Bertoldi S. H., Decanini, L.D. and Gavarini, C. [1999] *Telai tamponati soggetti ad azioni sismiche, un modello semplificato: confronto sperimentale e numerico*, Atti del 60 Convegno Nazionale ANIDIS, 2, Perugia, Italy.

Bertoldi, S. H., Decanini, L. D., & Gavarini, C., *Telai tamponati soggetti ad azioni sismiche, un modello semplificato: confronto sperimentale e numerico*, Atti del VI Convegno Nazionale ANIDIS, vol. 2, pp. 815-824, Perugia, 13-15 Ottobre 1993.

Biondi S, Candigliota E, Nuti C. *Modello a tre bielle per l'analisi degli effetti locali della tamponatura nelle strutture in cemento armato*, Atti del Convegno Nazionale ANIDIS, XI, January 2004, Genova.

Biondi S., Candigliota E. e Nuti C., Local Effects Modelling of an Infilled Frame: a Three-Strut Model Refinement.

Biondi, S., Colangelo, F. and Nuti, C. [2000]. *La risposta sismica di telai con tamponature murarie*, Gruppo Nazionale per la Difesa dai Terremoti, Rome, Italy.

Biondi, S., Candigliota, E., Nuti, C. 2001. *Carico limite per strutture intelaiate tamponate: verifica delle prescrizioni di normativa*. Atti del Convegno Nazionale ANIDIS X, Potenza, 9-13 Settembre 2001, F1, Id. F101.

Biondi, S., Candigliota, E., Nuti, C. 2002. *Tests on different infilled specimens: a critical review of code ultimate state criteria*. Proceedings of 12th European Conference on Earthquake Engineering, London, 9- 13 September 2002, paper 748.

Biondi, S., Colangelo, F., Nuti, C. (a cura di), 2002. *La risposta sismica dei telai con tamponature murarie*. Roma: CNR-Gruppo Nazionale per la Difesa dai Terremoti.

CIRCOLARE 10 aprile 1997, n. 65 istruzioni per l'applicazione delle *Norme tecniche per le costruzioni in zone sismiche* - allegato 2 *INTERAZIONE FRA TELAI E PANNELLI MURARI DI TAMPONATURA*

Cuomo M., Badalà A.: *Problematiche metodologiche relative alla determinazione sperimentale delle proprietà meccaniche dei materiali murari e dei loro componenti, La protezione del patrimonio culturale – La questione sismica*, II seminario Nazionale di Studio, Roma, 9-10 Aprile 1997, pp. 657-683. Gangemi Editore.

D. Combescure. *Modélisation du comportement sismique des structures de bâtiment comportant des murs de remplissage en maçonnerie*. Thèse de doctorat Ecole Centrale de Paris, 1996.

D. Combescure. *Seismic Behaviour of Infilled RC Frame using Non Linear Modelling Identification of the Equivalent Strut and Interactions with the RC Frame*, RAPPORT DM2S, 2001

D.M. LL.PP. 14.09.2005. *Norme Tecniche per le Costruzioni*. Supplemento Ord. n. 159 alla G.U. 23.09.2005 n. 222.

D.M. LL.PP. 20.11.1987: *Norme tecniche per la progettazione, esecuzione e collaudo degli edifici in muratura e per il loro consolidamento*, Supplemento Ordinario alla G.U. n. 285 del 5.12.1987.

D.M. LL.PP. 9.01.1996: *Norme tecniche per il calcolo, l'esecuzione ed il collaudo delle strutture in cemento armato, normale e precompresso e per le strutture metalliche*, Supplemento Ordinario alla G.U. n. 29 del 5.02.1996.

D.M.LL.PP. del 09/01/1996 *Norme tecniche per il calcolo per il collaudo delle strutture in cemento armato, normale e precompresso e per le strutture metalliche – punto 2.1.2.*

Dawe, J. L., & Seah, C. K. *Analysis of concrete masonry infilled steel frames subjected to in-plane loads*, Proc. of the 5th Canadian Masonry Symposium, pp. 329-340, Vancouver, 1989.

Decanini, L. D., et al.. *Modelo simplificado de paneles de mamposteria con aberturas incluidos en marcos de concreto reforzado y metalicos. Comparacion y calibracion con resultados experimentales y numericos*, Proc. of the 9th International Seminar on Earthquake Prognostics, San José, Costa Rica, September 19-23, 1994.

DISAT pubblicazione febbraio 1999-F. Colangelo – *Qualificazione, risposta sismica Pseudodinamica e modelli fenomenologici di portali di C.A. tamponati con laterizio*

Durrani, A. J., & Luo, Y. H.. *Seismic retrofit of flat-slab buildings with masonry infills*, Proc. from the NCEER Workshop on. Seismic Response of Masonry infills - Report NCEER-94-0004, pp. 1/3-8, March 1, 1994.

Ecoleader Project 4. *A proposal for tests on infilled frames of existing buildings: frames designed without seismic provisions or with less recent ones - static tests on infill masonry specimens* - Final Report, University of Roma Tre, Department of Structures, Experimental Laboratory on Materials and Structures, December 2005.

FEMA (Federal Emergency Management Agency) 356. *Prestandard And Commentary For The Seismic Rehabilitation Of Buildings*, Novembre 2000, pp 7-25.

G.G. Pnelis, A.J. Kappos. *Earthquake Resistant concrete structures*, E&F Spon, London, 1997.

Gerin M., Adebar P.. *Accounting for shear in seismic analysis of concrete structures*. 13th World Conference on Earthquake Engineering Vancouver, B.C., Canada August 1-6, 2004. Paper No. 1747.

Kent and Park, 1971. D.C. Kent and R. Park. *Flexural members with confined concrete*. Journal of the Structural Division ASCE 97 (1971), pp. 1969–1990.

Klingner, R. E., & Bertero, V. V.. *Infilled frames in earthquake-resistant construction*, Report EERC 76-32, Earthquake Engineering Research Center, December 1976.

Klingner, R.E. and Bertero, V.V. [1976]. *Infilled frames in earthquake resistant construction*, Earthquake Engineering Research Center, University of California, Berkeley, EERC 76-32.

Klingner, R.E. and Bertero, V.V. [1978]. *Earthquake resistance of infilled frames* ASCE Journal of the Structural Division, Vol. 104, No. ST6, pp. 973-989.

M Menegotto, PE Pinto – *IABSE Preliminary Report for Symposium on Resistance and and Ultimate Deformability of steel*, 1973

Papia, M., Cavalieri, L.. *Effetto irrigidente dei tamponamenti nei telai in c.a.*, II Conferenza plenaria Cofin. MURST "La sicurezza delle strutture in c.a. sotto azioni sismiche.....", Firenze, Dicembre, pp.85-94, 2000.

Mainstone, R. J.. *Supplementary note on the stiffness and strenght of infilled frames*, Current Paper CP 13/74, Building Research Establishment, London, 1974.

Mainstone, R. J.. *Supplementary note on the stiffness and strenght of infilled frames*, Current Paper CP 13/74, Building Research Establishment, London, 1974.

Mainstone, R.J. [1971]. *On the stiffness and strength of infilled panels*, Proceedings of the Institution of Civil Engineers, Supplement IV, pp. 57-90.

Mallik, D.V., Severn, R.T.. *The behavior of infilled frames under static loading*, Proceedings Institution of Civil Engineers, London, vol. 38, pp. 639-656, 1967.

Mehrabi, A. B. et al., *Performance of masonry infilled rc frames under inplanes latral load*, report CU/SR-94/6, University of Colorado at Boulder, October 1994

Mehrabi, A.B., et al.. *Performance of masonry - infilled R/C frames under in-plane lateral loads*, Rep. CU/SR-94-6, Department of Civil Environmental and Architecture Engineering, University of Colorado, 1994.

Mehrabi, A.B., Shing, P.B.. *Finite element modeling of masonry-infilled RC frames*, Journal of Structural Engineering, ASCE, vol. 123, n. 5, pp. 604-613, 1997.

Mehrabi, A.B., Shing, P.B., Schuler, M.P., Noland, J.L.. *Experimental evaluation of masonryinfilled RC frames*, Journal of Structural Engineering, ASCE, vol. 122, n. 3, pp. 228-237, 1996.

Mehrabi, A.B., Shing, P.B., Schuller, M.P. and Noland, J.L. [1996]. *Experimental evaluation of masonry-infilled RC frames* ASCE Journal of Structural Engineering, Vol. 122, No. 3, pp.228-237.

Ministero dei Lavori Pubblici, Circolare IO Aprile 1997, *Istruzioni per l'applicazione delle norme tecniche per le costruzioni in zone sismiche di cui al decreto ministeriale 16 gennaio 1996*, Supplemento Ordinario alla Gazzetta Ufficiale n. 97, 28 Aprile 1997.

Mosalam, K.M., White, R.N., Gergely, P.. *Static response of infilled frames using quasi-static experimentation*, Journal of Structural Engineering, ASCE, vol. 123, n. 11, pp. 1462-1469, 1997.

Negro, P., Verzeletti, G.. *Effect of infills on the global behaviour of rc frames: energy considerations from pseudo-dynamic tests*, Earthquake Engineering and Structural Dynamics, n. 25, pp. 753-773, 1996.

Ordinanza 3274, come modificata dall'OPCM 3431 del 3/05/2005 allegato 2 "norme tecniche per il progetto, la valutazione e l'adeguamento sismico degli edifici".

Panagiotakos, T.B. and Fardis, M.N. [1994]. *Proposed nonlinear strut models for infill panels*, 1st Year Progress Report of HCM-PREC8 Project, University of Paris.

Parducci, A., Mezzi, M.. *Repeated horizontal displacements of infilled frames having different stiffness and connecting systems*, Proceedings 7th World Conference on Earthquake Engineering, Istanbul, vol. 7, pp. 193-196, 1980

Paulay, T. and Priestley, M.J.N. [1992]. *Seismic design of reinforced concrete and masonry buildings*, John Wiley & Sons, New York, United States.

Prepared by AMERICAN SOCIETY OF CIVIL ENGINEERS Reston, Virginia for
FEDERAL EMERGENCY MANAGEMENT AGENCY Washington, D.C.
PRESTANDARD AND COMMENTARY FOR THESEISMIC REHABILITATION OF
BUILDINGS

Santini, S.. *L'influenza delle tamponature sul comportamento sismico delle strutture intelaiate*, Tesi di dottorato, Dipartimento di Ingegneria Strutturale e Geotecnica, Università di Roma "La Sapienza", Febbraio 1995.

Shing, P.B. et al [1992]. *Finite elements analysis of shear resistance masonry wall panels with and without confining frames*, Proceedings of the 10th World Conference on Earthquake Engineering, Madrid, Spain.

Silvia Mazzoni, Frank McKenna, Michael H. Scott, Gregory L. Fenves, et al..
OpenSees Command Language Manual

Stafford-Smith, B.. *Behavior of square infilled frames*, Journal of the Structural Division, vol. 92, n. ST1, pp 381-403,1996

Tassios T.P.: *Meccanica delle murature*, Liguori Editore, Napoli, 1988.

UNI EN 1015-11: *Determineazione della resistenza a flessione e a compressione della malta indurita*.

UNI EN 771-1: *Specifiche per elementi per muratura*.

UNI EN 772-1-11: *Metodi di prova per elementi in muratura. Determineazione della resistenza a compressione della muratura*.

Zarri F.: *Parametri di resistenza e di deformabilità meccanica di murature di laterizio*, Costruire in Laterizio, anno 7, n. 41, pp. 452-455 (1994).